

# SRI International

Final Technical Report • September 1997

## CONTROL TECHNOLOGY FOR SMART MATERIALS

*Prepared by:*

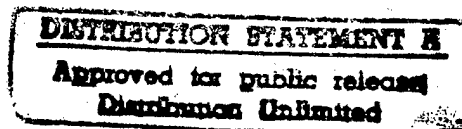
DAVID S. FLAMM  
KENNETH C. CHOU  
GARY S. GUTHART  
*SRI International*

LARRY P. HECK  
RONALD M. UEBERSCHAER  
WILLIAM C. NOWLIN

GARY H. KOOPMANN  
STEVE SHARP  
HANS WODTKE  
*The Pennsylvania State University*

*Prepared for:*

Office of Naval Research, Code 334  
Ballston Tower One  
800 N. Quincy Street  
Arlington, VA 22217-5660  
Attn: Kam Ng, Program Officer



Contract N00014-94-C-0176  
ARPA Order No. B848  
CDRL A003  
Contract Duration: 30 September 1994 - 31 July 1997  
Contract Amount: \$883,989

19971030 032

SRI Project 6602

The views and conclusions contained in this document are those of the authors and should not be interpreted as necessarily representing the official policies, either expressed or implied, of the Advanced Research Projects Agency or the U.S. Government.

Co-Principal Investigators: David S. Flamm, Principal Scientist  
Telephone: 650-859-2460  
Fax: 650-859-4941

Kenneth C. Chou, Senior Research Engineer  
Telephone: 650-859-3097  
Fax: 650-859-4121

*Approved by:*

DAVID S. FLAMM, *Principal Scientist*  
*Applied Control and Signal Processing Program*

ERIC M. PEARSON, *Director*  
*Applied Physical Sciences Laboratory*

DTIC QUALITY INSPECTED 3

## **REPRODUCTION QUALITY NOTICE**

**This document is the best quality available. The copy furnished to DTIC contained pages that may have the following quality problems:**

- **Pages smaller or larger than normal.**
- **Pages with background color or light colored printing.**
- **Pages with small type or poor printing; and or**
- **Pages with continuous tone material or color photographs.**

**Due to various output media available these conditions may or may not cause poor legibility in the microfiche or hardcopy output you receive.**



**If this block is checked, the copy furnished to DTIC contained pages with color printing, that when reproduced in Black and White, may change detail of the original copy.**

# Contents

<b>1</b>	<b>EXECUTIVE SUMMARY</b>	<b>4</b>
1.1	Objectives . . . . .	4
1.2	Results . . . . .	4
1.3	Recommendations . . . . .	6
<b>2</b>	<b>INTRODUCTION</b>	<b>7</b>
<b>3</b>	<b>CONTROL PROBLEM FORMULATION</b>	<b>11</b>
<b>4</b>	<b>WAVELET CONTROL DESIGN METHOD</b>	<b>14</b>
4.1	Overview . . . . .	14
4.2	Change of Basis for Control Problem . . . . .	14
4.3	Multiscale Bases . . . . .	16
4.3.1	Orthonormal Wavelets of Compact Support . . . . .	16
4.3.2	Compression Properties of Wavelets . . . . .	19
4.4	Designing Neutralization Path $P$ . . . . .	20
4.5	Designing Feedforward Path $Q$ . . . . .	22
4.5.1	Optimizing $Q$ in Multiscale Bases . . . . .	24
4.5.2	Banded (Locally Interconnectd) $Q$ . . . . .	24
4.5.3	Continuous Solutions . . . . .	25
4.5.4	Discrete Solutions . . . . .	26
4.5.5	Structure of Banded Matrices in Wavelet Domain . . . . .	28
4.6	Summary of Multiscale/multirate Methodology . . . . .	28
4.6.1	Wavelet-Based Neutralization Path . . . . .	29

(DTIC QUALITY INSPECTED &

4.6.2	Q-Parameter Design Feedforward Path . . . . .	29
<b>5</b>	<b>SENSOR/ACTUATOR PLACEMENT METHODS AND INTEGRATION WITH KIKO</b>	<b>31</b>
5.1	Overview . . . . .	31
5.2	Transducer Selection . . . . .	32
5.3	Direct Use of Imperfect Data . . . . .	34
5.4	Transformation of Nonuniform Data for Wavelet Calculations . . . . .	35
5.4.1	Problem Statement . . . . .	36
5.4.2	Outline of Approach . . . . .	37
5.4.3	Notation . . . . .	38
5.4.4	The Warping Function . . . . .	39
5.4.5	Building a Useful Imaginary Green's Function . . . . .	39
5.4.6	Bounds Comparison . . . . .	41
5.4.7	Issues . . . . .	41
5.5	Generalized Wavelets . . . . .	42
5.5.1	Comparisons of Reconstruction Error and Sparsity . . . . .	43
5.6	Conclusions and Recommendations for Further Work . . . . .	44
<b>6</b>	<b>NUMERICAL RESULTS AND SIMULATIONS FROM MODEL DATA</b>	<b>46</b>
6.1	Euler-Bernoulli Beam Results . . . . .	46
6.2	Flexible Plate Results . . . . .	51
6.3	Conclusions . . . . .	58
<b>7</b>	<b>RESULTS OF EXPERIMENTAL VALIDATION</b>	<b>61</b>
7.1	PSU Experimental Setup . . . . .	61

7.1.1	Experiment 1 - Frequency Domain Analysis . . . . .	61
7.1.2	Experiment 2 - Frequency Domain to Time Domain Analysis . . . . .	62
7.1.3	Experiment 3 - Frequency Domain to Time Domain Analysis . . . . .	62
7.1.4	Conclusion . . . . .	63
7.2	Validation of Green's Function Properties Using PSU DATA . . . . .	63
7.3	Wavelet Compression Using PSU Data . . . . .	67
<b>8</b>	<b>TECHNOLOGY TRANSFER</b>	<b>70</b>
<b>9</b>	<b>CONCLUSIONS</b>	<b>71</b>
<b>10</b>	<b>REFERENCES</b>	<b>72</b>
<b>A</b>	<b>Euler-Bernoulli Green's Function</b>	<b>74</b>
<b>B</b>	<b>Reference [11] (Transducer Placement for Broadband Active Vibration Control Using a Novel Multidimensional QR Factorization)</b>	<b>77</b>
<b>C</b>	<b>Reference [3] (Representation of Green's Function Integral Operators Using Wavelet Transforms)</b>	<b>100</b>

# 1 EXECUTIVE SUMMARY

## 1.1 Objectives

The objectives of this program are aimed at the development of controls technology for Smart Structures and Materials systems with large numbers of sensors and actuators. This development focuses on a methodology for designing controllers that control large-scale Smart Structures and Materials systems with potentially thousands of inputs and outputs at a dramatically reduced cost in both computation and input/output interconnection complexity. Moreover, the methodology can be used to implement large-scale controllers that have highly scalable, multiprocessor architectures.

Our program objectives can be summarized as follows:

- Demonstrate an initial proof-of-concept of the wavelet-based method for controlling smart structures and materials with large transducer arrays.
- Develop a practical and mathematically sound methodology for designing and implementing computationally efficient, sparsely interconnected, scalable control systems.
- Validate the new methodology by designing and simulating a control system for control of simple structures using both numerical modeling data and experimentally measured data.

## 1.2 Results

The Control Technology for Smart Materials Program has confirmed the advantages of a multiscale approach to transfer function-based control of systems with very large numbers of transducers. The main results of this program are as follows:

- **Wavelet Control Design Method**

Main result:

Developed design method that exploits wavelet transform compression properties and the Q-parameterization of the controller in producing controller designs that can be implemented with reduced computational processing demands and with a simplification of interconnections from inputs to outputs.

Summary of method:

By using the Q-parameterization of the controller, we can divide the design problem into the two parts. The first part consists of implementing a transfer function that cancels the

coupling from actuator inputs to sensor outputs. The second part consists of designing a feedforward transfer function, "Q", such that its parameters minimize an optimal control cost function. The wavelet control method uses the wavelet transform to compress the coupling transfer function, and uses a spatially banded Q-parameter structure to compress the feedforward transfer function. The result is an overall controller that is sparsely interconnected and that has fewer effective input/output interconnections.

Our design method also exploits temporal bandwidth compression via finite-impulse response (FIR) parameterization of the controller and multirate filtering.

- **Sensor/Actuator Placement Methods and Integration with KIKO**

Main results:

- Developed algorithm for transducer selection. This approach uses a predefined set of candidate actuators or sensors, and selects a fixed, smaller, number of these transducers to maximize their effectiveness. For this purpose effectiveness is defined for actuators as approximating the range of all possible uncontrolled system outputs over a number of frequencies, and for sensors as approximating the span of all possible system disturbance inputs over a number of frequencies.
- Developed approaches for using nonuniform and irregularly bounded distributions of transducers. The result of transducer selection would generally be irregularly placed devices. There is no theoretical basis for benefits of direct application wavelet transformation in this case, so we looked at three ideas to retain the advantage of multiscale methods with irregular spatial placement of transducers.

- **Validation Using Analytical and Numerical models**

Main results:

- Validation of wavelet compression method on Euler-Bernoulli beam model:  
Used transfer function from force inputs to displacement outputs along a beam as example of coupling transfer function. Showed compression performance that agreed with theoretical predictions over wide range of frequencies
- Validation of overall control method on Euler-Bernoulli beam model:  
Successfully controlled displacement along a beam due to wide-band force disturbances. Wide-band control performance achieved using a wavelet-based controller.

- **Validation Using PSU-collected Data**

Main results:

- Validation of wavelet compression method on measured plate transfer function:  
Used  $34 \times 34 \times .125$  inch aluminum plate to measure coupling transfer function.
- Validated smoothness properties of plate using taking numerical approximation of derivatives using measured data
- Validated wavelet compression of transfer function using measured data

### **1.3 Recommendations**

The next logical steps of development are closed-loop hardware demonstration, and further work on advanced wavelets that can treat irregular transducer arrays, accomodate bounded domains, and reduce the break-even point for advantageous application of this technology. The first step is needed to build confidence of potential users, and is justified by the results to date. The second step would be focussed on the most important needs for further theoretical and algorithmic development of the methodology to suit real applications.



## 2 INTRODUCTION

Smart Structures and Materials technology has emerged as a promising new area of engineering research and development. The concept of embedding sensing and actuating devices within a material and/or structure offers the possibility of altering the physical behavior of a system in ways not possible through the use of passive materials alone. The DARPA Smart Structures and Materials program has focused much of its effort on the development of device and embedding technology for initial proof of concept for engineering such systems. The design requirements of embedding devices in materials and structures present formidable challenges to developing device technology capable of performing in applications requiring, for example, the rendering of significant actuation force over a reasonable bandwidth.

The development of active control technology specifically for smart structures and materials, however, has lagged substantially behind that of the base materials, transducers, and embedding techniques. Still, development of smart structures with ever-greater numbers of embedded elements continues, spurred by potential uses that require large arrays of sensors and actuators. For example, several "Smart Skin" concepts are being developed for embedding transducers on the surface of a structure. By placing them on the wing of an aircraft, one increases flight performance by detailed control of the wing's shape, i.e., a "Smart Wing." By embedding transducers in an aircraft cabin's walls, one achieves interior acoustic noise quieting. There is yet another reason for considering an array of transducers on the surface of a structure. Rather than implementing a conventional control design that is sensitive to the particular device layout, a densely sampled array allows the *controller* to optimize the use of sensor information and actuator authority. No control technology suitable for such large arrays exists, however, and this presents a barrier to future applications.

To motivate the objectives of our program, consider the example of controlling a large array of collocated actuator/sensor pairs on a flexible plate as illustrated in Figure 1. Each tile on the surface contains an embedded actuator/sensor pair and the control problem might be, for example, to stiffen the plate by dynamically adjusting the actuator input signals based on dynamically sensing the sensor output signals. In Figure 1, the abundance of communication paths illustrates the complexity involved in mapping the sensor outputs on the surface into a control signal for a single actuator using a fully interconnected control approach. Note that the complexity of this approach in terms of both computational and communications cost increases with the number of actuators being controlled. In the case of full interconnection between every actuator and sensor, the system becomes potentially intractable and highly cost-ineffective.

In this program we develop and demonstrate technology capable of controlling hundreds or thousands of sensors and actuators embedded in the base material. We have dubbed this the "KIKO control problem" (Kilo-Input/Kilo-Output) for Smart Structures and Materials. This program focuses on a new multiscale/multirate theory of hierarchical design based on the wavelet transform. In the context of this theory, we develop efficient and highly scalable

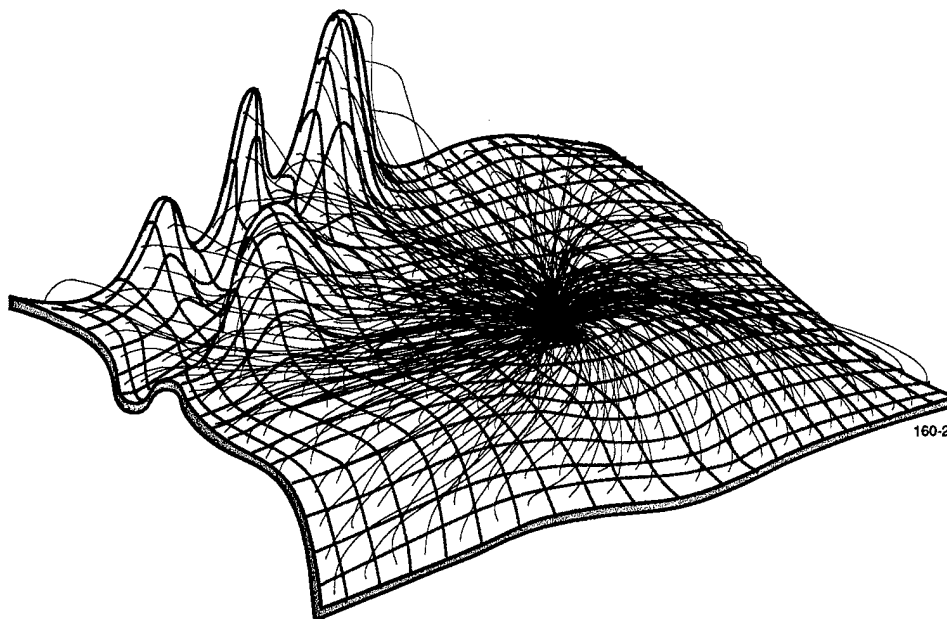


Figure 1: Fully interconnected control approach

implementations of control systems using multiprocessor architectures. This report describes our multiscale control approach and presents simulation results based on model and measured data that provide a first-order proof of concept for our approach.

Our program is aimed at developing a theory and methodology for controlling large numbers of devices for applications such as vibration control and acoustical noise control. The methodology we develop will allow us to implement controllers that can efficiently process large numbers of inputs and outputs. It is highly scalable and will guide us in designing highly structured multiprocessor schemes. The end result is a control system that implements large-scale control at a highly reduced cost in terms of processing hardware and interconnection complexity compared with a conventional approach. Our approach to control design is based on a multiscale hierarchy whose structure is governed by the characteristics of the control system transfer functions as illustrated in Figure 2. Aggregating actuator inputs and sensor outputs into local groups and doing this recursively in scale results in a processing architecture that allows efficient computation and communication between all sensors and actuators. Note that in contrast to locally interconnected control approaches, where sensors and actuators are constrained to communicate within local neighborhoods, our approach allows direct communication from any sensor to any actuator. Thus, while the controller has the same number of degrees of freedom as a fully interconnected controller, it exploits the multiscale hierarchy in significantly reducing computational and communications cost.

This spatial hierarchy also allows us to use a multirate approach to efficiently implement the controller. Thus, we optimize not only spatial properties of the system to reduce interconnection complexity, but temporal bandwidth as well. One of the ultimate features of such a scheme is to allow the control of broadband phenomena over a wide spatial extent and to do

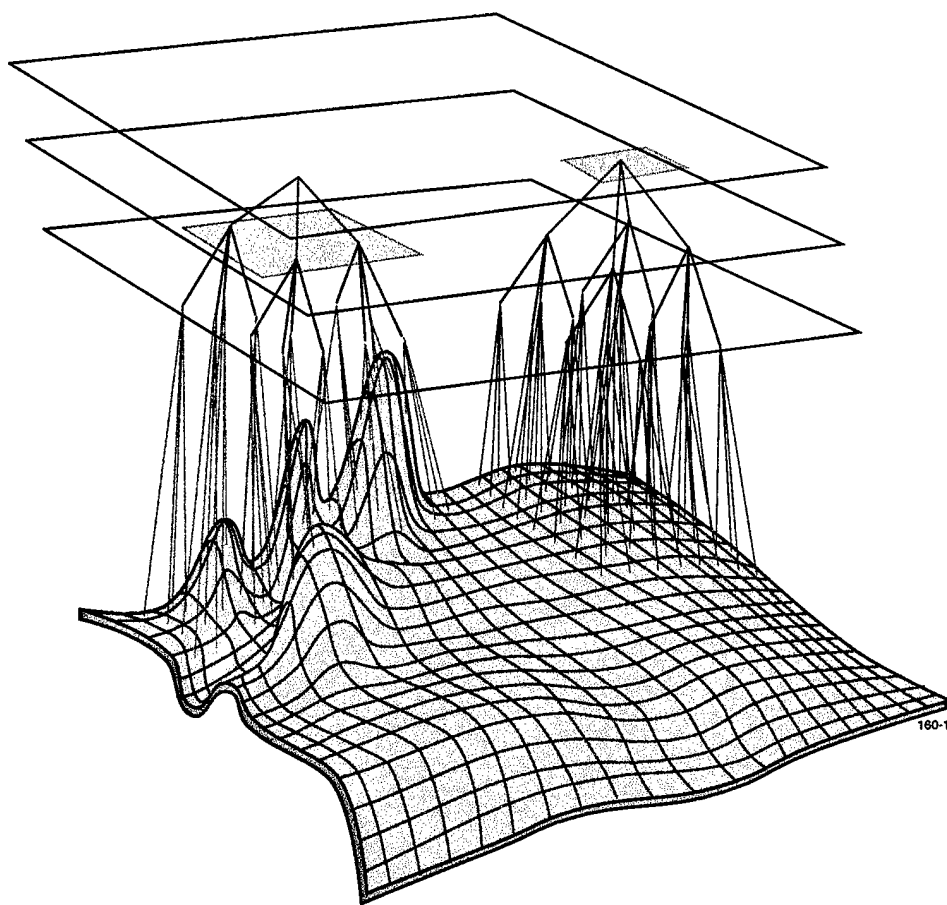


Figure 2: Multiscale control approach

so without having to optimize the layout of a relatively small number of transducers.

This report summarizes the theory developed under this program and describes the multiscale method for controlling smart structures and materials in Sections 4 and 5. Section 1 provides an executive summary of our results. Sections 6 and 7 provide examples of simulations using analytical and numerical models as well as results of applying our method to measured data.

### 3 CONTROL PROBLEM FORMULATION

This section describes the general closed-loop control problem in terms of a block diagram and its associated transfer function equations. The problem formulation applies to a wide range of control problems and provides us with basic notation and a formalism for analyzing closed-loop control systems in terms of stability and robustness. Furthermore, by parameterizing the controller via the Q-parameterization [9], the controller design problem becomes a tractable model-matching problem. SRI is a pioneer in exploiting the Q-parameterization for the design of large-scale systems. The KIKO control approach extends this approach much further by exploiting inherent redundancies in the physical system to achieve dramatic reductions in the computational and communications complexity of the controller.

The block diagram for the basic closed-loop control configuration is depicted in Figure 3. The quadruple of transfer functions  $(T, S, A, P)$  represents various sub-blocks of the overall physical system. In the absence of control, the disturbance propagates through the system  $T$  to produce a response, while the transfer function  $K$  represents the user-designed controller. The transfer function  $T$  represents the uncontrolled response that is to be “matched” or canceled by the control path. The transfer function  $S$  maps the disturbance to the output of the sensors, while  $A$  maps the inputs to the actuators to the physical response variable to be controlled. Finally,  $P$  represents the coupling from actuators to sensors. The overall closed-loop transfer function in Figure 3 from input to output, which we denote  $G$ , is expressed as follows.

$$G = T + A(I - KP)^{-1}KS \quad (1)$$

where each transfer function is a matrix function of frequency and  $I$  denotes the identity matrix, which is constant for all frequencies.

Control problems can be stated in terms of an optimization problem in which the optimal controller is the solution to the minimization of the norm of the transfer function  $G$  with respect to  $K$ .

$$\min_K \|G\| \quad (2)$$

Constraints to this optimization problem include requiring stability of  $G$  as well as insuring robustness of the design with respect to modeling errors in  $(T, S, A, P)$ . Furthermore,  $K$  must be causal, i.e., realizable. An obvious difficulty in solving such a constrained optimization is the nonlinear dependence of  $G$  on  $K$ .

Fortunately, we can simplify the overall optimization problem with the use of the Q-parameterization of the controller  $K$ . Consider the set of controllers given by the formula

$$K = (I + QP)^{-1}Q \quad (3)$$

where  $Q$  is a free transfer function parameter. Such a system  $K$  has a natural implementation as a multi-input/multi-output (MIMO) feedback system as depicted in Figure 4. The basic theorem resulting from this parameterization is the following [9]:

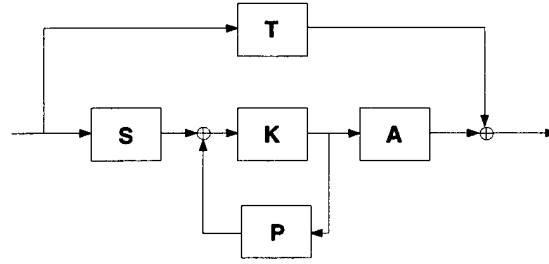


Figure 3: Block diagram of basic closed-loop system

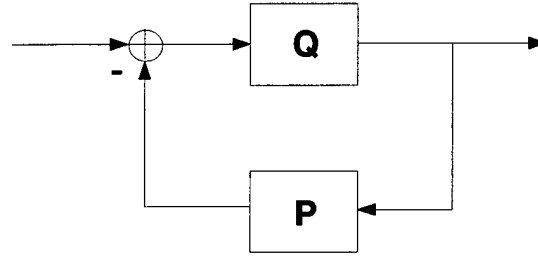


Figure 4: Block diagram of Q-parameterized controller

- Referring to Figure 3 and eq.(3), for stable  $P$ , the collection of stable  $Q$ 's parameterize the collection of  $K$ 's that stabilize the closed-loop system  $G$ .

The design implications of this theorem are far-reaching. In particular, by substituting eq.(3) into eq.(1), we get the following expression for  $G$ :

$$G = T + AQS \quad (4)$$

Essentially, we have transformed  $G$  from a nonlinear function of  $K$  into an *affine* function of  $Q$ . Furthermore, the overall optimization problem as stated in eq.(2) reduces to the following model matching problem [9].

$$\min_Q \|T + AQS\| \quad (5)$$

If we restrict  $Q$  to be stable, then, via the Q-parameterization theorem, we satisfy the requirement that the overall closed-loop system  $G$  be stable.

For practical reasons, we would like to design our controller to be robust to unmodeled errors in the overall system. Indeed, one of the main reasons for designing feedback systems is to make a system insensitive to modeling errors or changes in plant parameters. For example, consider the case where we have additive plant errors. In

$$\tilde{P} = P + D \quad (6)$$

$P$  represents the nominal plant and  $D$  is a stable transfer function that represents a frequency-dependent additive error. In this case, the loop gain of our system,  $G$ , is equal to  $DQ$ , and by

the small gain theorem [8], the following is a sufficient condition for stability of  $G$  given the nominal plant  $P$  and the plant errors as in eq.(6).

$$\|DQ\|_{\infty} < 1 \quad (7)$$

where the  $\infty$ -norm of a stable matrix transfer function is the supremum of the maximum singular value of the matrix over all frequencies. A version of the robust control design problem, then, is using the nominal plant  $P$  as our plant model and solving eq.(5) for  $Q$  under the constraint given in eq.(7) as  $D$  varies.

Finally, we consider the computational complexity of implementing a controller as given in eq.(3). One of the main difficulties in implementing a controller with large numbers of sensors and actuators is the fact that we must map dynamically all of the sensor outputs into all of the actuator inputs. In the  $Q$ -parameterization realization of the controller, the implementation problem can be divided into two steps:

Step 1. Implementing a model of  $P$  as a transfer function from actuator inputs to sensor outputs (sometimes referred to as the *neutralization* path).

Step 2. Implementing  $Q$  as a transfer function from sensor outputs to actuator inputs (sometimes referred to as the *feedforward* control path).

Thus, if  $P$  and  $Q$  are full matrices over a wide band of frequencies, the computational complexity of implementing a controller with large numbers of sensors and actuators becomes significant. For example, suppose  $P$  and  $Q$  were implemented as matrix finite impulse response (FIR) filters and there were  $N_s$  sensors and  $N_a$  actuators. The number of multiplications and additions required to perform a *single* tap filter operation is  $2N_sN_a$ . Moreover, the communications complexity scales poorly, as illustrated in Figure 1.

Finally, the computational complexity scales linearly with the number of taps of each FIR filter, motivating the need for multirate processing. Our multiscale hierarchy gives rise to a controller in which some channels are sampled at a lower rate, while others are processed using shorter FIR filters.

## 4 WAVELET CONTROL DESIGN METHOD

### 4.1 Overview

In this section we describe in detail the KIKO control design method. The method is based on the Q-parameterization of the controller and the wavelet decomposition of particular system transfer functions in this parameterization. Referring to the block diagram in Figure 4, the controller can be designed and implemented in terms of the feedforward transfer function, "Q," and the feedback or neutralization path, "P." Motivated by our twin objectives of reducing computational and communications complexity of the controller, we develop methods for designing the two transfer function paths such that they are both sparse and have regular structure. Sparsity is a mathematical property that translates into reduced computation in implementing the controller, while regularity of the input/output mapping of the transfer functions can be exploited to build multiprocessor architectures that are interconnected in a simple, scalable fashion.

### 4.2 Change of Basis for Control Problem

In this section we address the problem of simplifying the computations required to implement a controller  $K$  via a change of basis in both the space of sensor outputs (i.e., the domain of the transfer function  $S$ ) as well as the space of actuator inputs (i.e., the domain of the transfer function  $A$ ). The main idea behind reducing the computational requirements of the controller via a change of basis consists of (1) using basis transformations to decouple both the neutralization and feedforward transfer functions, i.e., making the transformed transfer functions  $P$  and  $Q$  sparse, and (2) using basis transformations that are computationally efficient and structured in such a way as to be easily implementable in digital hardware. In the following we define notation and a formalism for describing and analyzing such an idea.

From the previous section, and in particular from the parameterization of the controller  $K$  as given in eq.(3), there are two matrix transfer functions for which we would like to consider basis transformations as a way of simplifying implementation, namely,  $P$  and  $Q$ . For our control applications,  $P$  and  $Q$  are in general full transfer function matrices over the band of interest, necessitating fully interconnected systems for carrying out steps 1 and 2 from the previous section. The intent of performing basis transformations on these transfer functions is to sparsify the required interconnections via highly structured, computationally efficient basis transformations. We restrict ourselves to the case of frequency-independent bases (constant matrices). In particular, we define the following:

$$\tilde{P} = X_l P X_r^{-1} \quad (8)$$

$$\tilde{Q} = Y_l Q Y_r^{-1} \quad (9)$$



Note that for both  $P$  and  $Q$ , *separate* basis transformations are performed for the domain and range of each respective matrix transfer function. Indeed, neither  $P$  nor  $Q$  is necessarily square. Note, however, that in the case of square  $P$  ( $Q$ ), if  $X_r^{-1} = X_l^{-1}$  ( $Y_r^{-1} = Y_l^{-1}$ ), then  $X$  and  $Y$  can be viewed as similarity transformations.

The efficiency of a change of basis in reducing computational complexity depends on (1) the sparseness of  $\tilde{P}$  and  $\tilde{Q}$ , i.e., the interconnections required in realizing  $\tilde{P}$  and  $\tilde{Q}$ , and (2) the computational complexity of the basis change transformation. To see this more explicitly, consider that the implementational requirements of a system implemented in bases  $X$  and  $Y$  can be divided into the following two tasks, which correspond to the two tasks as defined in the previous section for implementing the controller  $K$ .

1. Neutralization:

$$X_l^{-1} \tilde{P} X_r \quad (10)$$

2. Feedforward:

$$Y_l^{-1} \tilde{Q} Y_r \quad (11)$$

In general it is not clear to what extent one can sparsify  $P$  and  $Q$ , i.e., render basis coefficients precisely equal to zero, by using basis transformations  $X$  and  $Y$  that are computationally efficient to implement. For example, Jordan and Schur canonical forms [10] offer similarity transformations of a matrix into nearly diagonal and triangular forms, respectively. In both cases, however, full transformation matrices are involved with  $O(N^2)$  computational complexity required for performing the transformations.

Our approach to sparsifying the control transfer functions  $P$  and  $Q$  using basis transformations is to develop a methodology for trading off sparsity of the transformed transfer functions with both computational and implementational complexity of the transformations. To develop this methodology we need tools for characterizing this tradeoff in terms of analytical properties of  $P$  and  $Q$ . In particular, we base our methodology on tools developed in the context of wavelet transform theory [17]. Within the context of wavelets, as will be described in the following section, we have available a class of extremely fast ( $O(N)$ ) basis transforms that have the added capability of sparsifying physical operators. Furthermore, the degree to which an operator can be made sparse can be characterized in terms of mathematical characteristics of the operator, such as its smoothness.

In summary, our approach to multiscale control is to perform multiscale basis transformations on  $P$  and  $Q$  and implement the controller in the space of multiscale basis coefficients. We design our transforms so as to make the basis coefficients as decoupled as possible. This will necessarily involve, as will be explained in the following sections, approximations of  $P$  and  $Q$ . However, we will be able to arbitrarily trade off approximation precision with sparsity in a structured way.

### 4.3 Multiscale Bases

In this section we describe an approach to multiscale control that is based on a class of basis transformations corresponding to the compactly supported, orthonormal wavelet transform described in Daubechies [7]. The advantages of using this particular class of transforms for performing basis transformations on the plant  $P$  and the control parameter  $Q$  are threefold: (1) these transforms take advantage of scale-recursive algorithms that are extremely efficient ( $O(N)$ , where  $N$  is the number of samples of the discrete signal to be transformed); (2) the basis functions can be designed to be extremely effective in compressing operators, e.g., reducing the interconnectivity of transfer functions such as  $P$  and  $Q$ ; and (3) by doing a spatial scale decomposition using wavelets, we actually perform an approximate modal decomposition that allows us to process fine-scale coefficients (representing higher modes that are more highly damped) using shorter impulse responses, and coarse-scale coefficients (representing lower modes that are of narrower bandwidth) using lower sampling rates. Section 4.3.1 gives a brief overview of orthonormal wavelet bases. Section 4.3.2 discusses results of using these bases to sparsify operators.

#### 4.3.1 Orthonormal Wavelets of Compact Support

The basic structure of any scale-based wavelet basis is based on the property that a space of functions, for example  $L^2(\mathcal{R})$ , can be spanned by a basis set consisting of dilations and translations of a single, properly chosen function.

$$\{\Psi(2^m x - n) \text{ for } m, n \text{ integer}\} \quad (12)$$

The basic wavelet function  $\Psi$  in eq.(12) is in general oscillatory and compressed in  $x$ , hence the name. For our purposes one of the most interesting aspects of bases of the type in eq.(12) is the fact that under certain conditions, transforming a signal in these basis functions can be interpreted as performing what is known as a *multiresolution analysis* of the signal [12]. In this analysis, the signal is represented at different resolutions using a *scaling function*,  $\Phi$ , which is used to blur the signal at these resolutions.

The multiresolution analysis interpretation of the wavelet transform can be summarized by the following key points.

- The translations of the scaling function for a fixed-scale  $m$ ,  $\{\Phi(2^m x - n) \text{ for } n \text{ integer}\}$ , define a subspace of  $L^2(\mathcal{R})$ . Representing a signal at this scale is achieved by projecting the signal onto this subspace.
- The translations of the wavelet function for a fixed-scale  $m$ ,  $\{\Psi(2^m x - n) \text{ for } n \text{ integer}\}$ , span the subspace defined by the difference between the scaling subspace at scale  $m$  and the scaling subspace at scale  $m - 1$ .

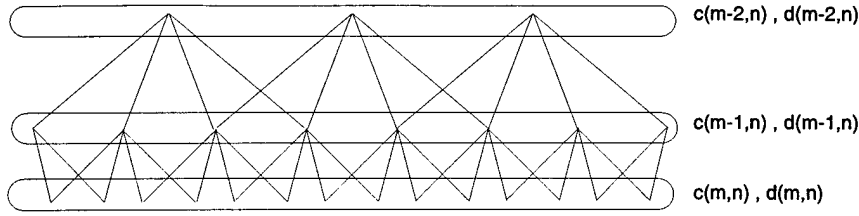


Figure 5: Domain of wavelet coefficients on a multiscale lattice

- The wavelet basis coefficients can be computed *recursively* in scale, resulting in an extremely efficient procedure.

In Daubechies[7], extensions of the Haar wavelet are derived for a class of wavelets that are compactly supported and orthonormal. Furthermore, a characteristic of this class of wavelets is that their transforms can be computed efficiently via a scale recursion as illustrated in the Haar case. Let us define the scaling coefficients and wavelet coefficients as follows for some signal  $f(x)$ .

$$c(m, n) = \int_{-\infty}^{\infty} \Phi(2^m x - n) f(x) dx \quad (13)$$

$$d(m, n) = \int_{-\infty}^{\infty} \Psi(2^m x - n) f(x) dx \quad (14)$$

It can be shown [7] that the following recursion can be used to compute the scaling and wavelet coefficients recursively in scale from fine to coarse.

$$c(m, n) = \sum_k c(m+1, k) h(2n - k) \quad (15)$$

$$d(m, n) = \sum_k c(m+1, k) g(2n - k) \quad (16)$$

Each of the recursions in eqs.(15,16) can be interpreted as discrete filtering followed by down-sampling by a factor of two. The scaling function filter  $h(n)$  is related to the wavelet filter  $g(n)$  by:  $g(n) = (-1)^n h(1 - n)$ . Furthermore, for compactly supported wavelets,  $h(n)$  and  $g(n)$  are FIR filters (typically of length  $< 12$ ). The computational complexity for the algorithm described by eqs.(15,16) is order  $O(NL)$ , where  $L$  is the length of  $h$  and  $g$ , and  $N$  is the number of coefficients at the initial (finest) scale. The algorithm flow is illustrated in Figure 5 for the case of 4-tap FIR filters  $h$  and  $g$ , where the  $c$  and  $d$  coefficients are computed recursively up the lattice. The algorithm is initialized at the finest scale with the sequence  $c(M, n)$ , where  $M$  is the finest scale and  $c(M, n)$  is the signal to be transformed.

The inverse transform, i.e., reconstructing the scaling coefficients at the finest scale from wavelet coefficients at all coarser scales, consists of the following recursion in scale from coarse to fine.

$$c(m+1, n) = \sum_k c(m, k) h(n - 2k) + \sum_k d(m, k) g(n - 2k) \quad (17)$$

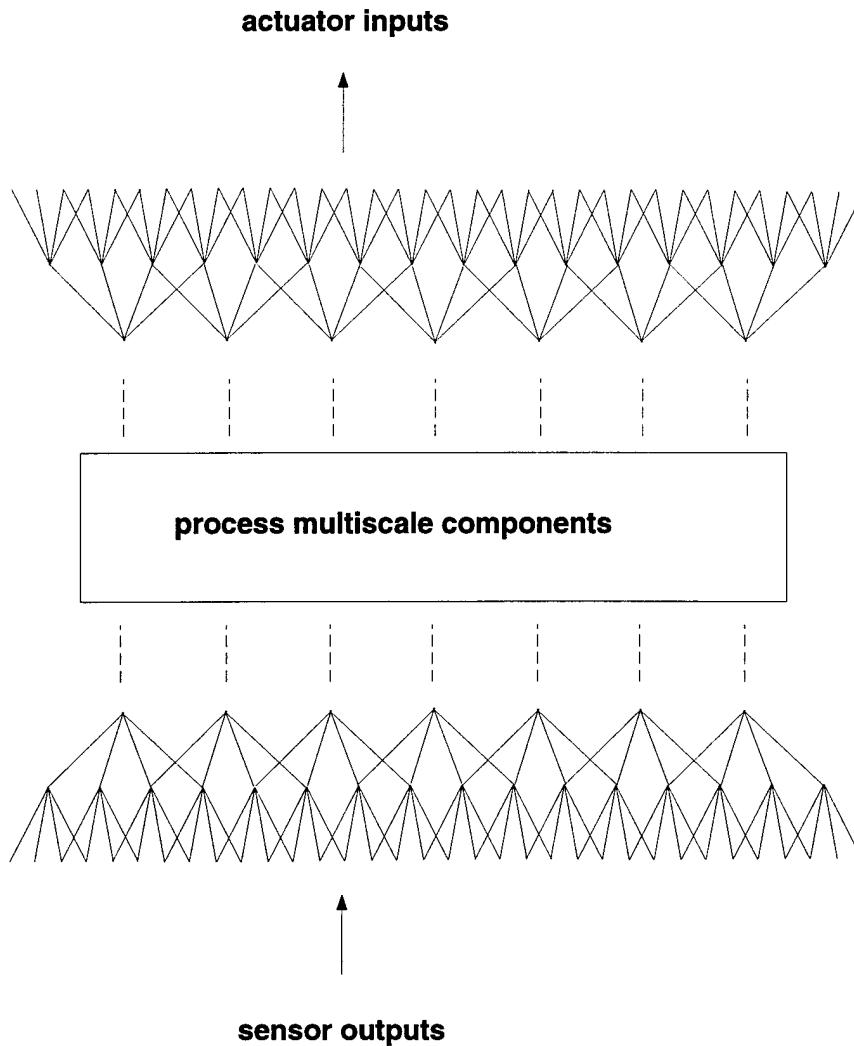


Figure 6: Multiscale basis transformation for control

The algorithm flow would correspond to propagating down the lattice in Figure 5. Again, the computational complexity is  $O(NL)$ .

What these fast wavelet algorithms suggest is the possibility for performing basis transformations on our control transfer functions  $P$  and  $Q$ , and, if the basis coefficients behave in a decoupled fashion, for performing local computations on each basis coefficient to implement the control law. Furthermore, the lattice algorithm suggests a scheme for parallel processing in which processors are assigned to each node in the lattice. Figure 6 illustrates a block diagram of the flow of information involved in implementing the feedforward path of the controller. The neutralization path is similar but runs in the opposite direction, i.e., from actuator inputs to sensor outputs.

### 4.3.2 Compression Properties of Wavelets

In this section we review some results in Beylkin [2] on using wavelets to compress or sparsify operators. These results motivate our use of wavelet bases to do multiscale control in that we exploit wavelet compression properties to sparsify our control transfer functions. This allows us to implement our control law in multiscale bases in which basis coefficients are modified in a decoupled fashion.

One of the main ideas in using wavelets to compress operators is to take advantage of the fact that the wavelet bases designed in Daubechies [7] can be used to efficiently represent smooth operators. The property of these wavelets that allows such compression is one that is referred to as the property of "vanishing moments." This property is described as follows.

$$\int_{-\infty}^{\infty} \Psi(x) x^m dx = 0 \text{ for } m = 0, 1, \dots, M-1 \quad (18)$$

It is also true that the number of vanishing moments,  $M$ , is proportional to the support length of the wavelet or the length of the discrete filters  $h(n)$  and  $g(n)$ .

The reason this property is essential to compressing smooth operators is the fact that when integrated against a wavelet basis function,  $\Psi(2^m x - n)$ , satisfying eq.(18), a function  $f(x)$  is equal to  $f(2^{-m}n)$  plus derivatives of  $f$  of order greater than or equal to  $M$ . For smooth functions, these higher-order derivatives are small, and thus the wavelet coefficients are small. What this means for operators is that we can relate compression efficiency of the wavelet basis in terms of smoothness properties of the operator. Beylkin [2] considers the class of Calderon-Zygmund integral operators, which have the property of being smooth away from the diagonal. In particular, 2D operators  $K(x, y)$  in this class satisfy the following:

$$|K(x, y)| \leq \frac{1}{|x - y|} \quad (19)$$

$$|\partial_x^M K(x, y)| + |\partial_y^M K(x, y)| \leq \frac{C_M}{|x - y|^{1+M}} \quad (20)$$

From the fact that the  $M$ th partials of  $K$  decay strongly away from the diagonals along with the vanishing moment property in eq.(18), one can show that the wavelet coefficients decay in a similar fashion as a function of the distance between coefficients, i.e., the distance between the centers of the basis functions corresponding to two coefficients.

Our control transfer functions  $P$  and  $Q$  will of course not be as simple as the operators in the Calderon-Zygmund class. In fact they are frequency-dependent and depend heavily on boundary conditions and material properties of the structure on which the actuators and sensors reside. Our multiscale approach is based on detailed characterization of  $P$  and  $Q$  in terms of their smoothness properties and any possibly existing singularities. We will tailor our multiscale bases to take advantage of the smoothness of these transfer functions. The key issue is in trading off complexity and regularity of the transform, for example as illustrated in the lattice of Figure 5, and the efficiency realized by such a transform, with the complexity of the

transfer functions as measured by their degree of smoothness as a function of position (for example position of actuators and sensors on the structure).

#### 4.4 Designing Neutralization Path $P$

The theoretical basis for making our neutralization transfer function  $P$  sparse in the wavelet domain is based on viewing this transfer function at each frequency as a spatial, Green's function operator that maps inputs (i.e., actuator inputs in some spatial domain), into outputs (i.e., sensor outputs in that domain). A simple example of such an operator is the mapping from normal force inputs along a beam to normal velocities measured along the beam. Our analysis applies to general operators along surfaces; thus, in particular, we can treat the case of 3D structures with transducers embedded on their surfaces.

In analyzing the structure of our transformed Green's function operator,  $K$ , we have determined that the following key properties of  $K$  can be used to compress  $K$  using wavelet transforms. Note that  $K(x, y)$  is notation for a general input/output Greens's function operator where  $y$  is variable representing actuator location, while  $x$  is variable representing sensor location.

1.  $K(x, y)$  is smooth for  $x \neq y$  (i.e., all its derivatives are continuous).
2.  $K(x, y)$  has a discontinuous  $L$ th partial derivative in both  $x$  and  $y$  evaluated at the point  $x = y$ .

From these properties we can determine the structure of the transformed  $K$ . The transformed  $K$  maps wavelet transforms of the inputs to wavelet transforms of the outputs. At any particular scale a wavelet coefficient corresponds to the inner product of a wavelet function with a set of inputs (outputs). At that scale, the wavelet coefficient corresponding to a set of outputs is a function of the wavelet coefficient of the inputs at that scale at locations coincident with the outputs and the wavelet coefficients corresponding to outputs at neighboring locations. The output wavelet coefficient is also a function of input wavelet coefficients at other scales, but again the dependence involves only input locations neighboring the outputs. This local dependence in scale and position characterizes the sparseness of Green's function operators in the wavelet domain, and is the basis for our development of sparsely interconnected neutralization filters. A more precise statement and more detailed analysis of the dependence of the transformed operator on scale and position is found in [3].

Figures 7 and 8 are plots of the magnitude of the Green's function at 1000 Hz and 5000 Hz, respectively, where  $x$  and  $y$  are uniformly sampled with 128 points over the interval  $[0, 1]$ .

Figures 9 and 10 are plots of the magnitude of the wavelet transform of the Green's function at 1000 Hz and 5000 Hz, respectively. Thus, these figures depict the operator mapping wavelet

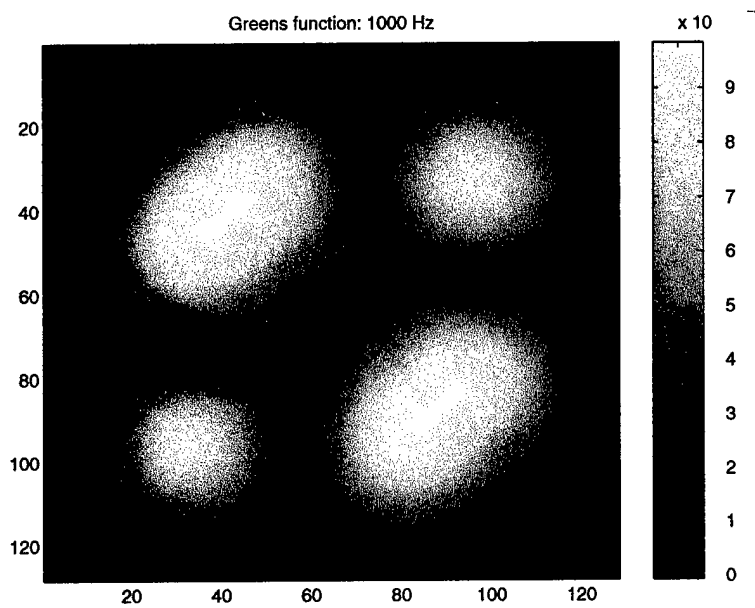


Figure 7: Intensity image of magnitude of Green's function at 1000 Hz

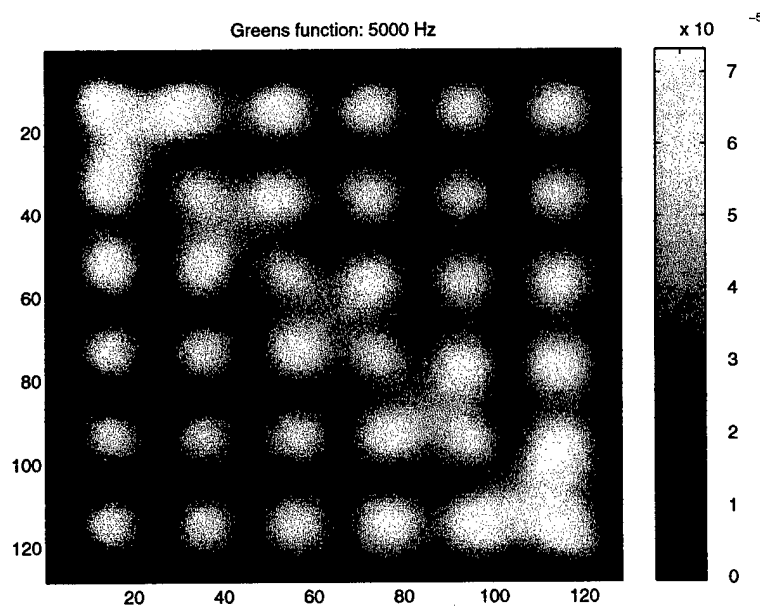


Figure 8: Intensity image of magnitude of Green's function at 5000 Hz

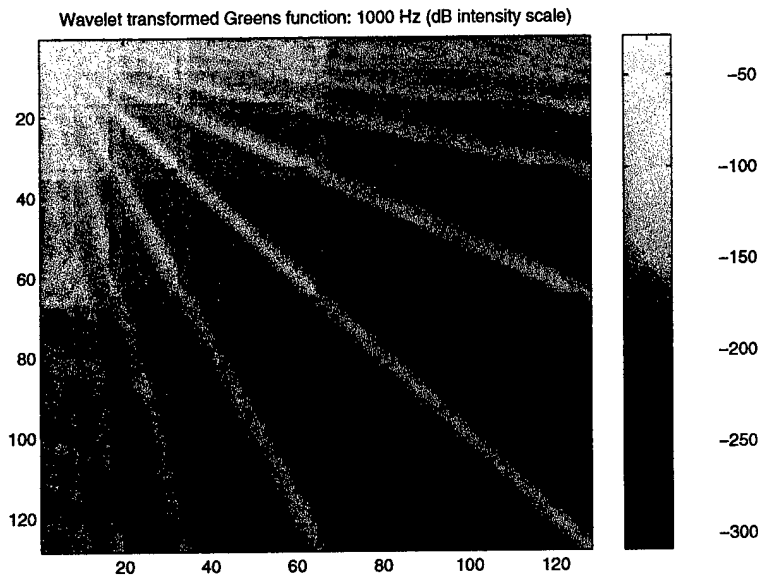


Figure 9: Intensity image of magnitude of wavelet-transformed Green's function at 1000 Hz (intensity plotted in dB)

coefficients of the forcing inputs into wavelet coefficients of the sensing outputs. Note that the intensities in these plots are plotted in a dB scale due to the fact that coarse-scale coefficients dominate in energy over many of the finer-scale coefficients.

In Figure 11 we show the coefficients of the wavelet-transformed Green's function at 1000 Hz greater than  $1e - 5$  times the norm of the Green's function. Note that the set of remaining coefficients is small, making the wavelet-transformed operator extremely sparse. Similar results are obtained for the Green's function at 5000 Hz, as shown in Figure 12.

## 4.5 Designing Feedforward Path $Q$

In this section we point out a significant difference between designing a multiscale version of  $P$  and designing a multiscale version of  $Q$ . In the case of the transfer function  $P$ , we are simply finding the best approximation of the true plant transfer function characteristics in a multiscale basis via the transformations described in the previous section. In the case of the transfer function  $Q$ , however, we actually *design*  $Q$  to optimize our control objective. Thus, we have the freedom to implement  $Q$  with arbitrary sparsity and structure, for example, trading off performance for increased sparsity. We have investigated two different sparse, regular structures for designing and implementing  $Q$ . The first is the design of  $Q$  in the same multiscale basis as used to approximate  $P$ , while the second is to design a "banded"  $Q$  in the spatial domain that leads to implementing a locally interconnected feedforward path.



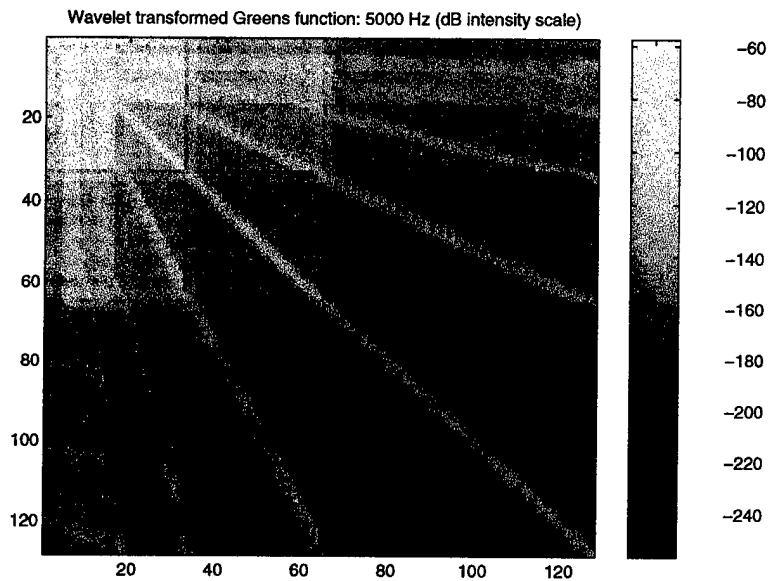


Figure 10: Intensity image of magnitude of wavelet-transformed Green's function at 5000 Hz (intensity plotted in dB)

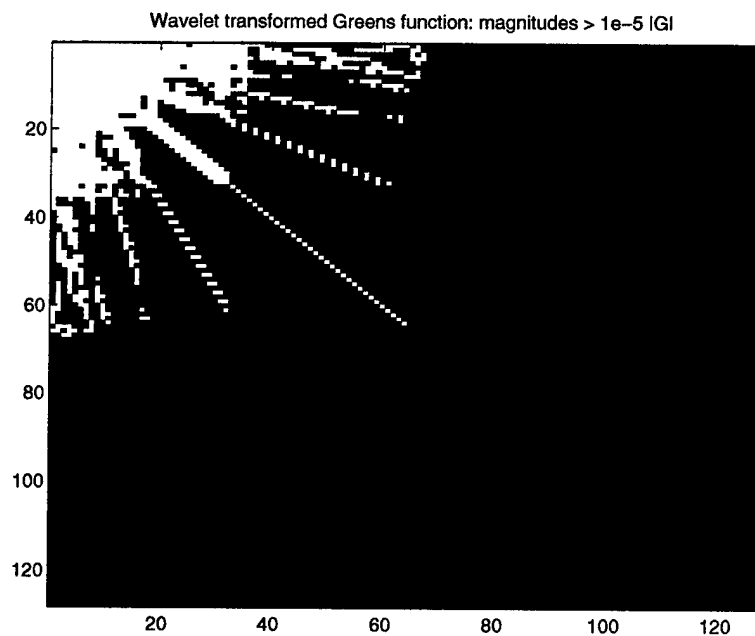


Figure 11: Intensity image of magnitude of wavelet-transformed Green's function at 1000 Hz: coefficients greater than  $1e-5$  times norm of  $K$

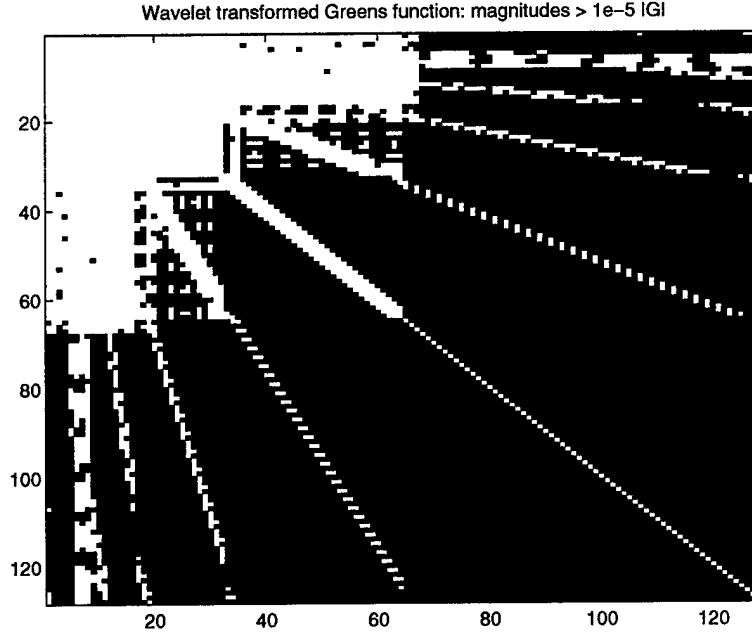


Figure 12: Intensity image of magnitude of wavelet-transformed Green's function at 5000 Hz: coefficients greater than  $1e-5$  times norm of  $K$

#### 4.5.1 Optimizing $Q$ in Multiscale Bases

We can rewrite the optimization problem in eqs.(5,7) as

$$\begin{aligned} \min_{\tilde{Q}} \quad & \|T + \tilde{A}\tilde{Q}\tilde{S}\| \\ & \|\tilde{D}\tilde{Q}\|_{\infty} < 1 \end{aligned} \quad (21)$$

where

$$\tilde{A} = AY_l \quad (22)$$

$$\tilde{S} = Y_l^{-1}S \quad (23)$$

and  $\tilde{D}$  is *not* necessarily related to  $D$  via a transformation with  $Y_l$ . Note that eq.(21) and eqs.(5,7) are equivalent due to the orthonormality of the wavelet transform represented by  $Y_l$ . In order to redesign  $Q = Y_l^{-1}\tilde{Q}Y_r$  to be sparse in its multiscale representation, we constrain  $\tilde{Q}$  to have local interconnections by zeroing out the appropriate entries of its matrix representation. We then solve eq.(21) for a sparse version of  $\tilde{Q}$ , whose interconnections are local.

#### 4.5.2 Banded (Locally Interconnectd) $Q$

We define a banded  $Q$  to be one whose matrix representation at each frequency is banded, i.e., the matrix is non-zero at entries some fixed number of entries to the right and left of

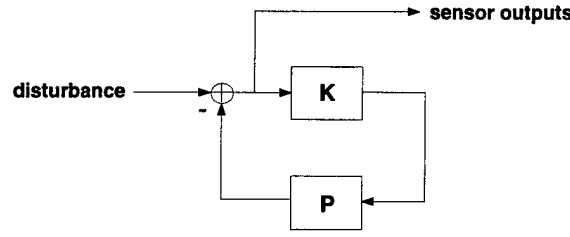


Figure 13: Disturbance rejection block diagram

the diagonal and zero everywhere else. We show in this section that the optimal  $Q$  for a general disturbance rejection problem is indeed a banded operator in the spatial domain at each frequency. We also show that, using our wavelet parameterization for the plant, the optimal  $Q$ -parameter is in fact “finger-like” in precisely the same way as the plant is in the wavelet domain. The thrust of the development is based on finite difference approximations to the partial differential equation (PDE) associated with the physics of the plant.

The disturbance rejection problem we are considering is the following, where we assume  $P$  is a stable matrix transfer function:

$$\min_K \|P(I - KP)^{-1}\|_2 \quad (24)$$

where  $K \in H_2$ . The block diagram for this problem is shown in Figure 13, where  $P$  is the transfer function from actuator inputs to sensor outputs.

In  $Q$ -parameterized form, where we assume the neutralization transfer function is equal to  $P$ , the problem becomes

$$\min_Q \|P + PQP\|_2 \quad (25)$$

for  $Q \in H_2$ .

We show in the following that for systems governed by linear PDEs, the optimal transfer function,  $Q$ , is a banded matrix transfer function. Furthermore, the band is purely a function of the differential operator associated with the PDE. We then show that banded matrix transfer functions in the wavelet domain have the same multiband or “finger-like” structure as  $P$  does. Thus, in the wavelet domain  $Q$  has the same basic structure as  $P$ .

### 4.5.3 Continuous Solutions

Since  $P$  represents the coupling from actuator inputs to sensor outputs, where the sensors and actuators are located, e.g., on the surface of a structure, we model  $P$  as a sampled version of a frequency-dependent Green’s function integral operator that maps physical input variables on the surface (e.g., normal forces) to physical output variables on the surface (e.g., normal velocities). This Green’s function operator is associated with the partial differential operator

$\Phi_{x,t}$  that contains partial derivatives with respect to the space and time variables  $x$  and  $t$ , respectively. For example, the following partial differential operator corresponds to the case of the Euler-Bernoulli beam.

$$\Phi_{x,t} = c_1 \frac{\partial^4}{\partial x^4} + c_2 \frac{\partial^4}{\partial x^4} \frac{\partial}{\partial t} + c_3 \frac{\partial^2}{\partial t^2} + c_4 \frac{\partial}{\partial t^2} \quad (26)$$

where the  $c_i$ 's are functions of  $x$  and  $t$ . For the analysis in this report, we consider the class of linear PDEs. To make the specification of the PDE well-posed we must also include boundary conditions. To do this we specify the initial conditions of the system as well as the surface boundary conditions.

We define  $G(x, t, x', \tau)$  to be the *Green's function kernel*.<sup>1</sup> The Green's function integral operator maps an input function  $f(x, t)$  (e.g., the applied force on a structure) into an output function  $u(x, t)$  (e.g., the resulting normal velocity on a structure due to the forcing function) as follows:

$$\int \int G(x, t, x', \tau) f(x', \tau) dx' d\tau = u(x, t) \quad (27)$$

The partial differential operator is the inverse of the Green's function integral operator in the following sense, which defines the Green's function.

$$\Phi_{x',\tau} G(x, t, x', \tau) = \delta(x - x') \delta(t - \tau) \quad (28)$$

Note that  $G(x, t, x', \tau)$  can be viewed as the *causal* solution to an initial value problem with forcing that is a spatial impulse at  $x'$ .

Recall that  $Q$  is the solution to the optimization problem in eq.(24). In the continuous domain, eq.(28) shows that the operator  $\Phi_{x,t}$  is in fact equal to the optimal solution  $Q$ , since it sets the cost function equal to zero and is a causal operator. We now show that the discretization of the continuous differential operator  $\Phi_{x,t}$  is in fact a banded matrix with respect to the spatial variable  $x$ . Thus, at each point in time (or frequency if represented in the frequency domain), the discretized operator  $\Phi$  is a locally interconnected transfer function.

#### 4.5.4 Discrete Solutions

For practical systems we must model  $P$  as a sampled version of a frequency-dependent Green's function integral operator. Since the optimal  $Q$  is defined in terms of this  $P$ , we analyze the relationship between the continuous space/time characterization of the system given in the previous section and a discrete approximation to this. We do this by using a *finite difference* approximation of the differential operator,  $\Phi_{x,t}$ . This approximation preserves the banded structure of the operator and in particular converts the differential operator  $\Phi_{x,t}$  into a banded

<sup>1</sup>Whereas in the mathematical physics literature the Green's function is associated with the integral over the spatial variables for a fixed frequency, we are considering the function to vary in space and time, with the integral taken over both space and time variables.

matrix at each point in time. We will now show that in the discrete, sampled case, the control objective function, eq.(25), is small using the banded finite approximation of  $\Phi_{x,t}$ . By small, we mean that the value of the objective function in eq.(25) is on the order of  $h^n$ , where  $h$  is the spacing between samples and  $n$  is the order of the differential operator. The analysis is performed for the case of the Euler-Bernoulli beam but can be generalized to the larger class of linear PDEs.

Consider the finite difference approximation of the Euler-Bernoulli beam equation.

$$\left. \frac{du}{dx} \right|_{x_0} \approx \frac{u(x_0) - u(x_0 - \Delta)}{\Delta} \quad (29)$$

The discrete difference operator is defined as follows.

$$D_{i,j} = [00\dots d\dots 00] \quad (30)$$

$$d = \frac{1}{\Delta^4} [1 \quad -8 \quad 28 \quad -56 \quad 70 \quad -56 \quad 28 \quad -8 \quad 1] \quad (31)$$

This operator is in fact a banded matrix, which implies a locally interconnected transfer function at any particular frequency. We will denote this matrix as  $\Pi$ .

If the discrete, finite difference operator  $\Pi$  is well-posed, it has an inverse, represented by the operator  $P'$ . Furthermore, if  $\Pi$  is consistent and convergent (this is true for our finite difference approximation [14]), then its inverse,  $P'$ , applied to an arbitrary  $f$  satisfies the following:

$$u = Pf \quad (32)$$

$$u' = P'f \quad (33)$$

$$\|u - u'\| = O(h^n) \quad (34)$$

where  $n$  is the order of the finite difference operator.

$$\|(P - P')\| \|f\| \leq O(h^n) \quad (35)$$

$$\|P(I + QP)\|_2 = \|P(I + QP' + Q(P - P'))\|_2 \quad (36)$$

Let  $Q = -\Pi$ . Then,

$$\|P(I + QP)\|_2 = \|PQ(P - P')\|_2 \quad (37)$$

$$\leq \|PQ\|_2 \|(P - P')\|_2 \quad (38)$$

$$\leq \|PQ\|_2 O(h^n) \quad (39)$$

We can bound  $\|PQ\|_2$  as follows.

$$\|PQ\|_2 = \|(P - P')Q + P'Q\|_2 \quad (40)$$

$$\leq \|(P - P')Q\|_2 + \|P'Q\|_2 \quad (41)$$

$$\leq \|(P - P')\|_2 \|Q\|_2 + \|I\|_2 \quad (42)$$

$$\leq \|Q\|_2 O(h^n) + 1 \quad (43)$$

Thus,

$$\|P(I + QP)\|_2 \leq O(h^n) + \|Q\|_2 O(h^{2n}) \quad (44)$$

Eq.(44) shows that the use of  $Q$  which equals the discrete approximation of the differential operator results in a cost function that is arbitrarily small as a function of sensor/actuator sampling distance  $h$ . Since  $Q$  is in fact a banded matrix, this result motivates the use of a banded  $Q$  for design of the optimal feedforward transfer function.

#### 4.5.5 Structure of Banded Matrices in Wavelet Domain

In this section, we show that banded  $Q$  designs can be implemented as sparsely interconnected transfer functions in the wavelet domain. We define our banded operator  $Q$  at a particular frequency as

$$Q(x, x') = 0, |x - x'| > (B - 1)/2 \quad (45)$$

where the width of the band is  $B$ ,  $x$  is the actuator input position, and  $x'$  is the sensor output position.

We now show that the wavelet transform of the banded operator  $Q$  gives the same sparse “finger-like” structure that our neutralization transfer function has. Consider the following wavelet-transformed operator  $Q$ .

$$\alpha_{m,n,\bar{m},\bar{n}} = \int_{2^{-m}n}^{2^{-m}(n+1)} \int_{2^{-\bar{m}}\bar{n}}^{2^{-\bar{m}}(\bar{n}+1)} Q(x, x') \psi(2^m x - n) \psi(2^{\bar{m}} x' - \bar{n}) dx dx' \quad (46)$$

where  $\psi$  has  $M + 1$  vanishing moments. From eq.(45) and the fact that the wavelet function  $\psi(2^m x - n)$  has support width  $2^{-(2M-1)}$ , we deduce that  $\alpha_{m,n,\bar{m},\bar{n}} = 0$  when  $|x - x'| > (B - 1)/2 + M$ . Thus, the coefficients of  $Q$  in the wavelet domain exhibit the same sparse structure that is exhibited by the neutralization transfer function.

## 4.6 Summary of Multiscale/multirate Methodology

A major benefit of doing our multiscale decomposition of the controller, aside from simplifying the controller interconnections, is the fact that for both the neutralization and feedforward

paths the fine-scale components will in general have shorter impulse responses, while coarse-scale components have lower bandwidth. This allows shorter FIR filters to be used to control fine-scale components, while coarse-scale components can be controlled at a slower sampling rate. We summarize the steps involved in our multiscale/multirate control methodology for designing and implementing a multiscale/multirate controller as follows.

#### 4.6.1 Wavelet-Based Neutralization Path

- We determine our model of the plant transfer function  $P$  from calibration measurements using an FIR model. This identified model forms the basis of our neutralization transfer function.
- We choose a wavelet basis with a certain number of vanishing moments. The higher the number of vanishing moments, the better the compression of the plant  $P$ . Recall, however, that the support width of the wavelet function and, consequently, the number of taps of the FIR filters  $h$  and  $g$  to implement the scale-recursive wavelet transform, is proportional to the number of vanishing moments. Thus, there is an inherent trade-off between achieving good compression and maintaining a computationally efficient transform.
- We choose a sparse interconnection “mask” in the wavelet domain that represents the interconnections we retain for the neutralization transfer function. This mask can be determined from the data and represents neutralization interconnections in the wavelet domain.
- We implement the neutralization transfer function using a multichannel FIR model. Each channel will be low-pass filtered and down-sampled in accordance with its bandwidth, while its impulse response length will also vary with channel in accordance with its degree of damping.

#### 4.6.2 Q-Parameter Design Feedforward Path

- We do a Q-parameter design of the controller, keeping in mind the implementation of our controller in terms of the transfer functions  $Q$  and  $P$  as described in the block diagram in Figure 4. We determine the optimal transfer function  $Q$  by solving the optimization problem in eqs.(5,7) either (1) in the wavelet domain, i.e., eq.(21), while constraining the wavelet-transformed operator  $\tilde{Q}$  to have limited interconnections; or (2) using a banded  $Q$  transfer function and solving eqs.(5,7) for the nonzero coefficients.
- We implement the feedforward transfer function using a multichannel FIR model. As in the case of the neutralization filter, each channel will be subsampled and have a filter length that is appropriate for that channel. In contrast to the neutralization path, however, for the feedforward path we can design our weights to have the multirate, variable filter

length structure by further constraining the structure of the Q-parameter when solving the optimization problem in eq.(21).



## 5 SENSOR/ACTUATOR PLACEMENT METHODS AND INTEGRATION WITH KIKO

### 5.1 Overview

The KIKO control design methodology described to this point assumes a starting point of uniformly spaced arrays of collocated sensors and actuators. Application of the wavelet transform treats the model of the system near the boundaries of the arrays by periodic repetition of the array.

In practice these aspects must be modified. Generally the arrangement of transducers is not uniquely dictated by the application, but must be determined as part of the design process. Uniform regularity of placement will generally be impossible due to design restrictions, such as the presence of other equipment, projections from surfaces, or variations in materials. Concern for cost could also be a major motivation for placing transducers more densely in some regions than in others. Even if one starts from an array designed to be uniform, yield from the manufacturing process and failure during operation will both result in irregular arrays. Manufacturing tolerances will also give arrays that have imperfections in collocation of sensors and actuators. Periodic repetition in computations with a finite array may lead to artifacts in the size of wavelet coefficients (due to apparent discontinuities from the periodization) and a reduction in attainable sparsity of the compressed representation. In the same vein, similar artifices would be necessary to treat boundaries that are not rectangular, with similar penalties. Finally, there may be additional benefits in compression from using multidimensional wavelets that are not just cross products of one dimensional wavelets.

We have addressed these issues with two general areas of investigation: optimal transducer selection, and wavelets for bounded and nonuniform arrays.

The optimal transducer selection work has resulted in a computational algorithm to treat an appropriate optimization problem. This approach assumes a predetermined grid of candidate transducer locations. The algorithm selects a predetermined number among these for use in control design. Thus, the result of transducer selection will be an irregularly spaced set even if the set of candidates is uniform spatially. Our algorithm is heuristic in order to avoid the computational complexity of an fully optimal solution. However, our results do provide bounds on suboptimality based on analysis of the problem data. Computational examples illustrate good performance of the algorithm.

In order to apply KIKO techniques to a transducer suite selected by optimization techniques, it is necessary to pursue the issues of what to do with non-uniformly located, possibly non-collocated, transducers in an irregularly bounded region. Our approach to applying wavelets to these cases followed three directions. First, we looked at direct use of nonuniform and non-collocated data by simply ignoring the imperfections and proceeding with computation. Next,

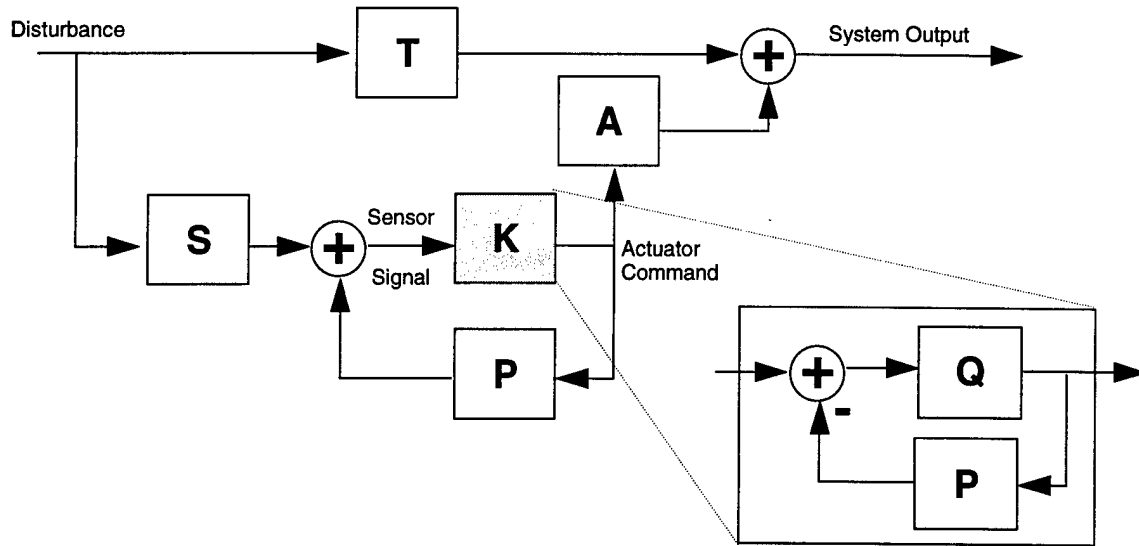


Figure 14: Standard feedback control block diagram with Q-parametrized controller.

we analyzed certain transformations of non-uniform data to synthesize a uniform array, and at the compression resulting from subsequent wavelet transformation. Finally, we investigated two types of generalized wavelets: wavelets tailored to the interval but using regularly spaced data, and so-called second generation wavelets, which can be tailored to arbitrary spacings and domain boundaries. We have computational results illustrating these various investigations.

## 5.2 Transducer Selection

This section summarizes work more completely described in [11]. The problem under consideration may be described with reference to Figure 14. Because of the properties of the Q-parametrization, as discussed in Section 3, for a given set of actuators and sensors the control design problem assumed here consists of choosing the transfer function  $Q$  to minimize quadratic cost criterion

$$\min_Q \sum_{\omega=\omega_l}^{\omega_h} \| T(\omega) - A(\omega)Q(\omega)S(\omega) \|_2^2 \quad (47)$$

subject to power constraints on the actuator commands expressed by

$$\sum_{\omega=\omega_l}^{\omega_h} \| Q(\omega)S(\omega) \|_2^2 \leq c \quad (48)$$

and the constraint that  $Q$  be causal and stable. The precise criteria used are not key to the developments here, as will be seen below. The  $\omega$ s in these expressions are frequencies at which we choose to evaluate the criteria, selected to cover a desired bandwidth with sufficient density to assure smooth behavior over that band.

In the present discussion we are concerned with selection of actuators and sensors, which amounts to determination of the transfer functions  $A(\omega)$  and  $S(\omega)$ . In the present approach we assume that some  $A_1(\omega)$  and  $S_1(\omega)$  are given, but that we wish to reduce the numbers of transducers by selecting only some of those represented in  $A_1(\omega)$  and  $S_1(\omega)$ . We represent this selection by using the **selector** matrices  $\Pi_a$  and  $\Pi_s$ , which contain all zeros except for a single one in each column of  $\Pi_a$  and each row of  $\Pi_s$ . Ideally, we would like to find these selector matrices to minimize the same cost as above, transforming the problem into

$$\min_{Q, \Pi_a, \Pi_s} \sum_{\omega=\omega_l}^{\omega_h} \|T(\omega) - A(\omega)\Pi_a Q(\omega)\Pi_s S(\omega)\|_2^2 \quad \text{subject to} \quad \sum_{\omega=\omega_l}^{\omega_h} \|Q(\omega)\Pi_s S(\omega)\|_2^2 \leq c \quad (49)$$

Exact solution of this problem requires solving  $\binom{m}{k} \times \binom{n}{l}$  control design problems, where  $m$  is the number of candidate sensors,  $n$  the number of candidate actuators,  $k$  the number of desired sensors, and  $l$  the number of desired actuators. If the desired number of transducers is flexible, the combinatorial complexity would be increased by summation of candidate values for  $k$  and  $l$ .

As discussed in [11], our approach is to substitute two heuristic calculation in order to avoid the intractability of the combinatorial solution. These are

$$\min_{\Pi_s} \max_{\omega} D(S^T(\omega), S^T(\omega)\Pi_s^T) \quad \text{and} \quad \min_{\Pi_a} \max_{\omega} D(A(\omega), A(\omega)\Pi_a) \quad (50)$$

Here  $D(X, Y) = \sin \Theta(\mathcal{R}(X), \mathcal{R}(Y))$  is the sine of the largest principal angle between the range spaces of  $X$  and  $Y$ , and is a useful measure of the distance between the ranges of the two linear maps  $X$  and  $Y$ .

Because  $A$  (and  $S$ ) may be near rank deficient, it is further desirable to maintain maximum numerical rank for the resulting  $A(\omega)\Pi_a$  matrix (respectively,  $\Pi_s S(\omega)$ ), and this can be done by using the subset selection algorithm based on the singular value decomposition as suggested in [10]. One benefit of the subset selection approach is that it provides upper bounds on the approximation error in using a particular transducer suite in terms of the largest residual singular value. This provides a means for selecting a “good” number of transducers when there is a gap in singular values of the  $A$  (or  $S$ ) matrices. See [11] for details.

For the case of 40 candidate transducer locations, with 20 to be kept, and 300 frequencies to be used for evaluation, Table 1 indicates the relative complexity of the present algorithm (“multidimensional QR”) compared to the optimal (“exhaustive search”) and other heuristic approaches. Multidimensional QR is guaranteed to have superior performance the other heuristic techniques, and is roughly comparable in the complexity of computation.

This algorithm was used in the DARPA SPICES program for transducer selection. [11] has some examples of the SPICES computations, and also more details about the computational complexity.

Method	Complexity
Exhaustive Search	6.9e19
Sequential Forward Selection	3.8e9
Multidimensional QR	9.9e7
Best $k$	1.7e6

Table 1: Example Complexity Comparison

### 5.3 Direct Use of Imperfect Data

As a first step in considering alternatives to compensate for nonuniform or noncollocated transducers, we computed wavelet transforms of simulated data for an Euler-Bernoulli beam model containing the irregularities. Typical results are shown in Figures 16 and 17. For these plots, wavelet transforms were computed as if the data were all regularly spaced, when in fact the data contains responses due to perturbed transducers.

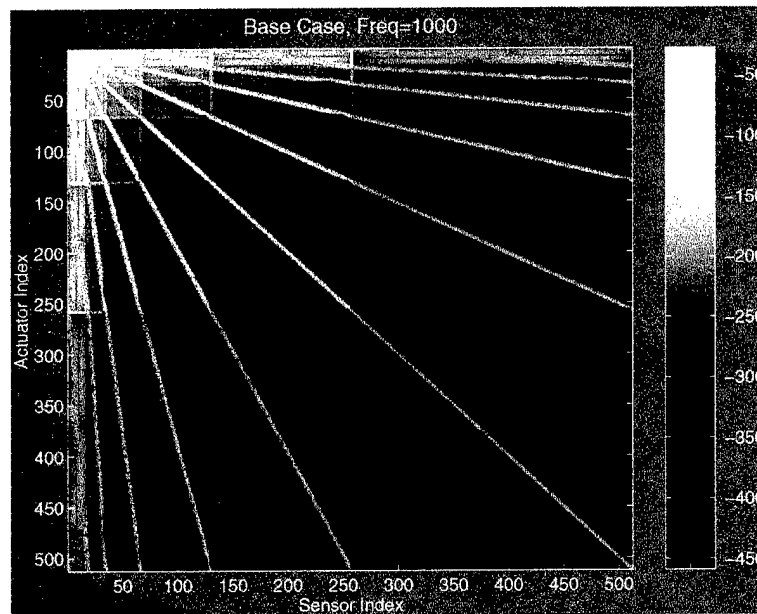


Figure 15: 8-tap wavelet transform for beam at 1 kHz with regularly spaced, collocated transducers.

In Figure 16 we see the results of perturbing the location of a single transducer pair by one half the regular transducer spacing. Note that one new vertical and one new horizontal line appear at each scale in the transformed data. This indicates that the transfer functions from the displaced actuator to all the sensors have acquired an apparent discontinuity in a derivative, as have the transfer functions from all the actuators to the displaced sensor. This is as one would expect: smoothness at a point would generally be disrupted by an arbitrary jump in a function value at that point.

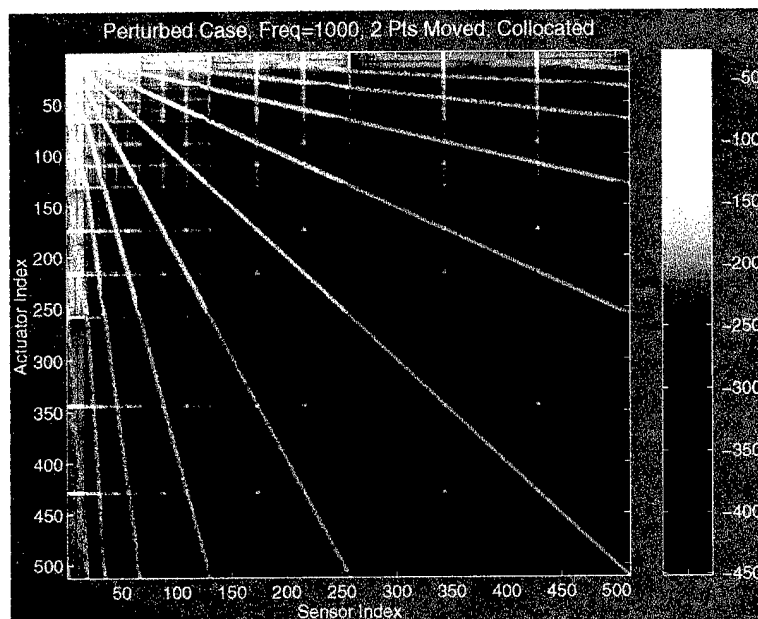


Figure 16: 8-tap wavelet transform for beam at 1 kHz with two transducer pairs displaced from evenly spaced position by 0.5 the regular spacing.

In Figure 17 we see a similar result for the case of perturbing a sensor location but not perturbing the location of the corresponding actuator. Here we see the apparent discontinuity in the transfer functions from all actuators to the perturbed sensor, and of course all other transfer functions remain unaffected.

If the true positions of transducers are known, then we can attempt to compensate for the assumption of uniformly spaced data in the wavelet transform. We examine two approaches. In the next section, we look at interpolation of irregularly spaced data to the uniformly spaced case. In the following section we discuss the use of wavelets tailored to nonuniform data. In both cases the true positions of the transducers must be known, either by design or experimental calibration.

## 5.4 Transformation of Nonuniform Data for Wavelet Calculations

This section describes our initial approach to the problem of applying KIKO control technology to a set of nonuniformly spaced transducers. The KIKO method of representing MIMO transfer functions via lossy compression has been shown to yield adequately faithful plant models with limited interconnections. By "limited interconnections" we mean that not every output depends on every input at all scales. Further, because of the apparent properties of the wavelet transform, for certain classes of plants the limitation of interconnections is regular and predictable, suggesting a conceptually simple, repeatable control architecture.

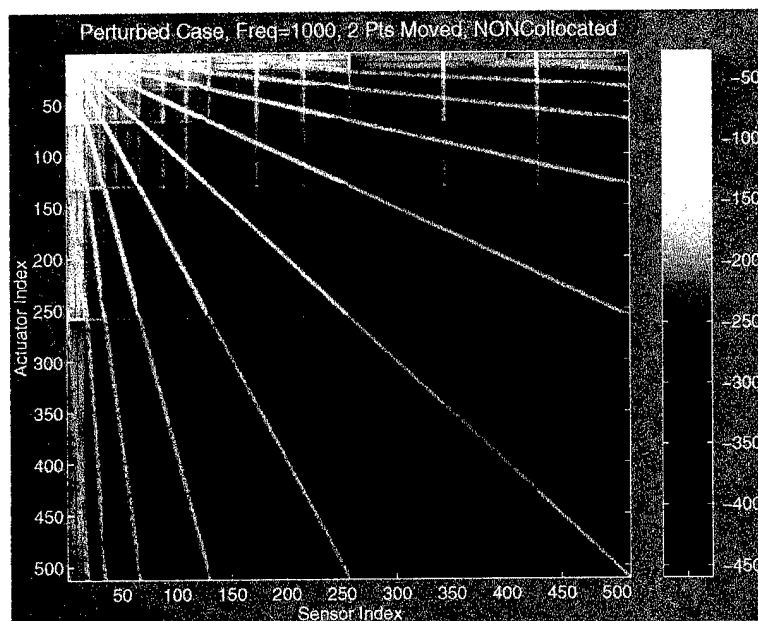


Figure 17: 8-tap wavelet transform for beam at 1 kHz with two sensors displaced from positions collocated with actuators by 0.5 the regular spacing.

#### 5.4.1 Problem Statement

The wavelet-based compression strategy that KIKO employs takes advantage of geometric properties of the Green's function describing the plant to be modeled. It uses particularly apt, fast, frequency-independent rotations, so that the transformed matrix transfer function is "sparse." For regularly spaced sensor-actuator pairs this geometric dependence produces the familiar finger plots that show important connections between input and output at a particular frequency (Section 4). In this part we will build upon these results, borrowing heavily from the notation and hooking into the machinery for computing the wavelet coefficient bound.

Now consider the case where a sensor-actuator pair is displaced from its regularly spaced position. One may now ask what happens to compression and the finger plot? It is easy to see that the compression level is different, and that the finger plot changes qualitatively. What is less clear is whether compression increases or decreases, and by how much. The goal of this note is to explore how we can quantify this difference.

The above paragraph outlines the analysis problem; we have not yet attacked the synthesis counterpart. The main synthesis problem to be addressed is the determination of sensor-actuator locations so that compression is maximized, where the metric of compression is ill-defined but presumably includes some frequency band. At a single frequency, we have some preliminary results based on an extension of the technique presented here.

A second caveat is less severe but still worth noting. Analysis of nonuniform compression, as attempted here, is different from reconstruction of a signal from nonuniform samples.

Wavelet-based compression looks to decompose a matrix of transfer functions, obtained via discrete sampling of an underlying continuous functional. At no point do we reconstruct the functional from samples.

Although there is a broad body of literature concerning the reconstruction of functions in various spaces from their regular or irregular samples, that work is not necessarily applicable to our control problem. As we have seen in various examples, the ability to do vibration control, for instance, depends not on the faithful reconstruction of arbitrary functions (as limited to be in some space) from their samples, but merely with the correlation of samples with performance measures. Thus, we obtain the rule-of-thumb in acoustics problems that the number of actuators must equal or exceed the rank of the disturbance-to-performance transfer matrix, regardless of the spatial complexity of the underlying functional.

All the results discussed here refer to single-dimension problems, such as a beam rather than a plate. Extensions to higher dimensions are conceptually easy but hindered by the availability of spline or other interpolating functions in two or more dimensions.

The final caveat we will mention concerns the collocation of the sensors and actuator. The notion of sensor-actuator pairs has been mentioned, and implies that there is exactly one sensor for each actuator. Here we state that as an assumption, along with the additional assumption that sensors and actuators are collocated. The second assumption is employed for notational ease and is readily removed. In fact, the irregularity of sensors may be different than that of actuators. The first assumption cannot be relaxed without causing some unnaturalness in the wavelet transform, since the input and output rotations would be dissimilar. Therefore, this assumption cannot be relaxed without a generalization of the KIKO methodology.

#### 5.4.2 Outline of Approach

The work presented here develops simple machinery to enable the application of results, obtained earlier for uniform spacing, to the nonuniform-spacing case. Before presenting the development, we give a brief outline of the simple underlying idea.

Wavelet analysis is properly defined for functions,  $f$ , defined on some compact, connected subset of the real line,  $S \subset \mathbb{R}$ . The wavelet coefficients are obtained by computing inner products of wavelet basis functions with  $f$ . Wavelet transforms are defined for discretely sampled functions,  $f_k$ , by equating the samples with the output of the continuous wavelet transform of  $f$  at the finest scale. Subsequent scale coefficients are computed using the discrete wavelet transform.

Thus there is an assumption of sampling uniformity in the discrete wavelet transform, since the wavelets used to produce  $f_k$  are uniformly-spaced translates of one another. This assumption of uniformity leads directly to the KIKO result of sparse wavelet-based representation for certain classes of Green's functions.

The finite-interval discrete wavelet transform can be viewed as a linear transformation from  $\mathbb{R}^K$  to  $\mathbb{R}^K$ . If the sampling is nonuniform, this linear transformation is still well defined, even if sparse representations should no longer be expected. What level of compression will be obtained? To address that question, we return to the definition of the discrete wavelet transform.

The main idea is this: although the samples,  $f_k$ , are nonuniform, and thus are not properly interpreted as generated by the continuous wavelet transform of some  $f$ , we will define a new function,  $\hat{f}$ , for which the uniform samples obtained by computing the continuous wavelet transform at the finest scale are exactly the  $f_k$ . Additionally, this function will be constrained to belong to the same important spaces as  $f$  (this is basically a matter of ensuring sufficient differentiability). We are now done: the new function,  $\hat{f}$ , will be analyzed using existing machinery to determine the compression level obtained.

That is, we see  $\hat{G}$  as the Green's function for an imaginary material whose regular samples by design equal the irregular samples of  $G$ . Because the relationship between  $G$  and  $\hat{G}$  is known, the functional form of  $\hat{G}$  is also available, and we use that to compute bounds on the compression of  $\hat{G}$ . Finally, since the wavelet transforms for  $\hat{G}$  and for  $G$  are identical, we obtain bounds for the compression for  $G$  with irregular samples  $G_k$ .

### 5.4.3 Notation

Let  $X$  be a compact, connected subset of the real line which supports a Green's function of interest. Let  $r, s \in X$ , and denote the Green's function as  $G(r, s)$ . The letter  $r$  stands for receiver, and  $s$  stands for source. We assume we know a functional representation for  $G$ , so that we may compute derivatives.

Let the location of sensor-actuator pairs be given by the points  $x_k$ . They are not uniformly spaced, but are, without loss of generality, ordered so that  $x_{k-1} < x_k$ . Let us also assume that there are a finite number of transducer locations,  $1 \leq k \leq K$ , and the region of support for  $G$  is a finite interval  $X = [A, B]$ . For simplicity we include the endpoints, though this may be inappropriate for certain boundary conditions. The extension to (semi) infinite and/or (half) open regions of support is straightforward.

Define a second compact, connected set,  $\hat{X}$ , which for the finite case above is the interval  $[\frac{1}{2}, K + \frac{1}{2}]$ . This is the set on which we will construct the imaginary Green's function,  $\hat{G}$ . Thus we define  $\hat{r}, \hat{s} \in \hat{X}$ , and denote the Green's function as  $\hat{G}(\hat{r}, \hat{s})$ . The transducer locations are just the first  $K$  integers:  $\hat{x}_k = k$ .



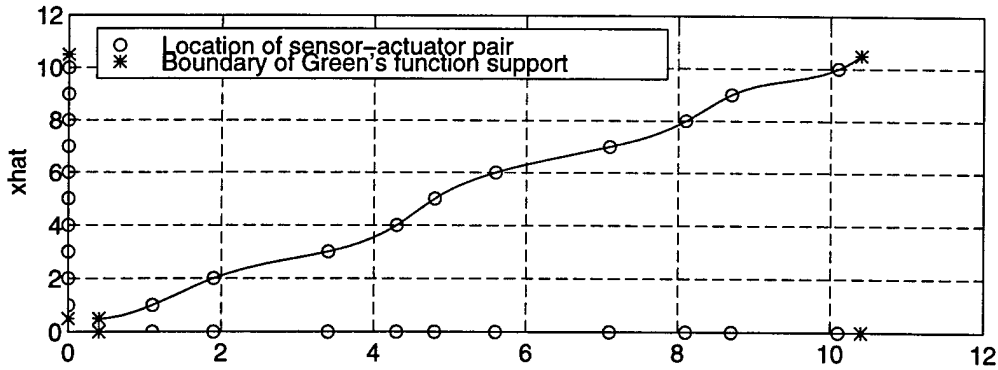


Figure 18: Illustration of example warping function in one dimension,  $g$ , mapping the irregularly sampled space,  $X$ , to the regularly sampled space,  $\hat{X}$ .

#### 5.4.4 The Warping Function

To define the transform of  $G$  to a space of evenly spaced sampling points, we imagine a one-to-one and onto **warping function**,  $g : X \rightarrow \hat{X}$ . (This development grew out of reconstruction theory for nonuniform sampling theory [4, 5], and its application to nonuniform sampling for wavelets is believed novel.) Since  $X$  and  $\hat{X}$  are intervals, we have immediately that  $g(A) = \frac{1}{2}$  and  $g(B) = K + \frac{1}{2}$ . We also impose the constraints  $g(x_k) = k$ , which implements our requirement that the transducer locations in the imaginary set are evenly spaced. An example of such a function is shown in Figure 18.

Since the function  $g$  is invertible, we write  $\gamma \triangleq g^{-1} : \hat{X} \rightarrow X$ . So far,  $\gamma$  is not well defined. That is, there are an infinity of possible  $\gamma$ 's which meet the criteria we have imposed. Let us agree to retain the remaining degrees of freedom for the time being, and investigate the properties of  $\gamma$  that can be deduced at this point.

#### 5.4.5 Building a Useful Imaginary Green's Function

Let us define the warped Green's function on  $\hat{X}$  as

$$\hat{G}(\hat{r}, \hat{s}) \triangleq G(\gamma(\hat{r}), \gamma(\hat{s})) \quad (51)$$

Note that, once  $\gamma$  is specified,  $\hat{G}$  is well defined. Thus an imaginary material with a Green's function has been constructed, with imaginary uniformly spaced samples. It is now appropriate to employ the analysis of the Green's function and its spatial derivatives to bound the level of compression, because the assumption of sample uniformity has been met, enabling a discretely sampled function,  $\hat{f}_k$ , to be equated with the output of the continuous wavelet transform of some  $\hat{f}$  at the finest scale.

In [3], a bound for the wavelet coefficient,  $\alpha_{m,n,\bar{m},\bar{n}}$ , is sought. (Here  $m$  is the scale index and  $n$  is the translation index for the “receive” wavelet, and  $\bar{m}$  is the scale index while  $\bar{n}$  is the translation index for the “source” wavelet. See that paper for details.) To compute this bound, the anchor points  $\hat{r}_0 = 2^{-m}n$  and  $\hat{s}_0 = s^{-\bar{m}}\bar{n}$  were used, representing the edges of the receive and source wavelet supports,  $\Omega_{\hat{r}}$  and  $\Omega_{\hat{s}}$ , respectively. In general, they may represent wavelets at different scales, and may or may not intersect. Additionally,  $\hat{r}$  and  $\hat{s}$  are test points inside  $\Omega_{\hat{r}}$  and  $\Omega_{\hat{s}}$ ; these points will be varied as the Green’s function is integrated against the wavelet basis functions to form the bound. In summary,

$$\begin{aligned}\Omega_{\hat{r}} &= [2^{-m}n, 2^{-m}(n+1)] \\ &= [\hat{r}_0, \hat{r}_0 + 2^{-m}]\end{aligned}\tag{52}$$

$$\begin{aligned}\Omega_{\hat{s}} &= [2^{-\bar{m}}\bar{n}, 2^{-\bar{m}}(\bar{n}+1)] \\ &= [\hat{s}_0, \hat{s}_0 + 2^{-\bar{m}}]\end{aligned}\tag{53}$$

$$\begin{aligned}\hat{r} &\in \Omega_{\hat{r}} \\ \hat{s} &\in \Omega_{\hat{s}}\end{aligned}$$

The essential component to the bound on compression is a term,

$$B_i^2(\hat{r}, \hat{s}) = \sup_{t \in [0,1]} \left( \frac{\partial^{2M}}{\partial \hat{r}^i \partial \hat{s}^{2M-i}} \hat{G}(\hat{r}_0 + t(\hat{r} - \hat{r}_0), \hat{s}_0 + t(\hat{s} - \hat{s}_0)) \right)^2 \tag{54}$$

Here  $M$  is the number of vanishing moments possessed by the wavelet basis functions, and  $i$  varies from 0 to  $2M$ . This expression is correct when  $\Omega_{\hat{r}} \cap \Omega_{\hat{s}}$  is empty; a slightly different expression is required when the intersection is nonempty:

$$\bar{B}_i^2(\hat{r}, \hat{s}) = \sup_{t \in [0,1]} \left( \frac{\partial^T}{\partial \hat{r}^i \partial \hat{s}^{T-i}} \hat{G}(\hat{r}_0 + t(\hat{r} - \hat{r}_0), \hat{s}_0 + t(\hat{s} - \hat{s}_0)) \right)^2 \quad \hat{r} \neq \hat{s} \tag{55}$$

Recall that the class of Green’s functions presented in [3] are discontinuous in their  $T^{th}$  derivative at  $\hat{r} = \hat{s}$ . The central difference in the two cases is that when  $\hat{r} = \hat{s}$ , as can only happen in the intersecting case, the wavelet transform will uncover the discontinuity in the  $T^{th}$ -order partial derivative of  $\hat{G}$ , if  $2M > T - 1$ .

Computation of  $B_i^2(\hat{r}, \hat{s})$  in (54) is straightforward once  $\gamma$  is chosen. For notational convenience, define the following identical functions to serve as placeholders:  $\rho(\cdot) \triangleq \gamma(\cdot)$  when the argument is  $\hat{r}$ ;  $\sigma(\cdot) \triangleq \gamma(\cdot)$  when the argument is  $\hat{s}$ . Also define  $\tau(\hat{x}; \hat{x}_0) \triangleq \hat{x}_0 + t(\hat{x} - \hat{x}_0)$ . Then the form of the arguments of  $\hat{G}$  in (54) becomes

$$\begin{aligned}\hat{G}(\hat{r}_0 + t(\hat{r} - \hat{r}_0), \hat{s}_0 + t(\hat{s} - \hat{s}_0)) &= G(\rho(\hat{r}_0 + t(\hat{r} - \hat{r}_0)), \sigma(\hat{s}_0 + t(\hat{s} - \hat{s}_0))) \\ &= G(\rho(\tau(\hat{r}; \hat{r}_0)), \sigma(\tau(\hat{s}; \hat{s}_0)))\end{aligned}$$

Partial derivatives of this term may be computed directly using the chain rule. For example,

$$\frac{\partial}{\partial \hat{s}} G(\rho(\tau(\hat{r}; \hat{r}_0)), \sigma(\tau(\hat{s}; \hat{s}_0))) = t\sigma' G_\sigma(\rho, \sigma)$$

$$\begin{aligned}
\frac{\partial^2}{\partial \hat{s}^2} G(\rho(\tau(\hat{r}; \hat{r}_0)), \sigma(\tau(\hat{s}; \hat{s}_0))) &= t^2 \sigma'' G_\sigma(\rho, \sigma) + t^2 (\sigma')^2 G_{\sigma\sigma}(\rho, \sigma) \\
\frac{\partial^3}{\partial \hat{s}^3} G(\rho(\tau(\hat{r}; \hat{r}_0)), \sigma(\tau(\hat{s}; \hat{s}_0))) &= t^3 \sigma''' G_\sigma(\rho, \sigma) + 3t^3 \sigma' \sigma'' G_{\sigma\sigma}(\rho, \sigma) + t^3 (\sigma')^3 G_{\sigma\sigma\sigma}(\rho, \sigma) \\
\frac{\partial^2}{\partial \hat{r} \partial \hat{s}} G(\rho(\tau(\hat{r}; \hat{r}_0)), \sigma(\tau(\hat{s}; \hat{s}_0))) &= t^2 \rho' \sigma' G_{\rho\sigma}(\rho, \sigma)
\end{aligned}$$

where the arguments  $\tau(\hat{r}; \hat{r}_0)$  and  $\tau(\hat{s}; \hat{s}_0)$  have been suppressed. Subsequent derivatives may be computed directly by repeated use of the chain rule and the product rule. The remainder of the wavelet coefficient bound computation is identical to that given in the corrected version of [3].

#### 5.4.6 Bounds Comparison

The comparison of bounds is unfortunately complicated by the lack of intuition about what factors contribute significantly. For instance, the term  $B_i(\hat{r}, \hat{s})$  must be evaluated, either inside the integral in (43) of [3], or separately to compute a supremum over  $(\hat{r}, \hat{s}) \in \Omega_{\hat{r}} \times \Omega_{\hat{s}}$  which can then be brought outside the integral. The same applies for  $\bar{B}_i(\hat{r}, \hat{s})$  in (55) of [3]. We have a poor understanding of the relative magnitudes of these two terms.

In particular, there is an assumption that  $B_i$  is not so much larger than  $\bar{B}_i$  that it contributes to the bounds on size of the wavelet coefficients for nonintersecting and intersecting cases. If this assumption were violated, it could increase the number of vanishing moments,  $M$ , required to get good compression. The current mathematical machinery does not address this question.

Nevertheless, the example computations above show that the computation of the  $B_i$ 's or  $\bar{B}_i$ 's is **changed** by nonuniform spacing only through the introduction of derivatives of this warping function. The warping function really adds nothing that essentially complicates computation of the bound. Recall that there were an infinity of warping functions that interpolate the transducer locations in Figure 18. Good choices for  $\gamma$ , which don't change either  $B_i$  or  $\bar{B}_i$  much, would then have first derivatives close to unity and all other derivatives small or zero throughout the domain of  $\gamma$ . Intuitively, one may think that these derivatives never get larger than they have to, while still growing the function to meet the boundary conditions, so that various products of them with  $G$  and its derivatives remain small.

#### 5.4.7 Issues

Note that the expression (54) becomes unwieldy if  $\gamma$  has nonvanishing high-order derivatives, because repeated use of the product rule is required. Each use of the product rule produces more terms that do not group together in a compact structure such as a binomial expansion. However, if  $\gamma$  is an affine function, so that  $\rho$  and  $\sigma$  are both affine, then the computation of  $B_i$  and  $\bar{B}_i$  are greatly simplified.

The choice of warping function plays a key role in our analysis, but its effect on the compression bounds is distressingly hidden, and its effect on the true compression is of course nonexistent. Thus the act of warping function choice becomes one of preserving the tightness of the bounds, if indeed that is possible.

The warping function can be considered to interpolate among the  $(x_k, \hat{x}_k = k)$  pairs. The plot in Figure 18 used cubic spline interpolation as an example. One could also consider the use of linear interpolation, which offers the attractive quality of vastly simplifying the computation of the bounds for almost all values of  $t$ . However, a linear interpolation introduces discontinuities in the first derivative at the knot points. It is not clear how to handle these within the supremum framework we have developed; they clearly cannot be ignored, since a smooth approximation to such a discontinuity would contribute large factors corresponding to higher derivatives. On the other hand, they are not real, and so should not be expected to hurt compression the way discontinuities in the Green's function do.

One view, requiring further exploration, is that the use of linear interpolation may lead to a good **approximation** of the strict bound. This approximation may prove useful since it would approximately quantify the loss of compression as a function of transducer spacing. The formula for computing the bound, which is undefined at the knots, will need to be repaired.

## 5.5 Generalized Wavelets

The basic theory of wavelets applies to functions in  $L^2(\mathbb{R})$ , that is, square-integrable functions defined on the real line. It is straightforward to extend this theory to the higher dimensional spaces  $L^2(\mathbb{R}^n)$  by simply taking as the wavelet basis the direct product of wavelets for  $L^2(\mathbb{R})$ . However, realistic domains for posing control problems will be bounded in  $\mathbb{R}^n$ , and generalization in a satisfactory way to other  $L^2$  spaces, starting with  $L^2([0, 1])$ , is not so obvious.

Two issues arise immediately in considering the application of wavelet representations to real control problems: First, that we need to compute wavelet transforms for functions on bounded domains, and second, that the spatial distribution of the data we wish to transform will generally not be uniform or regularly spaced. The first issue is a problem for standard wavelet analysis because any smooth wavelet basis for  $L^2(\mathbb{R})$  has elements that straddle the boundary points 0 and 1, and calculation of the corresponding coefficients in the wavelet expansion requires knowledge of function values outside the interval of definition.

Considering procedures used to handle Fourier transforms on finite intervals, there are two obvious approaches to try: extending the function by padding with zeros, and extending the function by periodic repetition. Following [6], we note several difficulties with these approaches. Both the zero padding and periodic extension techniques typically generate discontinuities at the boundary, resulting in large wavelet coefficients for fine scales even when the function is otherwise smooth on  $[0, 1]$ . Furthermore, the zero padding approach uses more wavelets than necessary, since some wavelets extend outside the interval in their support.

[6] also mentions the use in image analysis of extension beyond the boundaries by reflection, which obviously results in continuity at the boundary points. However, the derivatives at the boundaries will generally be discontinuous even when the function is smooth, again resulting in (possibly unnecessarily) large wavelet coefficients. A fourth alternative mentioned in [6] is a wavelet basis for the interval developed by [13], which does not give boundary artifacts as do the others. However, the authors of [6] object to the inability to generalize these wavelets to wavelet packets, and numerical ill-conditioning involved in constructing the “edge” wavelets with support at the boundary.

[6] introduces a new wavelet construction that does not suffer from the above difficulties, and we performed some experiments with these wavelets for our beam and plate models. ([6] cites a similar construction developed independently by B. Jawerth, and discussed in [1].) Other (less useful) constructions are due to various other authors. However, all these have in common that for application to sampled data via discrete version of the transforms, uniformly spaced data are required.

More recently, W. Sweldens [15] developed a new approach to the construction of wavelets that applies not only to functions on intervals, but to general domains in multiple dimensions with unevenly spaced data, which he called [16] “second generation” wavelets. We also experimented with these wavelets using our beam and plate models.

Below, we report on these two sets of experiments, and discuss our perceptions of their comparison, advantages and shortcomings. We wish to emphasize that these results are largely superficial and preliminary, and we feel that there is much benefit to be derived from further investigation in this area.

### **5.5.1 Comparisons of Reconstruction Error and Sparsity**

In numerical experiments using the wavelets constructed in [6], which we call “boundary wavelets,” it is easy to demonstrate significant advantages in compression over applying standard wavelet analysis through periodic repetition of a function on an interval. However, this advantage relies on the presence of discontinuities at the (former) boundary points in the repeated function. The frequency domain beam model used in our numerical experiments had clamped boundary conditions, and therefore the periodized transfer function is spatially continuous at the (former) boundary points up to the first derivative. This results in no advantage for the boundary wavelets over standard wavelets, as can be seen in Table 2. The data in Table 2 is based on setting to zero all wavelet coefficients below a certain threshold fraction of the norm of the wavelet transform, listed as the “truncation level.” The “reconstruction error” listed is the fraction of the norm of the original transfer function data.

Table 2 also indicates, at least for this example, that the lifted wavelets can provide a factor of 2 more sparsity for a given level of reconstruction error. It is difficult to make direct comparisons, because of the number of variables involved. For a given wavelet order, the lifted

Wavelet Order	Truncation Level	Standard Wavelets		Boundary Wavelets		Lifted Wavelets	
		Density	Reconstruction Error	Density	Reconstruction Error	Density	Reconstruction Error
4	-50 dB	24.7%	-39.2 dB	24.7%	-39.0 dB	15.2%	-50.8 dB
4	-40 dB	9.9%	-29.7 dB	9.6%	-31.1 dB	5.0%	-38.0 dB
6	-50 dB	11.1%	-37.9 dB	10.8%	-36.2 dB	6.7%	-44.0 dB
6	-40 dB	4.5%	-30.0 dB	4.4%	-30.5 dB	2.9%	-30.4 dB

Table 2: Compression results based on 128 transducer pairs and 4 levels of wavelets computed.

wavelet algorithm can require better than a factor of 2 less computation. (Since lifted wavelets are not orthonormal, there are two order numbers to specify – the number of vanishing moments and the number dual vanishing moments. For comparison's sake here we have chosen wavelets with these two numbers equal. In practice, however, this afford an additional degree of freedom in performing the tradeoff between sparsity and reconstruction error.) Different wavelets may be chosen for all three cases, and performance may depend on those choices. It is not clear from this example whether the better performance for the lifted wavelets is due to the treatment of edge effects or the difference in the interior wavelets. Ultimately, the best basis of comparison would be the amount of computation required to achieve desired levels of sparsity and reconstruction error. We have not gone to the required level of detail for that analysis.

## 5.6 Conclusions and Recommendations for Further Work

The transducer selection algorithm we have described above and in the appended paper [11] seeks to pick transducers that give the best numerical range in sensing and actuation for fixed number of transducers. Such a criterion makes sense from the standpoint of minimizing gains to enhance robustness, and limiting the sensitivity of performance to noise or random errors in measurement. The algorithm will result in nonuniform transducer locations, and of course real transducer arrays will always be spatially bounded. We discussed two means of treating the nonuniformities, interpolation and second generation wavelets, and two means of treating boundedness, boundary wavelets and second generation wavelets. It is clear that second generation wavelets merit further investigation.

The definition of second generation wavelets will depend on the transducer locations, so development of the algorithms for performing transforms and the architecture for information flow must take into account the sequence and assumptions behind such data. For example, it is likely that quite accurate transducer locations will be known prior to fabrication, allowing algorithm structure and data network architecture to be determined prior to fabrication, but that it may be necessary to perform calibration on the as-built system to determine the variety of coefficients needed to complete implementation. Of course, depending on variability, it may be possible to calibration once for an entire production line.

There is another possible use of transducer selection or placement which we have not investigated, that of selecting transducers to optimize compression. This makes sense only when there are a large number of transducers, and where much of the data is redundant in an appropriate sense. (Otherwise, transducer location is essentially dictated by what one needs to know and to affect, and algorithm presented above is very relevant.)

This reasoning might seem to lead to dispensing with large numbers of transducers and simply using the minimally few devices needed as determined via our selection algorithm: this is another form of compression – done by installing only those transducers a model says are needed. However, there is a big difference between compression based on just placing devices where a model says, and compression using the real smoothness properties of many physical measurements: the former is much more susceptible to the effects of uncertainty and much less adaptable to changes in the system. The availability of proliferated sensing and actuation opens up an opportunity for substituting real time measurements for models that are dubious (as in the case of complex physical systems).

From this perspective, it seems that it should be important to investigate **patterns** of transducer arrays, in particular how to position devices around boundaries and physical discontinuities, and **densities** of transducer arrays needed to measure and affect desired physical properties. These are areas for continuing work.

## 6 NUMERICAL RESULTS AND SIMULATIONS FROM MODEL DATA

In this section we report our results on applying the KIKO control method to simulated data using two different numerical models: (1) a model based on solutions to an Euler-Bernoulli beam and (2) a model based on modal representation of a flexible plate.

### 6.1 Euler-Bernoulli Beam Results

We used an Euler-Bernoulli beam model to test our transfer compression method and to test our overall control method using simulated data. For our example, we use an Euler-Bernoulli beam, whose equation of motion is given by

$$w_{rrrr} + \omega^2 w = -p(r) \quad r \in [0, 1]$$

where  $w$  is the dimensionless vertical displacement of the beam,  $\omega$  is dimensionless frequency and  $p$  represents the forcing along the beam. We use clamped boundary conditions

$$w = w_r = 0 \text{ for } r = 0, 1.$$

The Green's function in this case satisfies

$$G(r, s)_{rrrr} + \omega^2 G(r, s) = -\delta(r - s),$$

along with the boundary conditions above. Solution for the Green's function is possible in closed form. An analytical derivation for the Green's function of a finite-length Euler Bernoulli beam is given in Appendix A. Figure 19 shows the magnitude of the Green's function at a dimensionless frequency,  $\omega = 215$ , where 512 equally spaced samples along the beam were used as collocated forcing and sensing points.

The result of applying an orthonormal wavelet transform to the Green's function depicted in Figure 19 is shown in Figure 20. Note that the coefficient energy is highly concentrated along "finger-like" patterns in the matrix. This provides immediate visual validation for our analytical predictions of transfer function compression by showing that in the wavelet representation the transfer function coefficients are concentrated into a sparse pattern.

In Figure 21, we show the result of thresholding the wavelet coefficients shown in Figure 20 so that only coefficients greater than  $1e-8$  times the norm of the matrix appear in black. Note that the resulting coefficient pattern is indeed extremely sparse and that these coefficients can be used to *approximate* the original Green's function operator with a relative error of only  $1e-8$ . To compare what our analytical results in [3] suggested as important coefficients for approximation of the Green's function operator, Figure 22 shows the predicted finger-like pattern where overlaps in wavelet function supports occur.



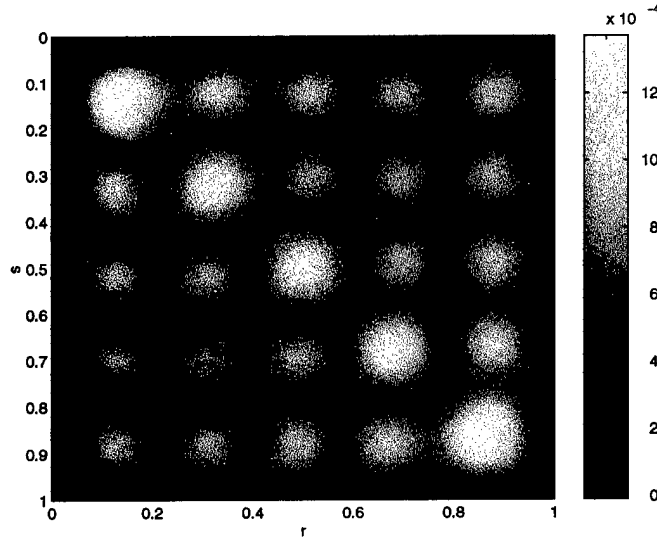


Figure 19: A plot of the magnitude of the Green's function for our Euler-Bernoulli beam with clamped ends as a function of the field point,  $r$  and the source point,  $s$ , and dimensionless frequency,  $\omega = 215$ . The scale is given by the colorbar on the right.

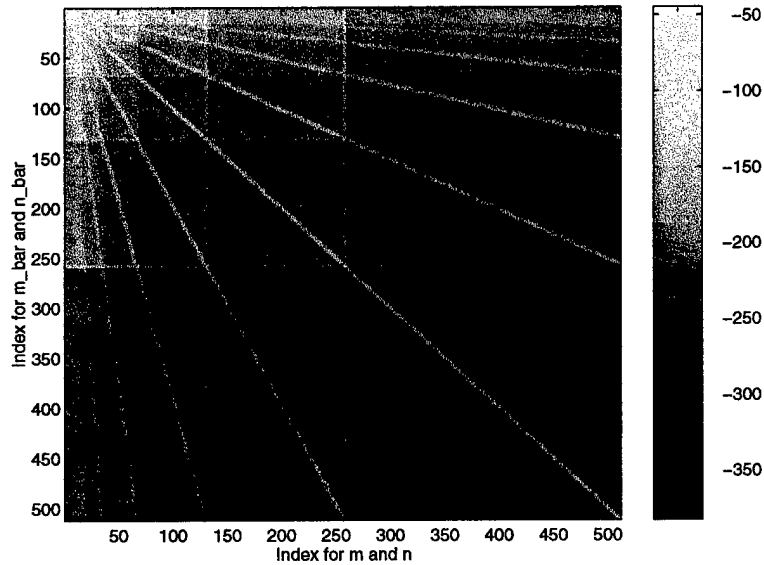


Figure 20: Magnitude of wavelet transform of Euler-Bernoulli beam Green's function using Daubechies 8-tap filter, plotted on dB intensity scale

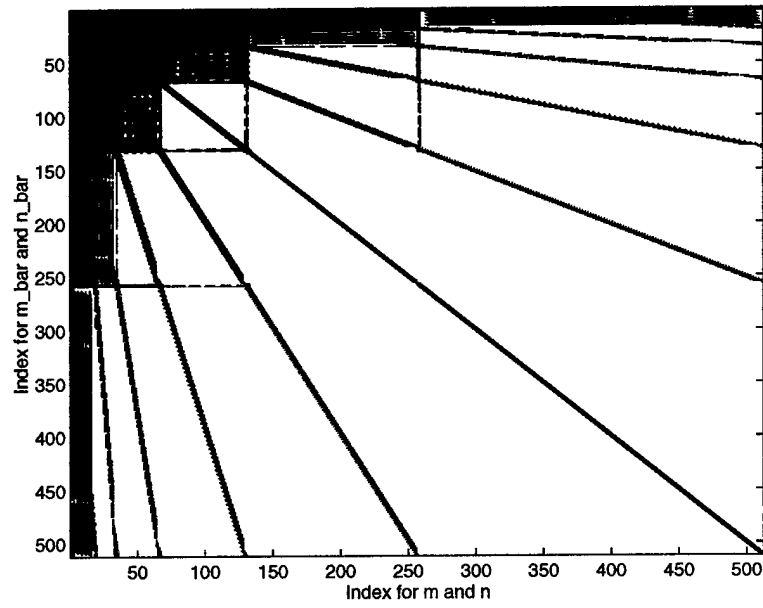


Figure 21: Thresholded wavelet coefficients shown in black.

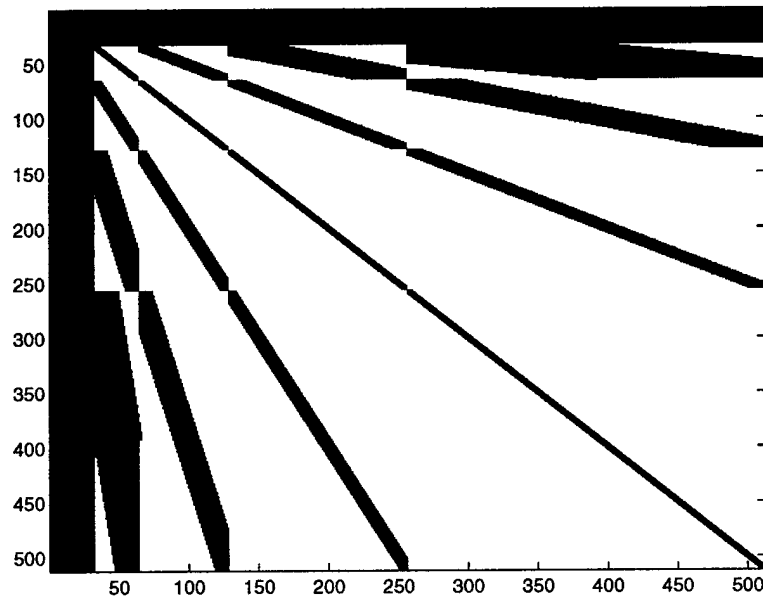


Figure 22: Predicted "finger-like" pattern for wavelet transformed Green's function operator.

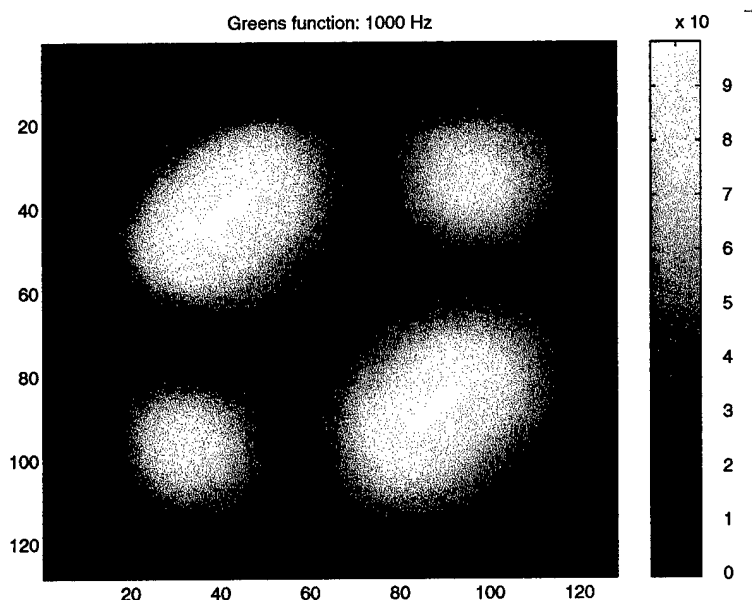


Figure 23: Intensity image of magnitude of Green's function at 1000 Hz

Further numerical experiments showed that the compression property holds for a wide range of frequencies. As an example, consider the case in Figure 23, which shows the magnitude of the Green's function at a much lower frequency than the previous case. Also, the number of samples is now 128 points rather than 512.

Figure 24 is a plot of the magnitude of the wavelet transform of the Green's function. Again, the finger-like pattern appears. In Figure 25, we show the coefficients of the wavelet-transformed Green's function greater than  $1e - 5$  times the norm of the Green's function.

We now show results of controlling the response of the Euler-Bernoulli beam in the presence of external disturbances. These results show that wavelet transfer function compression combined with sparse Q-parameter design can be successfully applied to the control of a beam using a dense array of actuators and sensors. The beam is taken to be steel of length 1 m, thickness 2 cm and width 5 cm. The internal damping  $\eta = .2$ , while the Young's modulus is equal to  $1.96e11 \text{ kg/ms}^2$ .

We design an optimal banded Q-parameter using an FIR parameterization for Q and solving eqs.(5,7) for the non-zero coefficients. Figure 26 shows the performance results for two different disturbances: (1) an impulsive force excitation at a point on the beam and (2) a random distribution of force excitations along the beam. We used 32 equally sampled points along the beam as collocated sensor and actuator positions. Full neutralization was used, i.e., no wavelet compression was applied to the plant transfer function. This case was performed to give us baseline performance for comparison purposes. The RMS performance was 19.7 dB over a 0 to 10 kHz bandwidth. Note that the bottom two plots bearing a resemblance to lips show the maximum output response for the controlled (white) and uncontrolled (red) cases along the

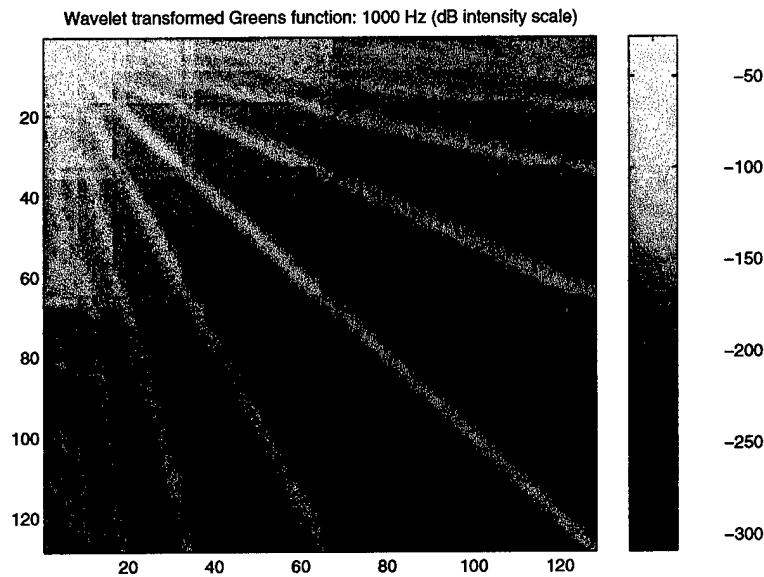


Figure 24: Intensity image of magnitude of wavelet-transformed Green's function at 1000 Hz (intensity plotted in dB)

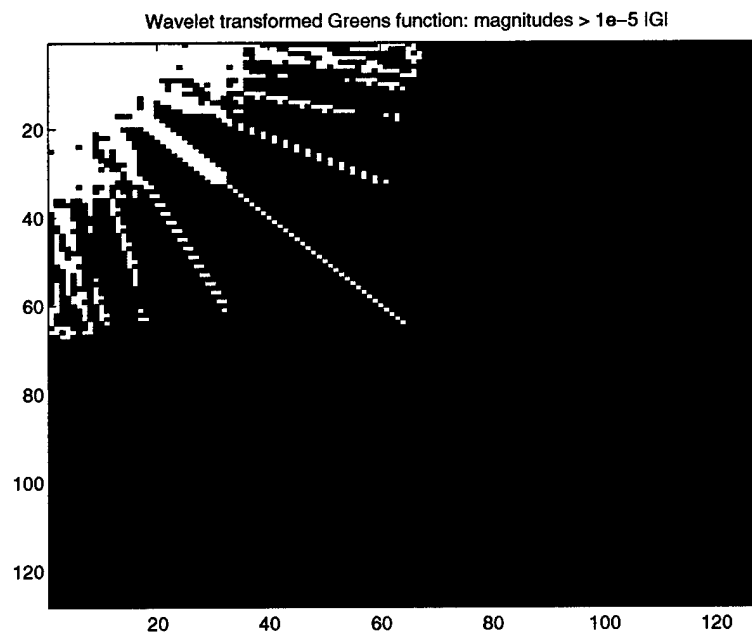


Figure 25: Intensity image of magnitude of wavelet-transformed Green's function at 1000 Hz: coefficients greater than  $1e-5$  times norm of  $K$

length of the beam, while the black bars indicate the forcing input.

Figure 27 shows the performance results for the same cases, where the neutralization transfer function is approximated using our wavelet compression approach. In this case, the wavelet sparsification used was such that 48 percent of the coefficients were retained.

Finally, in Figures 28 and 29 we show performance results in the presence of noise for 20 dB and 10 dB SNRs, respectively, where the neutralization transfer function is approximated again using the same 48 percent of the coefficients.

## 6.2 Flexible Plate Results

In this section we illustrate our control approach for the case of controlling vibrations in a  $1\text{ m} \times 1\text{ m}$  flexible plate with a 16 by 16 array of transducers. This example focuses on the ability of the wavelets to compress the plant  $P$ , which, in the case of our example, is taken to be the operator that maps point forces uniformly distributed on the plate into normal velocities at the same locations. Our control objective is to minimize the vibrations at the sensor outputs due to external disturbance forces by designing a feedback controller whose inputs are the sensor outputs on the plate and whose outputs are the control signals to the actuator inputs. This maps directly into the problem of minimizing the norm of the transfer function in eq.(1), where the transfer functions  $T$ ,  $S$ , and  $A$  are all equal to  $P$ .

Figure 30 is a plot of the velocity response of the plate due to a point force in the middle of the northwest quadrant of the plate at 250 Hz. The overall transfer function  $P$ , whose inputs include actuator point forces sampled uniformly throughout the plate and whose outputs include sensor velocity measurements at points collocated with the actuators, maps for each frequency all possible actuator inputs to all possible sensor outputs. Thus, at a single frequency we can think of  $P$  as a collection of plots as in Figure 30, one for each of the 16 actuator locations. Figure 31 depicts this at 250 Hz. One can think of this plot as a 16 by 16 checkerboard, where each square shows the velocity response due to an input whose location corresponds to the location of the square with respect to the checkerboard. In Figure 31, we also show the wavelet-transformed  $P$ , which is obtained using a 4-dimensional transform derived from tensor products of 1D transforms. One immediately notices that the amplitudes of the transfer function in the wavelet domain are much more concentrated into a sparse set of locations. In fact if we threshold the amplitudes to retain only 10 percent of the channels, we have the channels depicted in Figure 32. Using these channels as an approximation of  $P$  for our neutralization filter, we get an 8 percent error.

We now show how the approximation error in our wavelet-approximated neutralization filter affects closed-loop control performance. In particular, we show the effects of neutralization error on a Q-parameter design using a nearest-neighbor structure. For this structure each actuator control signal input is a function of the sensor outputs at each of the eight nearest locations surrounding the actuator plus the output of the sensor collocated with the actuator. Figure 33

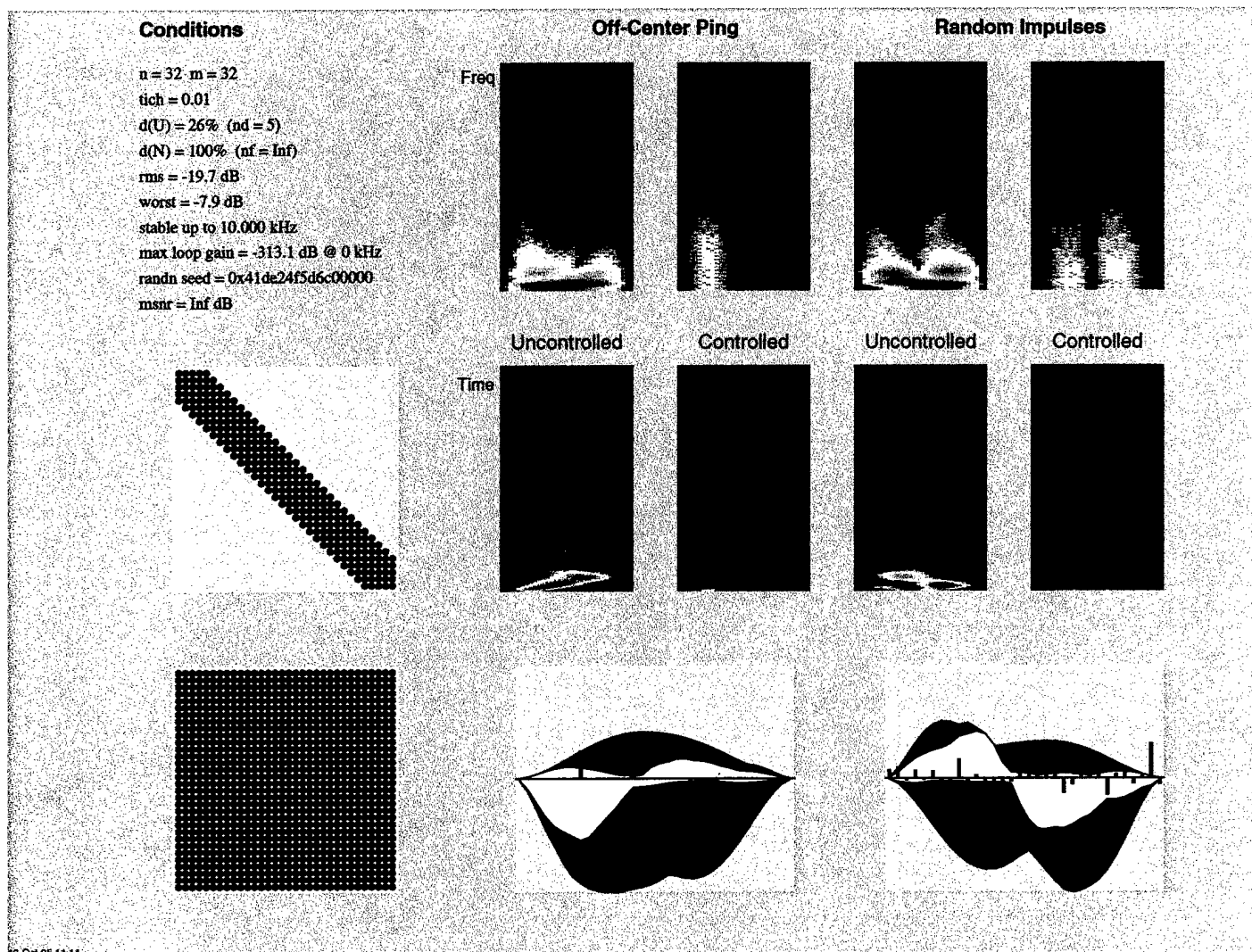


Figure 26: Frequency and time domain plots of controlled vs. uncontrolled responses, using banded Q-parameter and full neutralization (no wavelet compression used)

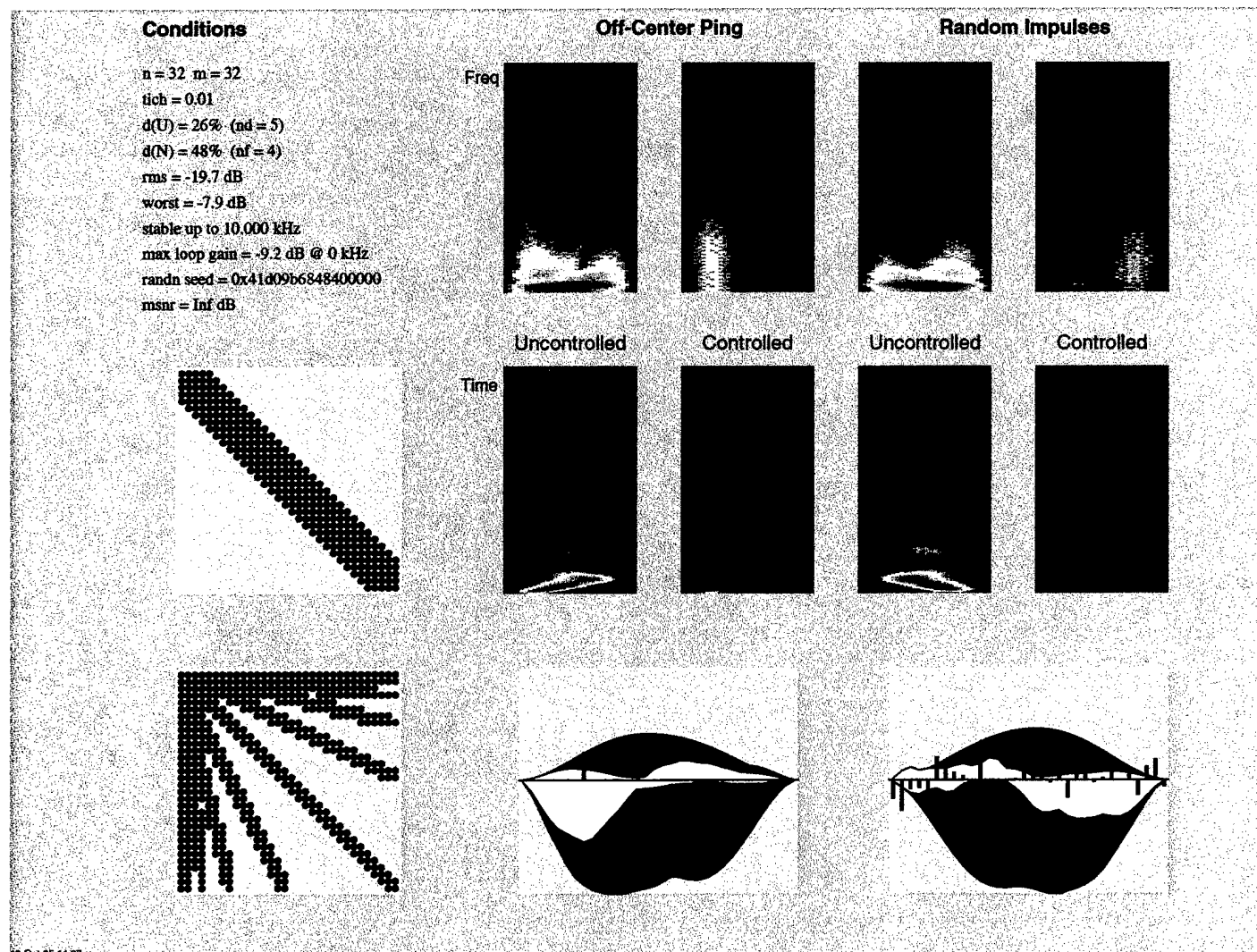
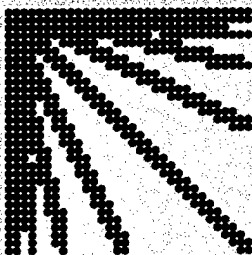
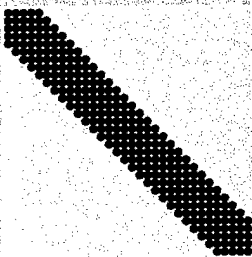


Figure 27: Frequency and time domain plots of controlled vs. uncontrolled responses, using banded Q-parameter and wavelet compressed neutralization

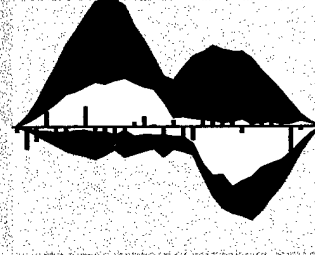
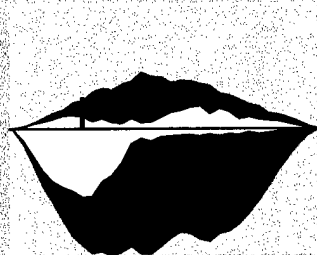
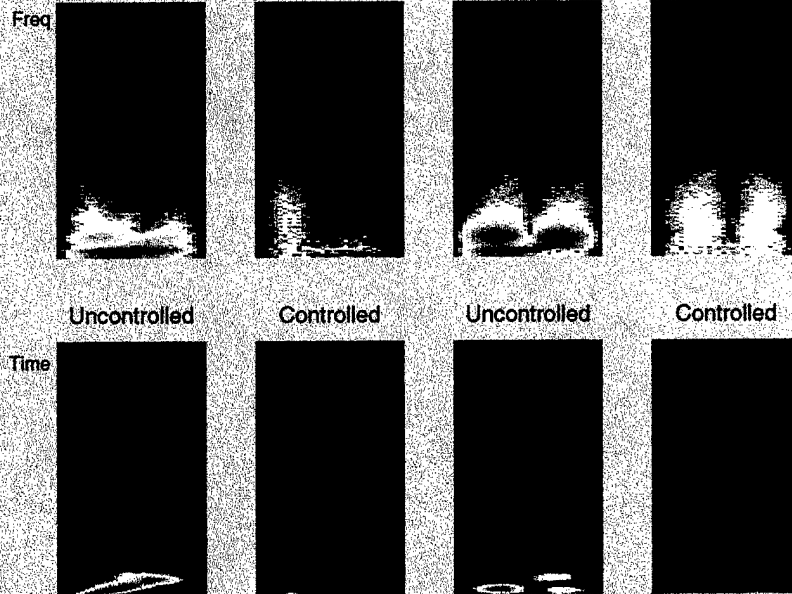
### Conditions

$n = 32$   $m = 32$   
 $\text{fich} = 0.01$   
 $d(U) = 26\%$  ( $nd = 5$ )  
 $d(N) = 100\%$  ( $nf = 4$ )  
 $\text{rms} = -16.7$  dB  
 $\text{worst} = -7.4$  dB  
 stable up to 10.000 kHz  
 $\text{max loop gain} = -9.2$  dB @ 0 kHz  
 $\text{randn seed} = 0x41babb3ad0000000$   
 $\text{msnr} = 20$  dB



### Off-Center Ping

### Random Impulses



13-Oct-95 11:40

Figure 28: Frequency and time domain plots of controlled vs. uncontrolled responses, using banded Q-parameter and wavelet compressed neutralization: 20 dB SNR



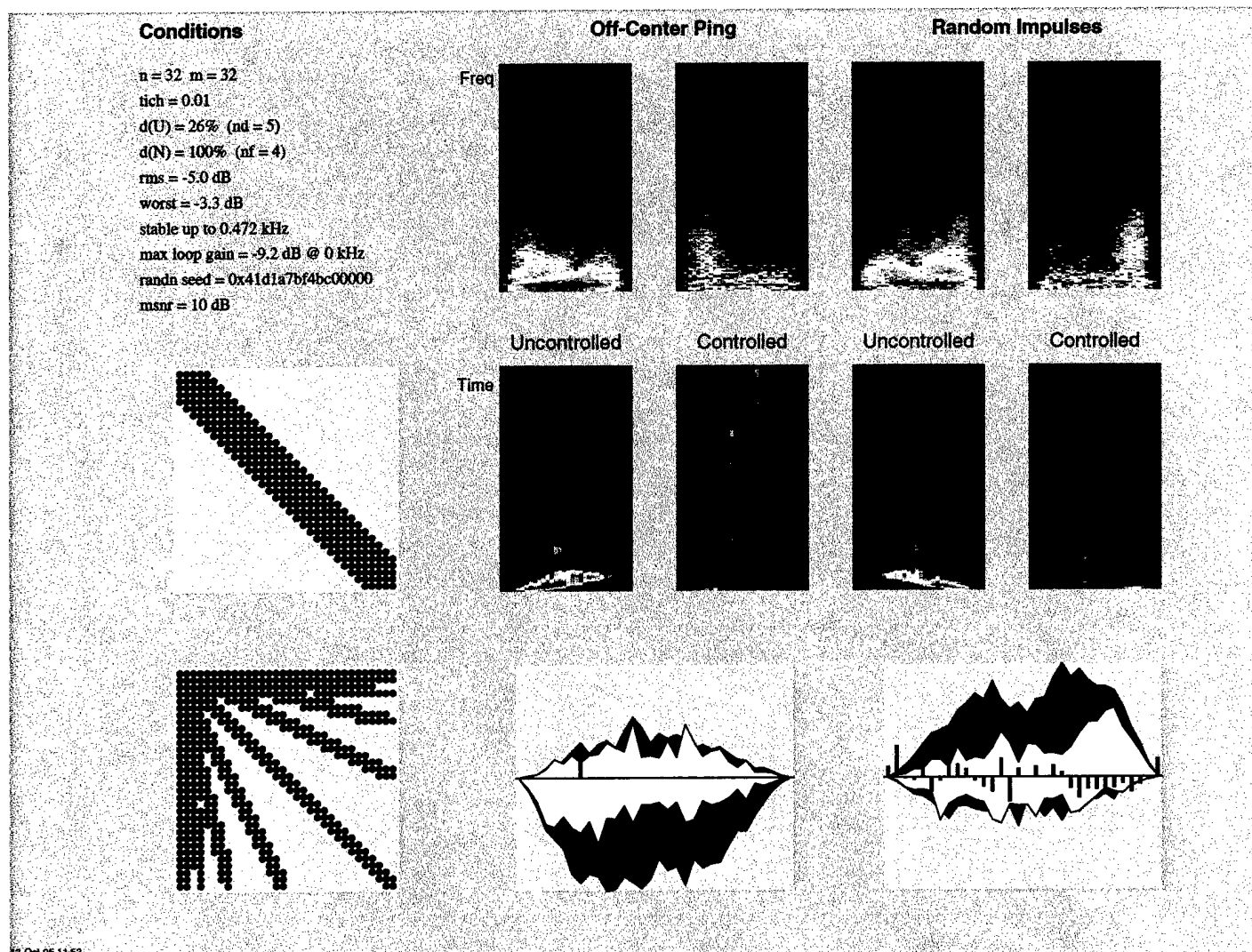


Figure 29: Frequency and time domain plots of controlled vs. uncontrolled responses, using banded Q-parameter and wavelet compressed neutralization: 10 dB SNR

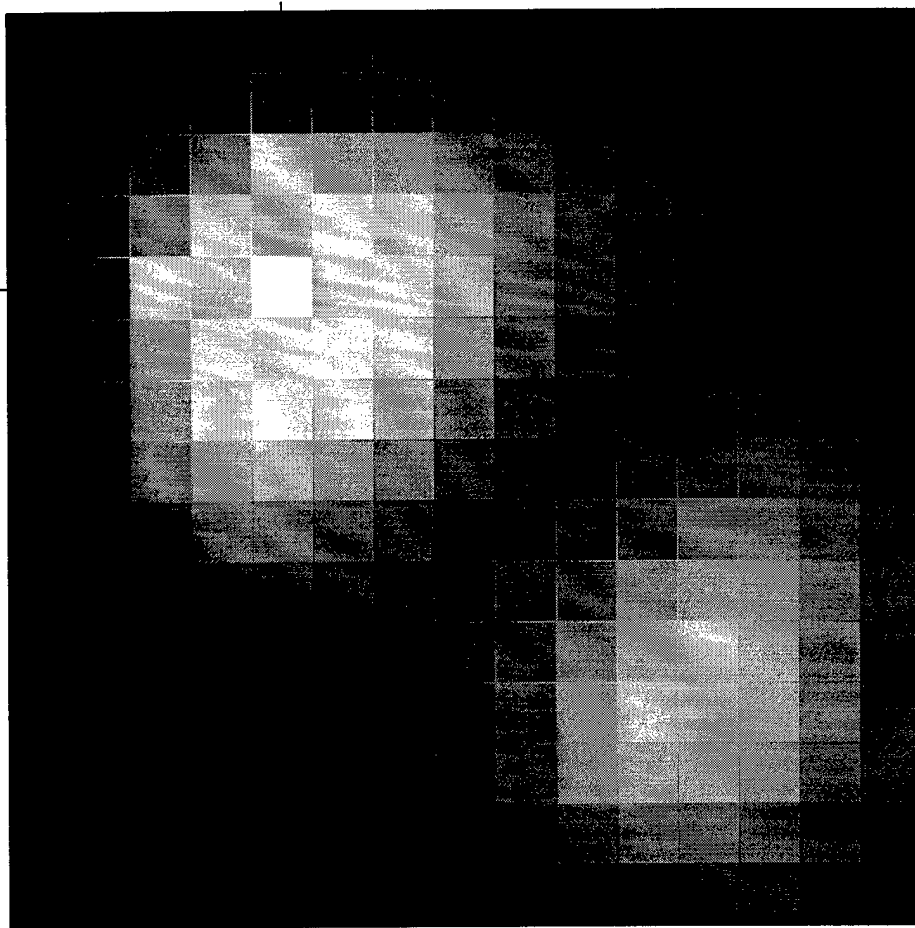


Figure 30: Transfer function response at 250 Hz due to force input in middle of northwest quadrant

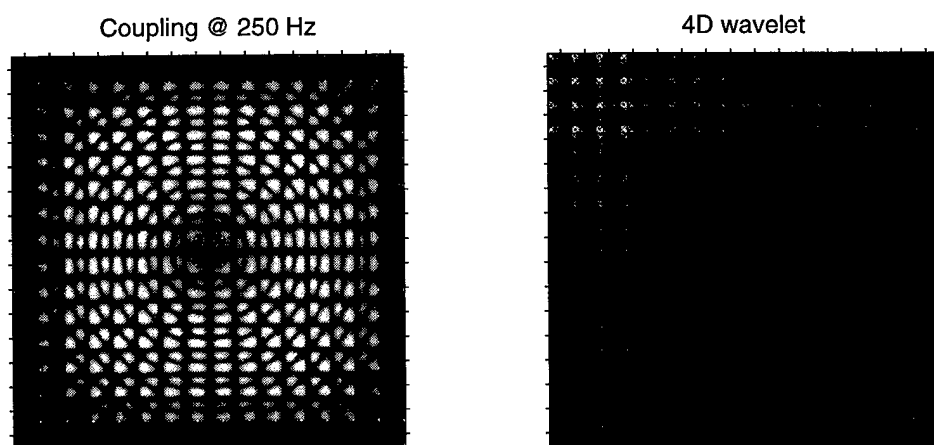


Figure 31: Transfer function at 250 Hz: (1)  $P$  (2) wavelet-transformed  $P$

10% wavelet mask for neutralization

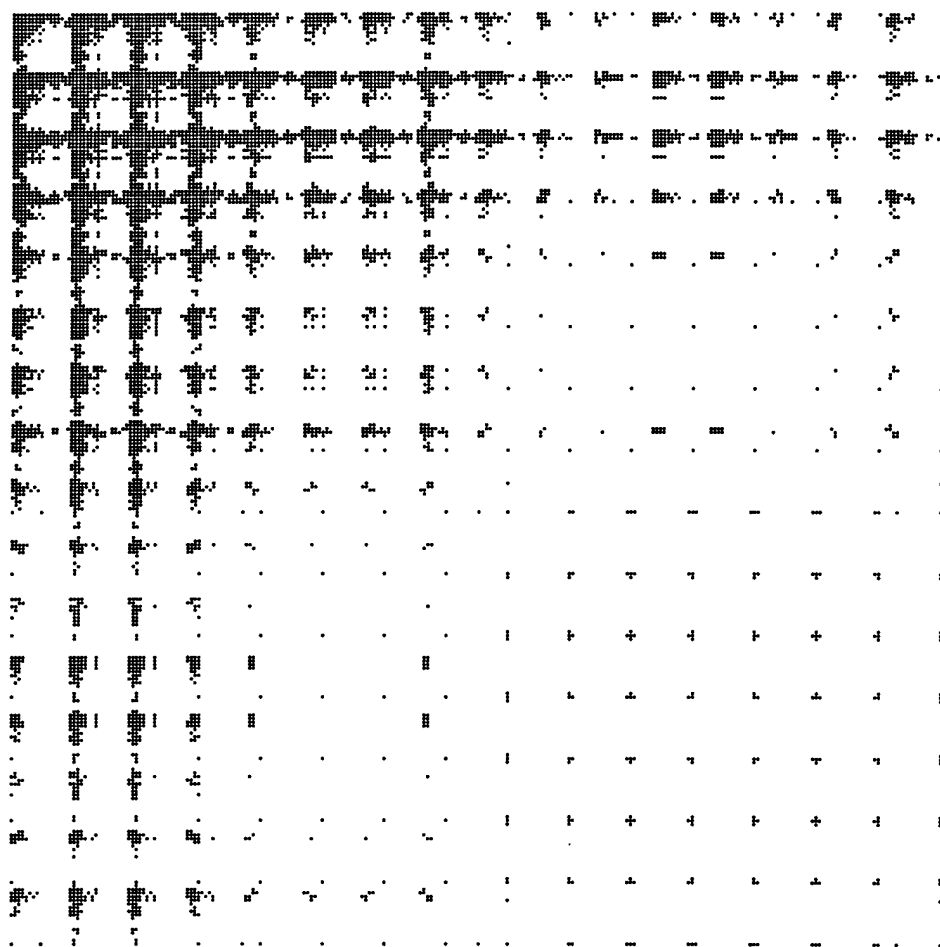


Figure 32: Nonzero channels of wavelet-transformed  $P$  for 10 percent density

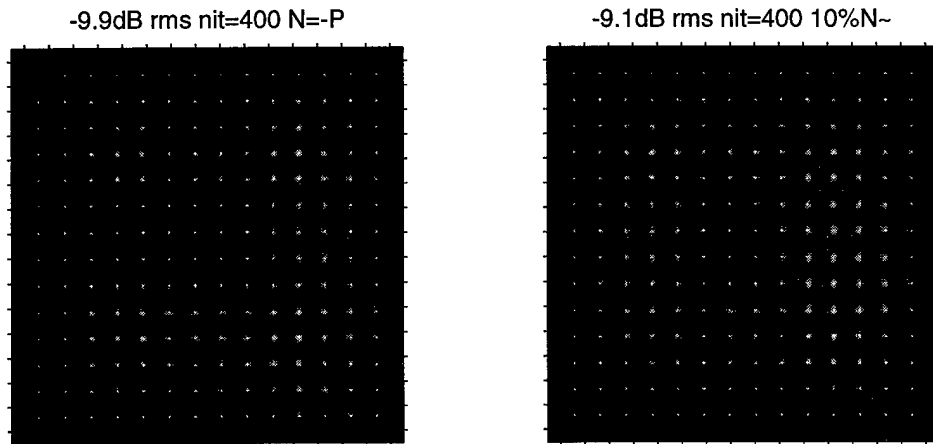


Figure 33: Closed-loop performance at 250 Hz: (1) perfect neutralization and (2) wavelet-transformed neutralization

shows the closed-loop control performance at 250 Hz using our designed Q-parameter with (1) perfect neutralization and (2) wavelet-approximated neutralization. These plots are normalized to be compared to the uncontrolled response shown in the first plot of Figure 31. The rms performance over a 0-1550 Hz band for case (1) is 9.9 dB, while for case (2) it is 9.1 dB. Thus, we only get a 0.8 dB degradation in performance using a neutralization filter with only 10 percent of the original channels. In other words, this is a 90 percent reduction in interconnection complexity with very little degradation in performance relative to using full interconnections.

To motivate how the multirate structure for the neutralization filter would work, we show the impulse response of several channels of the wavelet-approximated neutralization filter. Figure 34 shows impulse responses for (1) several channels of  $P$  and (2) several channels of the wavelet-transformed  $P$  corresponding to, from top to bottom, coarse, medium, and fine scales, respectively. Note that the coarser-scale channels exhibit lower bandwidth responses, while finer-scale channels exhibit shorter responses. This structure forms the basis of the multirate scheme outlined in the previous section.

### 6.3 Conclusions

We have described an approach to controlling large numbers of sensors and actuators via a multiscale/multirate processing scheme. By implementing the controller in the Q-parameterization we have identified two complementary sources of a processing bottleneck. In the neutralization path of the controller, the problem lies in the interconnections between actuators and sensors, while in the feedforward path of the controller, the problem is in the interconnections between sensors and actuators. For many physical systems, the neutralization path transfer function  $P$ , which represents the coupling between actuators and sensors, is predominantly

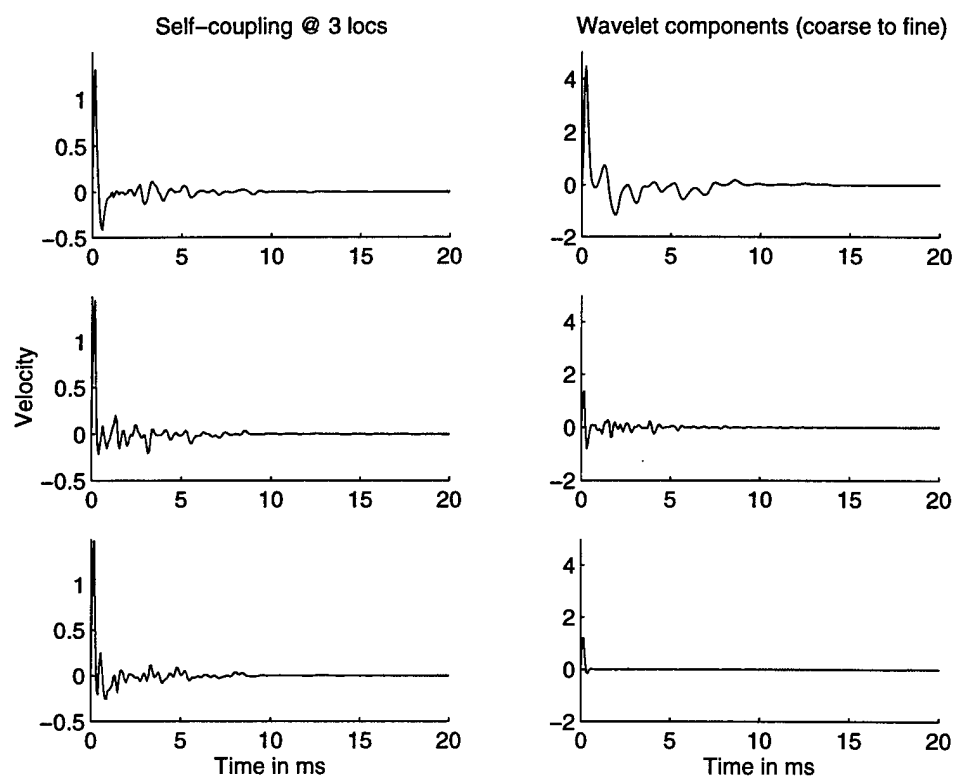


Figure 34: Impulse responses: (1)  $P$  and (2) wavelet-transformed  $P$

smooth, and compression can be obtained by performing a wavelet transform on the actuators and sensors, then implementing a sparse operator between the coefficients. Results on this were given for the both the case of a flexible beam as well as the case of a flexible plate.

The feedforward path transfer function  $Q$  can also be designed in the multiscale domain, giving us the same sparse interconnectivity as in the case of the neutralization transfer function. For both  $P$  and  $Q$ , the multiscale structure induces a multirate structure in the time domain that gives further computational efficiencies. In particular, coarse-scale components can be processed at lower sampling rates, while fine-scale components are processed at higher rates but with shorter filters.

In summary, the savings afforded by our overall multiscale/multirate methodology in processor communication, computation, and its inherent scalability, offers promise for controlling spatially varying, wideband phenomena. The methodology also offers a reasonable scheme for allowing the controller to optimally process a dense array of transducers for a given problem, obviating the need for customizing the transducer layout to a particular problem.

## **7 RESULTS OF EXPERIMENTAL VALIDATION**

### **7.1 PSU Experimental Setup**

This section summarizes the data acquisition procedure used in the experimental investigation of the dynamic response of a fully clamped panel. The investigation was conducted in order to provide SRI with experimentally measured structural transfer functions of a panel such that realistic data is available for the design of a multichannel control circuit. The measurements were performed at the Center for Acoustics and Vibration Noise Control Laboratory located at the Penn State University.

The measured structural transfer functions provide the relationship between point forces and velocities at positions on the panel. Several methods of obtaining the structural transfer functions were conducted, each method varying in the type of input force and sensing transducer used. The variation in the input and sensing transducers was performed in order to achieve the needed accuracy in transducer positioning and measurement repeatability and to provide a common phase reference between the transfer functions as required by SRI.

The measurements were performed on a 34x34x0.125 inch aluminum panel which is partially covered with an unconstrained damping layer to provide realistic damping. The panel is mounted to a wall opening of a transmission loss facility and the mounting approximates clamped boundary conditions, Figure 37. Figure 35 shows a photograph of the laser vibrometer side of the panel, while Figure 36 shows a photograph of the hammer/shaker side of the panel. The panel is discretized into  $n \times n$  patches of equal size, the corners of which are the positions where the measurements are taken (sensing positions) and control forces are applied (excitation positions). It should be noted that the panel has symmetric boundary conditions enabling the principle of reciprocity to be used, i.e., the interchanging of excitation and sensing positions will result in identical transfer functions.

#### **7.1.1 Experiment 1 - Frequency Domain Analysis**

The goal of the initial experimental investigation was to obtain a set of transfer functions that could describe completely the vibrational motion of the plate. These transfer functions were obtained using a modal impact hammer as the input force and an accelerometer as the dynamic sensor, Figure 38. The accelerometer was mounted to the panel at a set of specified sensing positions and the modal impact hammer (manual) excited the panel at a set of specified excitation positions. The signals from the two transducers were sent to an HP Analyzer, where the structural transfer function was computed and stored.

This procedure was deemed unexceptionable for two reasons. First, the repeatability of the excitation force produced by modal impact hammer was questionable due to human error, i.e. the impact was excited manually, and thus the excitation force was not always normal to the

panel. Second, it was believed that the mass of the accelerometer altered the panels response when mounted to the panel at different sensing positions.

### **7.1.2 Experiment 2 - Frequency Domain to Time Domain Analysis**

A second experimental investigation was performed to eliminate the previously mentioned problems and to reduce the amount of recorded data by allowing the input force to remain at a single position while only moving the sensor to set a sensing locations. The experimental transfer functions were obtained using a uni-morph piezoelectric shaker as the force input and a Polytech laser vibrometer as the sensor, Figure 39. The shaker was attached to a force transducer, which was in turn mounted to the panel at a specified position. The HP Analyzer provided a random noise signal to the shaker. This method of excitation allowed for a repeatable input force. The laser vibrometer is a non-contact sensor and therefore eliminates the mass loading effects of the accelerometer. The laser vibrometer was manually moved to set of sensing positions in order to measure to response of the panel.

It was determined that the manual positioning of the laser vibrometer did not provide the measurement position accuracy required. Consequently, a motorized positioning system for the laser vibrometer was developed, allowing for accurate sensor positioning, and the data was retaken. The use of the mounted shaker and motorized positioning of the laser vibrometer produced the required accuracy in measurement repeatability and transducer positioning required in developing the multichannel control circuit.

It was later determined by SRI that when these transfer functions were converted from the frequency domain to the time domain, there was a loss of phase reference between each transfer function. The loss of phase reference is inherent when using random excitation.

### **7.1.3 Experiment 3 - Frequency Domain to Time Domain Analysis**

In experiment 3, an electronic impulse hammer was used as the excitation force because it provided both a common phase reference between transfer functions and a repeatable excitation force. The electronic impulse hammer was mounted to rigid frame located adjacent to the panel, Figure 40. The mounting procedure was designed such that it was easy to manually move the impulse hammer to any excitation position. The laser vibrometer was positioned at a set of sensing positions using the motorized positioning system.

Since this experimental set-up achieved the needed accuracy in transducer positioning and measurement repeatability and provided a common phase reference between the transfer functions, it was requested by SRI that data was taken for multiple excitation and sensing positions (similar to experiment 1, except a complete description of the vibrational motion of the plate was not required).



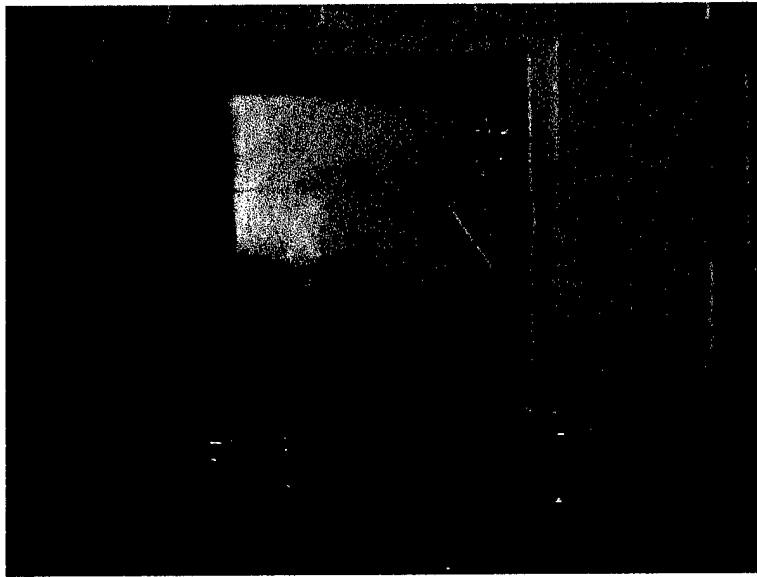


Figure 35: Laser vibrometer side of panel

#### 7.1.4 Conclusion

A means of obtaining experimental structural transfer functions of a plate was developed in order to provide SRI with realistic data needed to design a multichannel control circuit. The development of an experimental set-up to obtain the structural transfer functions was described. The experimental set-up met the required accuracy in measurement repeatability and transducer positioning and also provided a common phase reference between the individual transfer functions.

## 7.2 Validation of Green's Function Properties Using PSU DATA

The data taken by PSU was compared against model data using the modal plate model. Careful adjustment of the model parameters yielded a reasonable agreement between predicted and measured responses. This provides us confidence in using the data to perform tests in validating our control approach. Figure 41 shows the magnitude and phase of the response along 64 evenly spaced points along a strip of the plate due to point forcing at a single location. The response as a function of frequency is shown for both the model prediction as well as the measured response of the laser-vibrometer output.

In order to validate our wavelet transfer function compression approach, we examined the PSU data for intrinsic properties of the response data to impulsive excitations. In particular, as shown in [3], the impulse response of a structure should exhibit discontinuities at certain derivatives at the location of the impulse. This behavior enables the use of wavelets to compress the transfer function from inputs to outputs. Figure 42 shows the velocity response

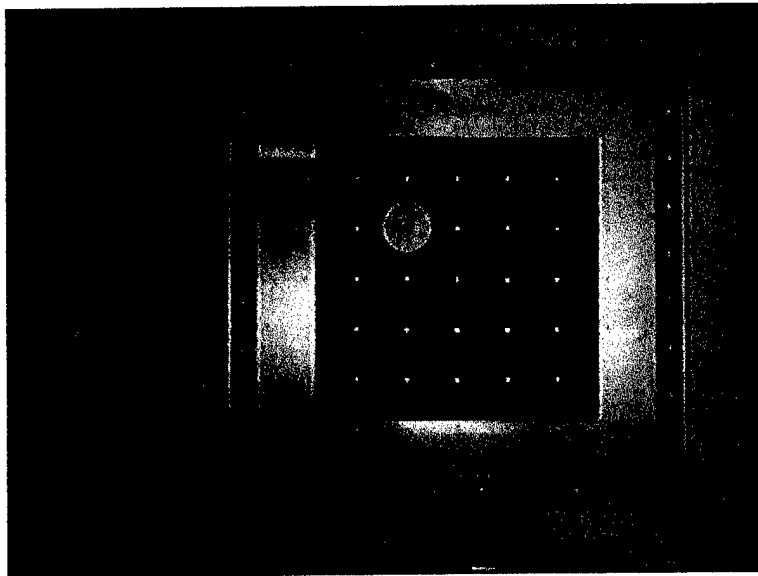


Figure 36: Hammer/shaker side of panel

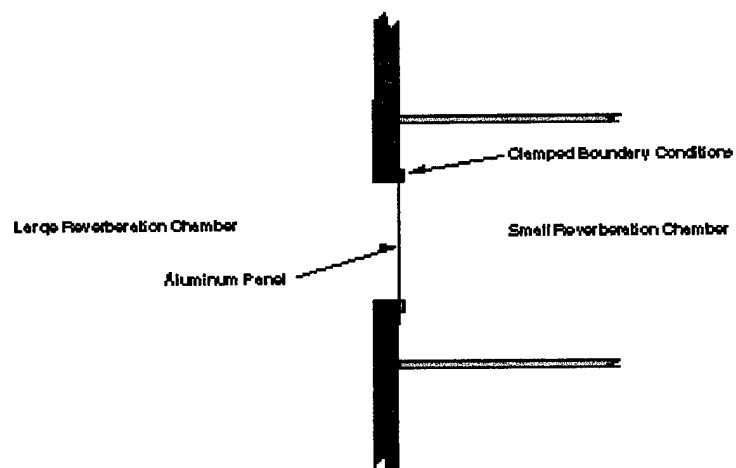


Figure 37: Diagram of Panel Mounted in Wall Opening of Transmission Loss Facility

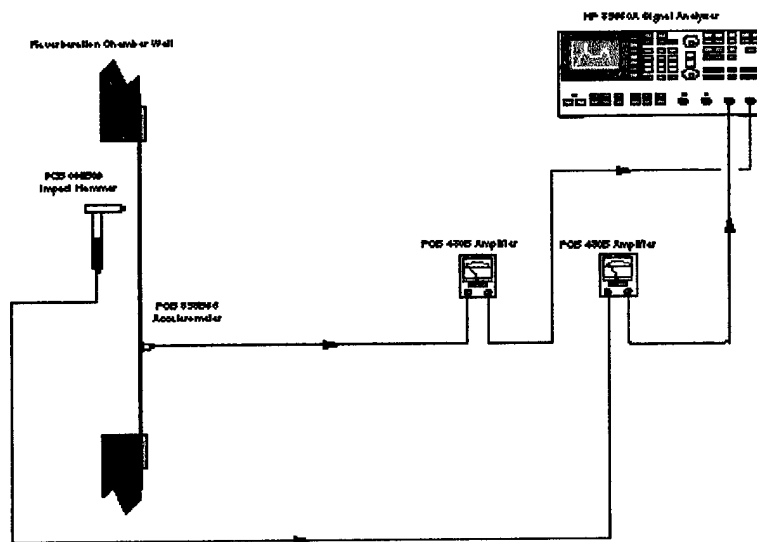


Figure 38: Diagram of Experiment 1 Set-up

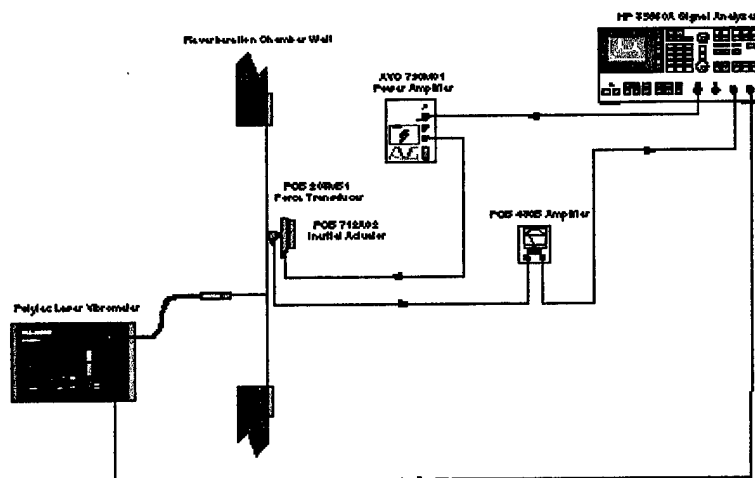


Figure 39: Diagram of Experiment 2 Using Laser Vibrometer

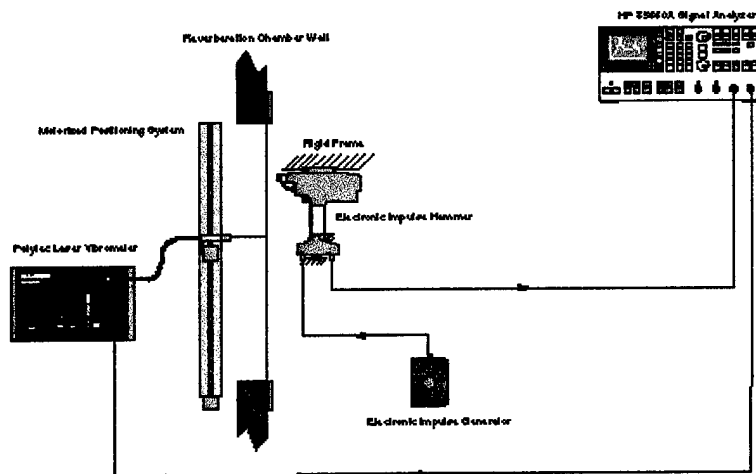


Figure 40: Diagram of Experiment 3 Set-up

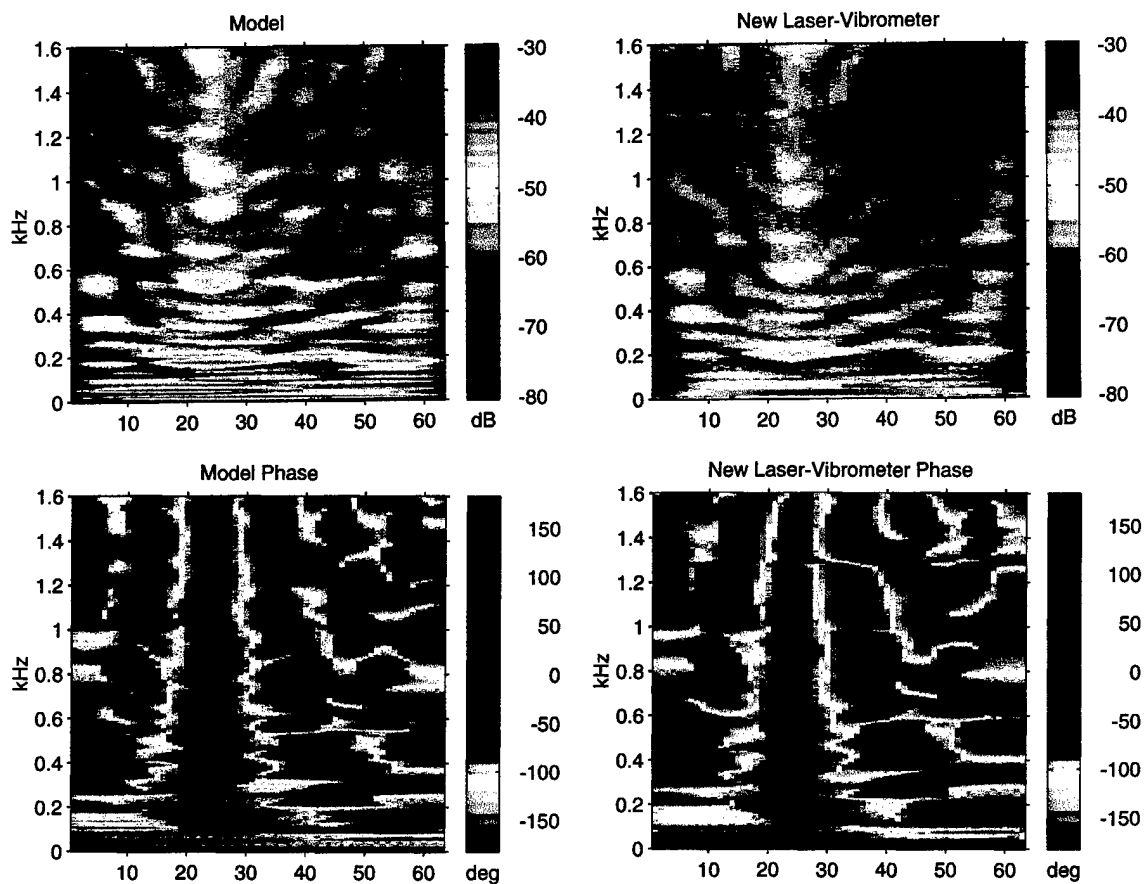


Figure 41: Model and experimental transfer function comparison: upper left - modeled magnitude, upper right - measured magnitude, lower left modeled phase, lower right - measured phase

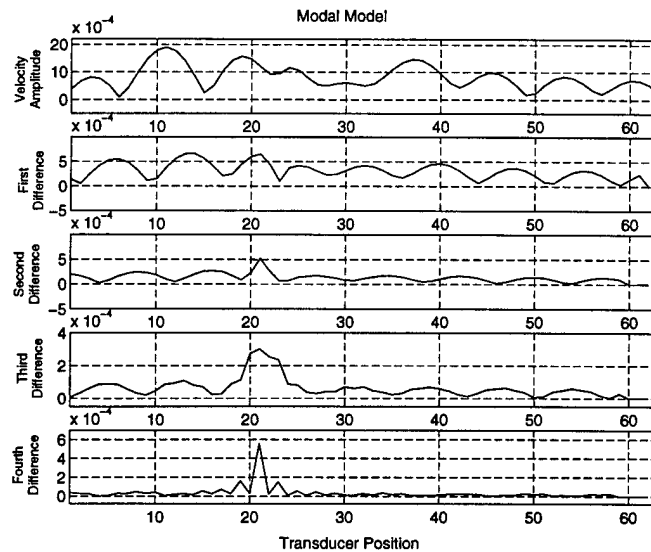


Figure 42: Velocity response due to force input using model data.

along a strip of the plate (off center) due to a force input at a single location. The velocity at 64 evenly spaced points are shown due to the force input, using model data. Note that the response peaks more and more at the location of the forcing point as a function of the order of the derivative. This peaking as a function of derivative order is precisely the property is exploited by wavelet transforms with vanishing moments in compressing transfer functions from inputs to outputs.

Figure 43 shows the result of measuring the velocity at these 64 evenly spaced points due to a shaker force input. The top plot shows the raw response measured by PSU, while the subsequent plot shows the result of taking derivatives (using finite differences) based on this raw data. This plot shows excellent validation of the wavelet transfer function compression approach, since the peaking property is clearly exhibited in the measured data.

### 7.3 Wavelet Compression Using PSU Data

In this section we report results on using the PSU data to show wavelet compression of the neutralization transfer function. In this case, the coupling from actuator input to sensor output along a strip on the plate was used. As in the case of the derivative test, 64 evenly-spaced sensor points were used. Only 16 evenly-spaced actuation points were used, due to limitations in collecting the data. These 16 were chosen to be collocated with the first 16 sensor points. Thus, the transfer function measured has 16 inputs and 64 outputs. Figure 44 shows the magnitude of the transfer function at a single frequency and the magnitude of the wavelet transform at that frequency. Note that the “finger”-like patterns are evident in the wavelet transform of the transfer function. Since we only had access to the first 16 inputs, rather than

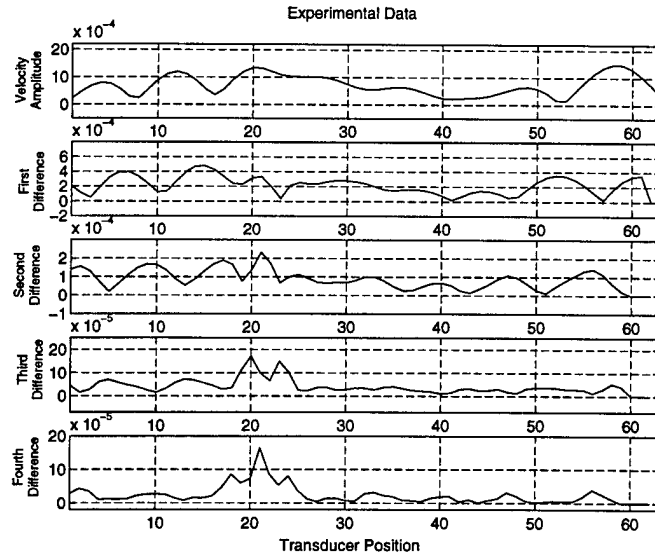


Figure 43: Velocity response due to force input using PSU measured data.

the full 64, we could only seek to verify that the pattern exhibited matched the subset of the full finger pattern corresponding to a 64 input 64 output system.

To quantify how well the prediction of the pattern based on our physical smoothness notions matched the measured data, we applied the our predicted pattern mask to the measured transfer function, i.e., we zeroed out the coefficients that were not included in the mask. The result is shown in Figure 45.

To summarize the performance of the compression achieved using this mask, we reconstructed the transfer function in physical coordinates and determined the relative error to be only .017 percent. The original and reconstructed transfer function can be visually compared in Figure 46.

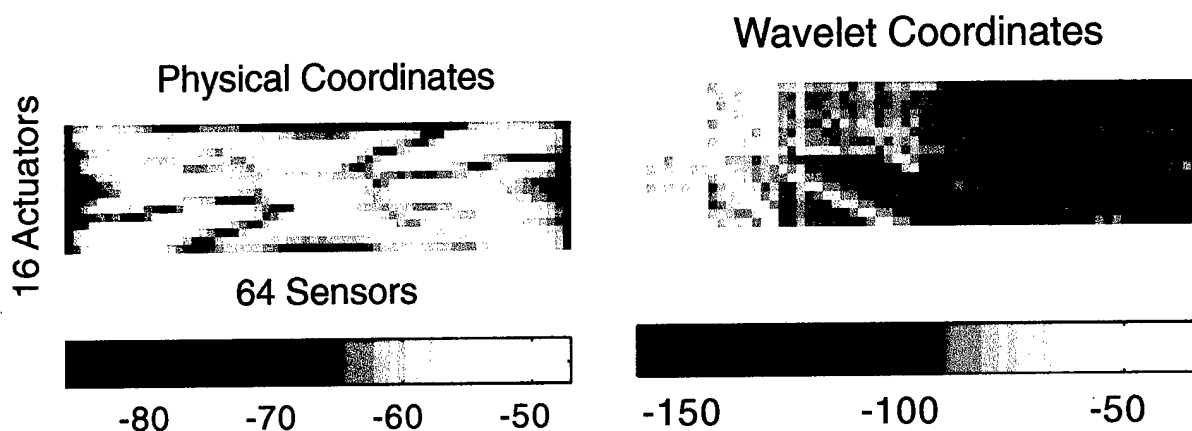


Figure 44: (l) Transfer function magnitude in physical coordinates (r) Magnitude of transfer function in wavelet coordinates.

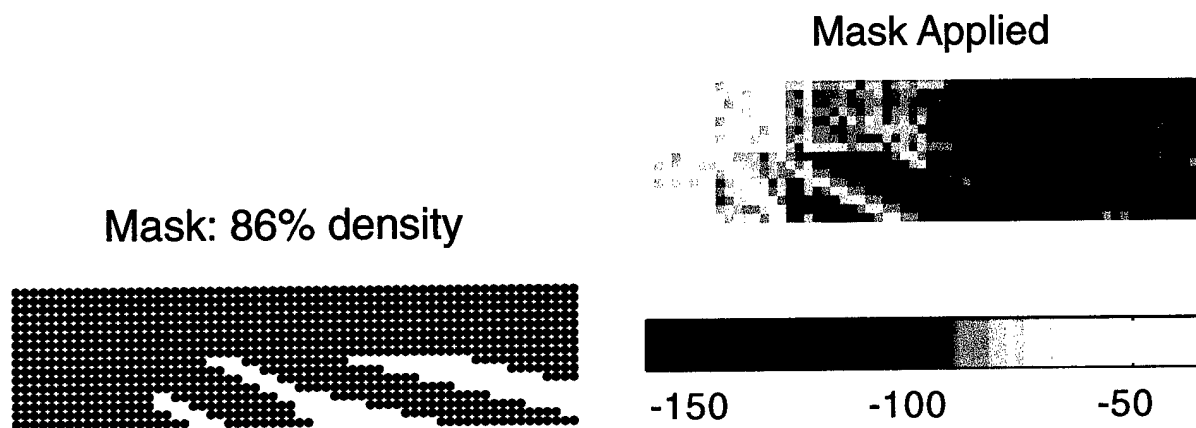


Figure 45: (l) Predicted mask of significant coefficients (r) Mask applied to measured transfer function.

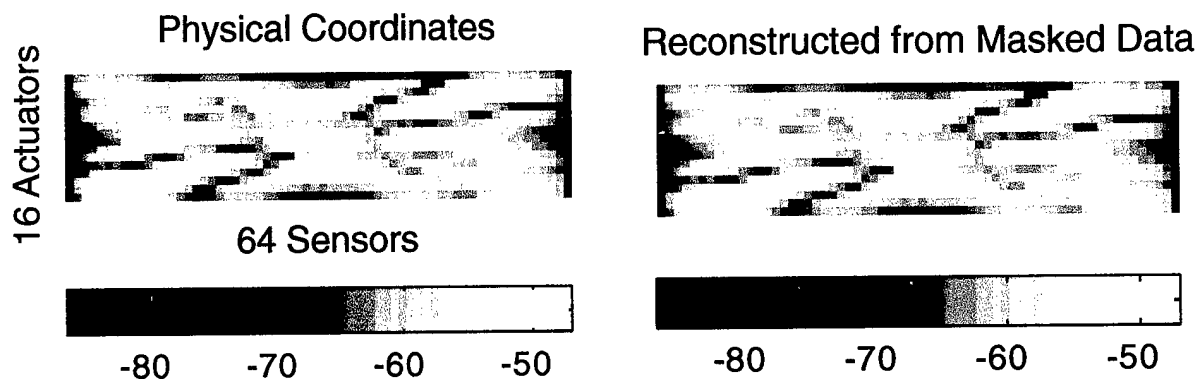


Figure 46: (l) Transfer function magnitude in physical coordinates (r) Reconstructed transfer function magnitude in physical coordinates.

## 8 TECHNOLOGY TRANSFER

The purpose of developing control technology for smart materials is to provide enabling technology that will be applied to systems with large numbers of sensors and actuators. In this section we summarize past and continuing efforts to effect this transfer from research to applications.

There are two areas of development in which efforts at technology transfer has occurred: transducer selection and transfer function compression. As discussed in Section 5, the transducer selection or placement results of this program are not restricted to systems with large numbers of transducers, so that work has been tested more and is closer to application than the compression results. Among the applications have been: a Navy structural acoustic control program, the SPICES program, and a NASA aircraft cabin quieting program. The application to SPICES is the primary example in [11], which is attached as Appendix B.

Since the "break-even" point for the compression methodology is somewhere on the order of 64 transducer pairs, a considerably greater investment in transducers is required before an application or demonstration can benefit from using our results instead of alternative control technology. Recent and current demonstrations and programs have typically focussed on development of individual transducers or manufacturing technology. For reasons of maximizing the tangible results of a fixed amount of funding these issues have received priority. However, technology such as KIKO will be necessary to take these efforts beyond "toy" demonstrations, and it is imperative that KIKO be ready when the applications are ready for that step. We summarize the additional work we believe needed to be appropriately ready in Section 9.

It appears that a first application may well be acoustic noise control. We have had numerous discussions with groups working on such applications in aircraft cabin quieting (the same NASA project mentioned above), attenuation of acoustic noise for rocket payloads, underwater acoustics (also in the DARPA Smart Materials program), and the DARPA MEMS program (SRI's acoustic noise suppressor program). In order to assist in control development (and possible KIKO application) for the DARPA Smart Wing program, in which around 130 actuators are anticipated for a full scale system, we have a consulting role in the current phase of that program. We also believe that a variation of this technology may be applicable to our current work on the ONR Power Electronic Building Block (PEBB) program. (This is a considerable departure from the partial differential equation-based theoretical justification in [3] included in Appendix C, but the tremendous proliferation of transducers anticipated in the use of PEBBs requires some form of transfer function compression and hierarchical control, and the wavelet approach may well provide the right set of coordinates in which to reduce the complexity of models for the desired and required interconnections.)

We recognize that continuing efforts are required to bring this work to its useful application, and we believe that KIKO will figure prominently into future programs as demonstrations are developed requiring the large numbers of transducers for which KIKO is intended.



## 9 CONCLUSIONS

A great variety of military and commercial applications have anticipated requirements for feedback control systems using large arrays of sensors and actuators, with numbers of transducers on the order of 100, 1000, or more. These applications include acoustic noise cancellation, vibration suppression, adaptive optics and control of turbulence in fluids.

The KIKO methodology comprises a procedure for designing a controller that is locally interconnected in a multiscale hierarchy, and a high-level processor architecture for implementing the controller in a scalable manner. A key feature of KIKO is that it provides a way to implement globally optimal control designs via hierarchical processing and interconnection. This is in contrast to other locally interconnected control designs, which can only provide local optimization and cannot address global criteria.

The design method takes as input transfer functions which are assumed to be measured on the system using sensor and actuator arrays. Based on these measured transfer functions the method uses efficient numerical algorithms to design a controller that is locally interconnected in a banded multiscale representation. The high-level processor architecture is based on the fast wavelet transform implemented in a distributed manner. An approach for integration of multirate techniques into the multiscale methodology has been developed.

The design procedure has been tested on closed-loop control simulations of beams and plates, and experimental work with a plate confirmed the validity of key assumptions. Transducer placement work focussed on heuristic subset selection from arrays, although with guaranteed performance bounds.

Although long term application requirements suggest major extensions of KIKO (say, to adaptive and nonlinear versions), in order to efficiently exploit and extend KIKO developments to date, further near-term work is needed to ensure that KIKO technology is ready for near term demonstrations and applications that will need it.

The most pressing near-term need for KIKO is to provide a closed-loop control demonstration of its capability. Otherwise, further needed development might wait until a demonstration is planned for other purposes, and it is discovered by trying and failing that other, existing, control methodology is not adequate for the job.

The most productive next direction for continuing research is likely to be the investigation of second generation wavelets. This would build strength in three important issues: treating irregularly spaced transducers, treating bounded domains of transducer distribution, and reducing the break-even point at which KIKO has an advantage over conventional approaches.

## 10 REFERENCES

- [1] L. Andersson, B. J. Nathan Hall, and G. Peters. Wavelets on closed subsets of the real line. In *Recent Advances in Wavelet Analysis*, pages 1–61. Academic Press, 1994.
- [2] G. Beylkin, R. Coifman, and V. Rokhlin, “Fast Wavelet Transforms and Numerical Algorithms I,” *Communications on Pure and Applied Mathematics*, Vol. XLIV, pp. 141–183, 1991.
- [3] K. C. Chou and G. S. Guthart, “Wavelet Analysis of Transfer Functions for Control of Euler-Bernoulli Beams,” SRI Internal Memorandum, February 1995 (submitted for publication in *International Journal for Multidimensional Systems and Signal Processing*).
- [4] J. J. Clark, M. R. Palmer, and P. D. Lawrence, “A transformation method for the reconstruction of functions from nonuniformly spaced samples,” *IEEE Trans. Acoust., Speech, Signal Processing*, ASSP-33:1151–1165, 1984.
- [5] D. Cochran and J. J. Clark, “On the sampling and reconstruction of time-warped bandlimited signals,” in *Proc. IEEE Intern. Conf. Acoust., Speech, Signal Processing*, pages 1539–1541, Albuquerque, April 1990.
- [6] A. Cohen, I. Daubechies, and P. Vial, “Wavelets on the interval and fast wavelet transforms,” *App. and Comp. Harm. Anal.*, 1:54–81, 1993.
- [7] I. Daubechies, “Orthonormal bases of compactly supported wavelets,” *Communications on Pure and Applied Mathematics*, Vol. XLI, pp. 909–996, 1988.
- [8] J. C. Doyle, B. A. Francis, A. R. Tannenbaum, *Feedback Control Theory*, Macmillan, New York 1992.
- [9] B. Francis, *A Course in  $H_\infty$  Control Theory*, Springer-Verlag, 1987.
- [10] G. H. Golub and C. F. Van Loan, *Matrix Computations*, Johns Hopkins University Press, 1983.
- [11] L. P. Heck, K. Naghshineh, and J. A. Olkin. “Transducer placement for broadband active vibration control using a novel multidimensional qr factorization,” to appear in *ASME J. Vibration and Acoustics*.
- [12] S.G. Mallat, “A Theory for Multiresolution Signal Decomposition: The Wavelet Representation,” *IEEE Transactions on Pattern Anal. and Mach. Intel.*, Vol. PAMI-11, July 1989, pp. 674–693.
- [13] Y. Meyer, *Ondelettes et opérateurs. I. Ondelettes. II. Opérateurs de Calderón-Zygmund. III. Opérateurs multilinéaires*, Hermann, Paris, 1990, English Translation, Cambridge Univ. Press, London/New York, 1993.

- [14] R. D. Richtmyer, *Difference Methods for Initial-value Problems*, Interscience Publishers, New York, 1957.
- [15] W. Sweldens, "The lifting scheme: A new philosophy in biorthogonal wavelet constructions," in A. F. Laine and M. Unser, ed., *Wavelet Applications in Signal and Image Processing III*, pp. 68-79. Proc. SPIE, 2569, 1995.
- [16] W. Sweldens, "The liftening scheme: A custom-design construction of biorthogonal wavelets," *J. of Appl. and Comput. Harmonic Analysis*, 3(2):186-200, 1996.
- [17] O. Rioul and M. Vetterli, "Wavelets and Signal Processing," *IEEE Signal Processing Magazine*, Vol. 8, No. 4, October 1991.

## A Euler-Bernoulli Green's Function

In this section, we derive an analytic expression for the Green's function of a forced Euler-Bernoulli beam with clamped ends. Figure 47 shows a schematic of the system. The beam is described by the well known differential equation with clamped boundary conditions

$$EI \frac{d^4 w}{dx^4} - \rho_s S \omega^2 w = F \delta(x - y),$$

$$w \equiv w' \equiv 0 \quad \text{at} \quad x = 0, L, \quad (56)$$

where  $E$  is Young's modulus,  $I$  is the rotary inertia of the beam cross section,  $S$  is the beam's cross-sectional area,  $\rho_s$  is the density of the beam,  $\omega$  is temporal frequency and  $w$  is the displacement of the beam's neutral surface as a function of  $x$ . The beam is of length  $L$  and has thickness  $h$ . For simplicity, we define the following nondimensional parameters

$$\bar{w} = \frac{w}{h} \quad \bar{x} = \frac{x}{L} \quad \bar{\omega} = \sqrt{\frac{\rho_s S L^4}{EI}} \omega \quad \bar{F} = \frac{F L^4}{EI h} \quad \bar{y} = \frac{y}{h}. \quad (57)$$

In terms of the nondimensional variables above, Equation 56 becomes

$$\frac{d^4 \bar{w}}{d\bar{x}^4} - \bar{\omega}^2 \bar{w} = \bar{F} \delta(\bar{x} - \bar{y}),$$

$$\bar{w} \equiv \bar{w}' \equiv 0 \quad \text{at} \quad \bar{x} = 0, 1. \quad (58)$$

In the following, we will use the nondimensional form above where we drop the overbars for convenience.

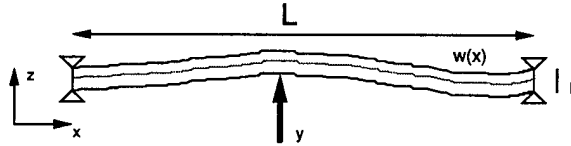


Figure 47: Schematic for the Euler-Bernoulli beam.

The derivation of the Green's function proceeds as follows. The beam is conceptually "split" into two sections on the left and right of the forcing point. The solutions for each side satisfy the original differential equation, a boundary condition on one side, and a set of matching conditions joining the solutions at the forcing point. The resulting solution is a weak solution of the original differential equation in that it is twice continuously differentiable on  $x \in [0, 1]$  with a jump discontinuity at  $x = y$  in the third derivative. The advantage of this weak solution form over the traditional series solution in terms of eigenvalues and eigenfunctions of the Sturm-Liouville problem is that in computations, the series solution must be truncated at some eigenvalue, giving rise to error akin to the Gibbs's phenomenon. The weak solution has no such truncation error. Furthermore, the discontinuity in the third  $x$ -derivative of the Green's

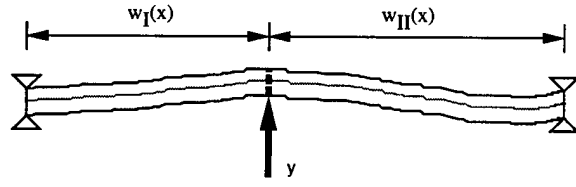


Figure 48: Splitting of the beam into two domains.

function intuitively reflects the effect of forcing in a way that the infinite sum of eigenfunctions to form this same step does not.

We start by splitting the beam into two parts about the forcing point, as shown in Figure 48. This gives for  $w$

$$w = \begin{cases} w_I & 0 \leq x \leq y \\ w_{II} & y \leq x \leq 1 \end{cases}, \quad (59)$$

with

$$\begin{aligned} \frac{d^4 w_I}{dx^4} - \omega^2 w_I &= 0 & 0 \leq x < y \\ w_I \equiv w'_I &\equiv 0 & \text{at } x = 0 \text{ and} \end{aligned} \quad (60)$$

$$\begin{aligned} \frac{d^4 w_{II}}{dx^4} - \omega^2 w_{II} &= 0 & y < x \leq 1 \\ w_{II} \equiv w'_{II} &\equiv 0 & \text{at } x = 1. \end{aligned} \quad (61)$$

In order for the split system to satisfy the original equation for  $w$ , a set of matching conditions at  $x = y$  must be satisfied. These are given by

$$w_I = w_{II}, \quad w'_I = w'_{II}, \quad w''_I = w''_{II}, \quad w'''_I - w'''_{II} = F \quad \text{at } x = y. \quad (62)$$

The appearance of the jump in the third derivative can be derived by evaluating Equation 58 on the left and the right of  $y$  and matching impulses. The resulting split system couples two boundary value problems.

The general solution for  $w_I$  and  $w_{II}$  is given by

$$\begin{aligned} w_I(x) &= c_1 \cos(\sqrt{\omega}x) + c_2 \sin(\sqrt{\omega}x) + c_3 \cosh(\sqrt{\omega}x) + c_4 \sinh(\sqrt{\omega}x), \\ w_{II}(x) &= c_5 \cos(\sqrt{\omega}x) + c_6 \sin(\sqrt{\omega}x) + c_7 \cosh(\sqrt{\omega}x) + c_8 \sinh(\sqrt{\omega}x). \end{aligned} \quad (63)$$

The two boundary conditions on each end,  $x = 0, 1$  and the four matching conditions at  $x = y$  give eight equations in the eight unknown  $c_i$ 's,  $i \in [1, 8]$ . The system for the  $c_i$ 's is given by

$$A \begin{bmatrix} c_1 \\ c_2 \\ c_3 \\ c_4 \\ c_5 \\ c_6 \\ c_7 \\ c_8 \end{bmatrix} = \begin{bmatrix} 0 \\ 0 \\ 0 \\ 0 \\ 0 \\ 0 \\ 0 \\ \frac{F}{\omega^{3/2}} \end{bmatrix} \quad \text{where} \quad (64)$$

$$A = \begin{bmatrix} 1 & 0 & 1 & 0 & 0 & 0 & 0 & 0 \\ 0 & 1 & 0 & 1 & 0 & 0 & 0 & 0 \\ 0 & 0 & 0 & 0 & c(\sqrt{\omega}) & s(\sqrt{\omega}) & ch(\sqrt{\omega}) & sh(\sqrt{\omega}) \\ 0 & 0 & 0 & 0 & -s(\sqrt{\omega}) & c(\sqrt{\omega}) & sh(\sqrt{\omega}) & ch(\sqrt{\omega}) \\ c(\sqrt{\omega}y) & s(\sqrt{\omega}y) & ch(\sqrt{\omega}y) & sh(\sqrt{\omega}y) & -c(\sqrt{\omega}y) & -s(\sqrt{\omega}y) & -ch(\sqrt{\omega}y) & -sh(\sqrt{\omega}y) \\ -s(\sqrt{\omega}y) & c(\sqrt{\omega}y) & sh(\sqrt{\omega}y) & ch(\sqrt{\omega}y) & s(\sqrt{\omega}y) & -c(\sqrt{\omega}y) & -sh(\sqrt{\omega}y) & -ch(\sqrt{\omega}y) \\ -c(\sqrt{\omega}y) & -s(\sqrt{\omega}y) & ch(\sqrt{\omega}y) & sh(\sqrt{\omega}y) & c(\sqrt{\omega}y) & s(\sqrt{\omega}y) & -ch(\sqrt{\omega}y) & -sh(\sqrt{\omega}y) \\ s(\sqrt{\omega}y) & -c(\sqrt{\omega}y) & sh(\sqrt{\omega}y) & ch(\sqrt{\omega}y) & -s(\sqrt{\omega}y) & c(\sqrt{\omega}y) & -sh(\sqrt{\omega}y) & -ch(\sqrt{\omega}y) \end{bmatrix}.$$

For compactness,  $c, s, ch$  and  $sh$  represent  $\cos, \sin, \cosh$  and  $\sinh$ , respectively. Equation 64 may be solved for  $c_i$  in closed form. While the solution is not very complex, it is lengthy and will be omitted here. Once the  $c_i$ 's are obtained, the solution for the displacement of the beam given a point force anywhere along the beam is known analytically from Equation 63. Therefore, we have derived the Green's function,  $K(x, y)$  for the EB-beam in closed form, where

$$K(x, y) = \begin{cases} w_I(x; y) & \text{for } 0 \leq x \leq y \\ w_{II}(x; y) & \text{for } y \leq x \leq 1 \end{cases}. \quad (65)$$

We use the above Green's function as a test platform analysis of the wavelet transform.

# Transducer Placement for Broadband Active Vibration Control Using a Novel Multidimensional QR Factorization

Larry P. Heck  
SRI International  
Menlo Park, CA 94025

Koorosh Naghshineh  
Western Michigan University  
Kalamazoo, MI 49008

Julia A. Olkin  
SRI International  
Menlo Park, CA 94025

## Abstract

This paper advances the state of the art in the selection of minimal configurations of sensors and actuators for active vibration control with smart structures. The method extends previous transducer selection work by (1) presenting a unified treatment of the selection and placement of large numbers of both sensors and actuators in a smart structure, (2) developing computationally efficient techniques to select the best sensor-actuator pairs for multiple *unknown* force disturbances exciting the structure, (3) selecting the best sensors and actuators over multiple frequencies, and (4) providing bounds on the performance of the transducer selection algorithms. The approach is based on a novel, multidimensional extension of the Householder QR factorization algorithm applied to the frequency response matrices that define the vibration control problem. The key features of the algorithm are its very low computational complexity, and a computable bound that can be used to predict whether the transducer selection algorithm will yield an optimal configuration *before* completing the search. Optimal configurations will result from the selection method when the bound is tight, which is the case for many practical vibration control problems. This paper presents the development of the method, as well as its application in active vibration control of a plate.

## 1 INTRODUCTION

Active vibration control represents the state of the art in reducing unwanted vibrations in structures. A current focus of research in the area is the development of smart materials that can automatically sense and then control vibrations induced from external disturbances. Smart materials for vibration control applications typically consist of embedded sensors, actuators, communication channels, and processors that have been programmed to implement the prescribed control law with the available transducers. However, current control algorithms cannot effectively deal with large system configurations (many sensors and actuators resulting in too many interconnections). Thus, subsets of transducers are often employed to achieve the desired control. Many of these presume the existence of a control configuration (i.e., layout of the sensors and actuators and the interconnections between them) or use ad-hoc methods to specify one, and focus instead on the design of the best control law. This is in spite of the fact that the complexity and performance of a control system are largely determined by the underlying control configuration (Nett and Spang, 1987).

Recent work in transducer selection algorithms can be broadly grouped into two approaches. The first approach assumes that permissible transducer locations are a continuous function in spatial location. Approaches to solve this problem utilize numerical optimization methods where the transducer locations are included as optimization parameters (Chen et al., 1991; Skelton and DeLorenzo, 1983; Wang et al., 1991). In general, these methods have high computational complexity, and, as a result, have been limited to small-scale transducer selection problems, focusing on either actuator or sensor selection (but not both). Specifically, the methods have been applied to problems of selecting tens of transducers at a single frequency.

The second transducer selection approach treats the problem where only a fixed (finite) number of transducer locations are permissible. Approaches to solve this discrete selection problem have focused on the use of heuristic search methods to treat the combinatorial explosion of candidate transducer configurations.

Work in this area includes efforts by Snyder and Hansen (1990). In their paper, the authors focus on the sensor selection problem, and present an efficient least squares technique to evaluate the performance of each sensor configuration. However, the paper does not address the problem of efficiently searching through all combinations and instead employs exhaustive search. As a result, the approach was limited to sensor selection only, at a single frequency. Ruckman and Fuller (1993) extended the work by Snyder and Hansen by focusing on selecting actuators (instead of sensors) and suggesting the use of the general body of subset selection methods. The subset selection methods include sequential search methods (e.g., forward and backward selection), which are computationally efficient but can yield unpredictably poor results. Finally, work by Baek and Elliott (1995) employed a class of heuristic search methods known as natural algorithms for the discrete transducer selection problem. The complexity of the search methods (simulated annealing and genetic algorithms) is much more efficient than exhaustive search, but significantly higher than the sequential search methods. While the methods provide a useful alternative to the sequential search methods (outperforming them in some cases), the computational complexity of the methods restrict their use to small-scale transducer selection problems.

This paper presents a new discrete transducer selection method for designing active vibration control configurations. First, the method extends previous transducer selection work by presenting a unified treatment of the selection and placement of large numbers of both sensors and actuators in a smart structure. Second, the new method has a very low computational complexity (lower than sequential forward selection) making it useful for very large-scale sensor and actuator selection problems (thousands of sensor-actuator pairs). Third, while all the approaches described above choose transducers assuming knowledge of the location of the excitation forces on the structure (and often limit the excitation to a point force), the method described in this paper does not require this knowledge. In this way, the best transducer locations can still be selected for applications where the locations of the disturbing forces are not known during the design of the transducer configuration. Fourth, the method presented here chooses the best actuators over multiple frequencies. Finally, the paper presents a computable bound that can be used to predict whether the transducer selection algorithm will yield an optimal configuration *before* completing the search. Optimal configurations will result from the selection method when the bound is tight, which is the case for many practical vibration control problems.

This paper is organized as follows. The next section briefly defines the vibration control problem and specifies measures of performance that the control law uses. Section 3 formally defines the transducer selection problem in the context of this control law and proceeds to describe the new transducer selection approach. We also describe the complexity of the various selection methods, showing that the multidimensional QR algorithm is computationally more efficient than the other leading selection algorithms (including sequential forward selection). Finally, Section 4 presents results from application of this approach to a model of a smart plate (i.e., with embedded sensors and actuators).

## 2 VIBRATION CONTROL PROBLEM

In recent years, a variety of approaches have been developed for structural vibration control. A common requirement of these approaches is knowledge of transfer functions relating disturbances, sensors, and actuators to each other and to the areas on the structure that are to be controlled. Knowledge of the transfer functions can be achieved through measurements (i.e., on-line system identification), or through the use of structural models (e.g., finite element models). For a broad class of structures, the transfer functions can be described by a set of linear time invariant (LTI) differential equations. The *state-space* form is a popular compact representation that writes these equations in first-order form, i.e.,

$$\dot{\mathbf{x}} = \mathbf{J}\mathbf{x} + \mathbf{K}\mathbf{u} \quad (1)$$

$$\mathbf{y} = \mathbf{L}\mathbf{x} + \mathbf{M}\mathbf{u} \quad (2)$$

where  $\mathbf{J}$ ,  $\mathbf{K}$ ,  $\mathbf{L}$ , and  $\mathbf{M}$  are state matrix variables,  $\mathbf{u}$  is a vector formed by stacking the  $N_d$  disturbances and  $N_a$  actuator control inputs,  $\dot{\mathbf{x}}$  is an element state vector of first and second derivative terms, and  $\mathbf{y}$  is a



vector of  $N_s$  sensor outputs.

Taking the Fourier transform of the state-space system in Eq. (2) yields an equivalent representation in terms of the frequency response matrix or plant  $H(\omega)$ :

$$Y(\omega) = H(\omega)U(\omega), \quad (3)$$

where

$$H(\omega) = L(j\omega I - J)^{-1}K + M. \quad (4)$$

The frequency response matrix can be divided into four submatrices  $E$ ,  $A$ ,  $S$ , and  $C$ :

$$H(\omega) = \begin{bmatrix} E(\omega) & A(\omega) \\ S(\omega) & C(\omega) \end{bmatrix}, \quad (5)$$

where  $E \in \mathbb{C}^{m \times n}$  is the complex disturbance transfer matrix that relates spatially distributed forces (or pressures) at the disturbance source to spatially distributed displacements (or velocities, accelerations) in the desired vibration control zone (structural locations where minimal vibrations are desired);  $A \in \mathbb{C}^{m \times k}$  is the complex actuator transfer matrix relating control inputs (e.g., voltages) for all  $k$  candidate actuators to displacements in the desired control zone;  $S \in \mathbb{C}^{l \times n}$  is the sensor transfer matrix relating spatially distributed forces at the disturbance source to  $l$  measured normal displacements at the candidate sensor locations on the vibrating structure; and  $C \in \mathbb{C}^{l \times k}$  is the feedback coupling between the actuators and the sensors.

Figure 1 shows a block diagram of the vibration control problem. The responses from the disturbance to the sensors,  $S$ , are sent to the *compensator*  $W$ . The outputs,  $WS$ , are sent through the actuators,  $A$ , to the vibration control zone. In this particular control implementation, a feedforward neutralization filter,  $N$ , is used to "neutralize" the feedback coupling,  $C$ , between the actuators and sensors. This technique is called  $Q$ -parameterization, which has been used successfully in vibration control problems to simplify control design (Flamm et al., 1995). Thus,  $AWS$  is an estimate of the vibrations that reach the control regions directly, denoted by  $E$ . The problem, then, is to find a causal compensator,  $W$ , that minimizes the expression

$$\min_W \sum_{\omega=\omega_l}^{\omega_h} \|E - AWS\|_2^2 \quad \text{subject to} \quad \sum_{\omega=\omega_l}^{\omega_h} \|WS\|_2^2 \leq c, \quad (6)$$

where  $\omega_l$  and  $\omega_h$  are the low and high cutoff frequencies of the control bandwidth, respectively, and  $c$  is a scalar specified by the designer. The constraints in this problem are to ensure that the controller is physically realizable, i.e., that the energy in the actuator inputs,  $WS$ , does not saturate the actuators, and that the compensator is causal.

Methods currently exist to solve the control problem in Eq. (6). An efficient time-domain method for vibration and noise control problems that uses a *conjugate-gradient* minimization approach to find finite-impulse response (FIR) controllers is described by Flamm et al. (1995). The system, developed by Olkin et al. (1994), has been used to design multiple-input/multiple-output controllers for broadband noise and vibration control with large spatial extent.

### 3 TRANSDUCER SELECTION

Referring again to Figure 1, the choice of the actuators will change the size and nature of the  $S$  and  $A$  frequency response matrices. Practical limitations on the number and placement of transducers often means that vibrations in the desired control zone and disturbance forces cannot be directly measured, nor can the forces be exactly reproduced. Satisfaction of the control objective will therefore depend on the ability of the transducers to estimate and then manipulate these vibrations at the desired control zones.

### 3.1 Mathematical formulation

For the transducer selection problem, the modified control objective using reduced numbers of actuators (Heck and Naghshineh, 1994) is given as

$$\min_{W, \Pi_a, \Pi_s} \sum_{\omega=\omega_l}^{\omega_h} \|E - A \Pi_a W \Pi_s S\|_2^2 \quad \text{subject to} \quad \sum_{\omega=\omega_l}^{\omega_h} \|W \Pi_s S\|_2^2 \leq c, \quad (7)$$

with the minimization completed over two additional parameters  $\Pi_a \in I^{m \times N_a}$  ( $N_a < m$ ) and  $\Pi_s \in I^{N_s \times n}$  ( $N_s < n$ ), where  $I^{i \times j}$  is the set of all  $i \times j$  binary-valued matrices. The parameters are called *actuator and sensor selectors*, respectively. The columns of  $\Pi_a$  and rows of  $\Pi_s$  are unit basis vectors corresponding to actuator and sensor locations (e.g., unit basis vector  $\mathbf{u}_3 = [0 \ 0 \ 1 \ 0 \ 0]^T$  corresponds to the third transducer position). An actuator selector matrix given as

$$\Pi_a = \begin{bmatrix} 1 & 0 \\ 0 & 0 \\ 0 & 1 \end{bmatrix} \quad (8)$$

would select the first and third actuator responses (columns) of  $A$ .

### 3.2 Key issues

The problem in Eq. (7) is difficult to solve directly because the quadratic cost function is non-differentiable. This arises because of the discontinuous nature of the selector matrices: either a transducer is selected, or it is not. As a result, the problem cannot be solved through direct extensions of the gradient-based optimization methods (such as the conjugate gradient method), and instead has been addressed through direct enumeration (search) methods. The complexity of the enumeration method is approximately the complexity of a complete controller design and performance assessment for one configuration multiplied by the number of possible transducer configurations. The number of possible configurations grows extremely rapidly as the complexity of the system increases.

For the transducer selection problem, given  $m$  candidate sensors and  $n$  candidate actuators, the number of distinct subsystems with  $k$  sensors and  $l$  actuators will be

$$\binom{m}{k} \binom{n}{l} \triangleq \frac{m!}{k!(m-k)!} \frac{n!}{l!(n-l)!}. \quad (9)$$

The total number of distinct subsystems will be

$$\sum_{k=1}^m \sum_{l=1}^n \binom{m}{k} \binom{n}{l}, \quad (10)$$

where each subsystem corresponds to a selected subset of the candidate transducers.

Even for modest-size problems, the number of candidate transducer configurations in Eq. (10) becomes exceedingly large. For example, the number of possible configurations or subsystems in a system with 40 sensors and 40 actuators is approximately  $1.1 \times 10^{23}$  (assuming only subsystems with equal numbers of sensors and actuators are considered). To put this into perspective, if each configuration could be evaluated in 1 second (i.e., a complete control design with the compensator computed), then it would take over  $3.4 \times 10^{13}$  centuries to evaluate every possible configuration! As a result of the large numbers of possible transducer configurations, a practical method for transducer selection will necessarily consist of suboptimal, but highly efficient measures to assess controller quality along with fast enumeration algorithms.

### 3.3 Transducer selection approach: single frequency

The approach to transducer selection presented in this section employs computationally efficient heuristic methods that avoid the high combinatorics described above. The approach consists of two main steps. First, the problem shown in Eq. (7) is broken down into smaller, more tractable problems. Then, after the large set of candidate transducer configurations is reduced to a small number, full controller designs are completed. In the first step, the approach seeks submatrices of  $A$  and  $S$  selected by  $\Pi_a$  and  $\Pi_s$ , that *extract the non-redundant* components of the original matrices. In addition, it is assumed that the residual error of the controller with these full matrices can be made small, i.e.,  $E \approx AWS$  at all frequencies. Beginning with the single frequency case, the approach approximates the controller with selected transducers such that  $A\Pi_a W \Pi_s S \approx AWS$ . To achieve this, a subspace distance measure,  $D_s$ , can be employed to quantify the difference between the original and candidate submatrices. A popular measure in the statistics, numerical analysis, and signal processing literature (Golub and Van Loan, 1989) is given as

$$D_s(A, A\Pi_a) = \sin \Theta(\mathcal{R}(A), \mathcal{R}(A\Pi_a)) \quad (11)$$

$$D_s(S, \Pi_s S) = \sin \Theta(\mathcal{R}(S^T), \mathcal{R}((\Pi_s S)^T)), \quad (12)$$

where  $\mathcal{R}$  denotes range space, and  $\sin \Theta$  is the sine of the largest *principal angle* between the range subspaces of the transfer function matrices. The largest principal angle between two subspaces  $F$  and  $G$  is the angle between the unit vector in  $F$  whose orthogonal projection onto  $G$  gives the largest residual. The sine of the largest principal angle is equivalent to the 2-norm of the difference (residual) between the orthogonal projections onto the range spaces of the matrices.

Since the largest principal angle corresponds to a worst-case residual, it can be argued that the selector matrices should be chosen to make the distance measures in Eqs. (11) and (12) as small as possible. However, for the vibration control problem, such an approach could lead to large actuator inputs, which would violate the constraints in Eq. (7). To see this, consider the following example (Golub and Van Loan, 1989). Let  $S, \Pi_s = I$  in Eq. (7), where  $I$  is the identity matrix. Also, let  $\omega = \omega_q$  so that the minimization is completed over a single frequency. We can rewrite the minimization problem as

$$\min_{W, \Pi_a} \|E - A\Pi_a W\|_2^2 \quad \text{subject to } \|W\|_2^2 \leq c. \quad (13)$$

If the goal is to find the two best actuators, and

$$A = \begin{bmatrix} 1 & 1 & 0 \\ 1 & 1+\epsilon & 1 \\ 0 & 0 & 1 \end{bmatrix}, \quad E = \begin{bmatrix} 1 \\ -1 \\ 0 \end{bmatrix}, \quad (14)$$

then choosing the first two actuators (first two columns of  $A$ ) gives the residual  $\|E - A\Pi_a\|_2^2 = 0$ , but  $\|(A\Pi_a)^+ E\|_2^2 = \|\mathbf{W}_{LS}\|_2^2 = \mathcal{O}(1/\epsilon)$ , where  $Q^+$  is the Moore-Penrose pseudoinverse operator (Stewart, 1984). As  $\epsilon$  gets smaller, the actuator weights will grow and eventually violate the constraint in Eq. (13). On the other hand, the other two possible subsets of actuators will lead to small weight norms, but with a much worse residual.

This example highlights the tradeoff that exists between choosing an independent set of actuators and choosing a set that minimizes the residual control error. A similar tradeoff occurs in the use of *subset selection* methods (Golub et al., 1976) to solve general rank-deficient least-squares problems. A solution developed for this problem uses a Householder QR with column-pivoting factorization. For the transducer selection problem, the factorization can be used to efficiently find an independent set of actuators and sensors. In addition, if the proper number of transducers is selected, the residuals in Eq. (7) can be made small.

The Householder QR algorithm can be described as follows. Let  $G \in \mathbb{C}^{m \times n}$  matrix be representative of the  $A$  and  $S$  matrices in Eqs. (11) and (12). The QR decomposition of  $G$  can be written as

$$\begin{aligned} G &= QR \\ &= Q \begin{pmatrix} R_{11} & R_{12} \\ 0 & R_{22} \end{pmatrix}, \end{aligned}$$

where  $Q \in \mathbb{R}^{m \times m}$  has orthonormal columns ( $Q^T Q = I$ ),  $R_{11}$  is a  $k \times k$  matrix with a condition number approximately equal to  $\sigma_1/\sigma_k$ ,  $\|R_{22}\|$  is of the order  $\sigma_{k+1}$ , and  $k$  is the rank of  $G$ . Pivoting (or permuting) the columns of the QR factorization can be used to make  $R_{22}$  small. For a rank-deficient matrix with  $r = \text{rank}(G)$ , column pivoting can yield

$$Q^T GP = \begin{bmatrix} R_{11} & R_{12} \\ 0 & 0 \end{bmatrix}, \quad (15)$$

where  $R_{11} \in C^{r \times r}$  is upper triangular and nonsingular, and  $R_{12} \in C^{n-r \times r}$ . With the column partitionings  $GP = [g_{p_1}, g_{p_2}, \dots, g_{p_n}]$  and  $Q = [q_1, q_2, \dots, q_m]$ , and  $r_{ij}$  denoting the  $(i, j)$ -th element of  $R$ , we have

$$g_{p_k} = \sum_{i=1}^{\min\{r, k\}} r_{ik} q_i \in \text{span}\{q_1, q_2, \dots, q_r\} \quad \text{for } k = 1 : n. \quad (16)$$

This implies that the  $\text{range}(G) = \text{span}\{q_1, \dots, q_r\} = \text{span}\{g_{p_1}, \dots, g_{p_r}\}$ . In other words, column pivoting can be used to find a subset of columns in a rank-deficient matrix that has the same range space as the original matrix, making the principal angles between the original and submatrix go to zero. In addition, the Householder procedure described in Golub and Van Loan (1989) ensures that the resulting submatrix of  $G$  is also well-conditioned (i.e., that the columns are sufficiently independent). Selecting actuators, for example, with this procedure (columns of  $A$  in Eq. (7)) will make the distance measure in Eq. (11) go to zero and yield a subset with the same *control authority* as the original, densely packed set of actuators.

In most vibration control problems of interest, the rank of the  $A$  and  $S^T$  matrices will not be exactly zero. Rather, because of numerical approximations, the rank can only be specified in terms of a threshold on singular values, called the *numerical rank* (Stewart, 1984). A consequence is that nonzero differences will exist between the range spaces of the original and selected submatrices. As a result, a method is required to determine the circumstances under which the differences between the range spaces is small. A useful bound (Golub and Van Loan, 1989) can be determined that specifies these circumstances, i.e.,

$$\sin \Theta(A, A\Pi_a) \leq \sigma_{r+1} \|R_{11}^{-1}\| \quad (17)$$

$$\sin \Theta(S^T, (S\Pi_s)^T) \leq \sigma_{s+1} \|R_{11}^{-1}\|, \quad (18)$$

where  $\sigma_{r+1}$  and  $\sigma_{s+1}$  are the  $(r+1)$ st and  $(s+1)$ st largest singular values of  $A$  and  $S$ , respectively, and the submatrix  $R_{11}$  (this in general will be a different matrix for  $A$  and  $S$ ) in the QR factorizations is guaranteed to be of the order  $\sigma_r^{-1}$  for  $A$  and  $\sigma_s^{-1}$  for  $S$ . These bounds show a sufficient condition for small errors; i.e., if there exists a large gap in successive singular values, called the *spectral gap*, then the error will be small. For transducer selection, these bounds provide a useful criterion for the optimality of a given configuration. Also, they give a direct correspondence between the numerical rank of the frequency response matrices and the number of required transducers; e.g., if the numerical rank of the actuator frequency response matrix is  $k$ , then  $k$  actuators are required.

### 3.4 Broadband extension

The goal for the broadband transducer selection problem is to minimize the expression in Eq. (7) with a single configuration over all frequencies of interest. For the broadband case, we extend the Householder procedure to compute factorizations over multiple matrices. The approach is as follows. Assume for some  $k$  and frequency  $\omega_i$  that we have computed Householder matrices  $H_1, \dots, H_{k-1}$  and permutations  $P_1, \dots, P_{k-1}$  such that

$$(H_{k-1}(\omega_i) \cdots H_1(\omega_i))G(\omega_i)(P_1(\omega_i) \cdots P_{k-1}(\omega_i)) = R^{k-1}(\omega_i) \quad (19)$$

$$= \begin{bmatrix} R_{11}^{(k-1)}(\omega_i) & R_{12}^{(k-1)}(\omega_i) \\ 0 & R_{22}^{(k-1)}(\omega_i) \end{bmatrix}, \quad (20)$$

where  $R_{11}^{(k-1)}(\omega_i) \in C^{(k-1) \times (k-1)}$ ,  $R_{12}^{(k-1)}(\omega_i) \in C^{(n-k+1) \times (k-1)}$ , and  $R_{22}^{(k-1)}(\omega_i) \in C^{(n-k+1) \times (n-k+1)}$ . The single-frequency Householder method moves the column of  $G$  corresponding to the largest column in  $R_{22}(\omega_i)$  to the  $k$ th column position (the lead position in the  $R_{22}(\omega_i)$  matrix), where largest is specified by the selection of a vector norm. The column exchanges are accomplished with the permutation matrix  $P(\omega_i)$ . This is followed by a left multiplication by a Householder matrix that zeroes all the subdiagonal components of the largest  $R_{22}(\omega_i)$  column vector. The procedure stops when  $k - 1 = \text{rank}(G(\omega_i))$ .

For the broadband case (multiple  $G$  matrices), instead of permuting a  $G(\omega_i)$  based on the column with the largest vector norm in  $R_{22}^{(k-1)}$ , we permute  $G(\omega_1), \dots, G(\omega_n)$  based on one of eight possible performance measures on the matrix consisting of a column from each  $R_{22}(\omega_1), \dots, R_{22}(\omega_n)$  matrix.

These performance measures, discussed and analyzed in more detail in Olkin, Heck, and Naghshineh (1996), can be selected depending on the application. The first four performance measures are the three induced matrix norms,  $l_1$ ,  $l_2$  and  $l_\infty$  and the Frobenius norm. The fifth performance measure chooses the smallest singular value of each actuator which helps minimize the effect of deep nulls in an actuator frequency response, which can lead to nonrobust control designs with poor performance. The sixth measure chooses the actuator response with the largest average value over all frequencies and response locations. The seventh measure is the ratio of the minimum to maximum actuator response over frequency, reflecting the fact that flatter actuator frequency responses are often desirable due to noise control robustness and performance considerations. The last performance measure attempts to minimize the effect of spatial nulls by choosing the maximum row sum of the actuator matrix.

As was the case with a single matrix, this permutation step is followed by left multiplying each  $G(\omega_1), \dots, G(\omega_n)$  with the corresponding Householder matrices that will zero the subdiagonal components of the selected columns for each  $R_{22}(\omega_1), \dots, R_{22}(\omega_n)$  matrix. Figure 2 illustrates this multidimensional broadband extension of the Householder QR factorization with column pivoting. Note that  $P$  is not a function of frequency; hence this matrix of ones and zeros is the same for each frequency.

For the broadband case, the error bounds in Eqs. (17) and (18) hold for each frequency, i.e.,

$$\begin{aligned} \sin \Theta(A(\omega_1), A(\omega_1)\Pi_a) &\leq \sigma_{r+1}(\omega_1) \| R_{11}(\omega_1)^{-1} \| \\ \sin \Theta(A(\omega_2), A(\omega_2)\Pi_a) &\leq \sigma_{r+1}(\omega_2) \| R_{11}(\omega_2)^{-1} \| \\ &\vdots \\ \sin \Theta(A(\omega_n), A(\omega_n)\Pi_a) &\leq \sigma_{r+1}(\omega_n) \| R_{11}(\omega_n)^{-1} \| \end{aligned}$$

and

$$\begin{aligned} \sin \Theta(S(\omega_1)^T, (S(\omega_1)\Pi_s)^T) &\leq \sigma_{s+1}(\omega_1) \| R_{11}(\omega_1)^{-1} \| \\ \sin \Theta(S(\omega_2)^T, (S(\omega_2)\Pi_s)^T) &\leq \sigma_{s+1}(\omega_2) \| R_{11}(\omega_2)^{-1} \| \\ &\vdots \\ \sin \Theta(S(\omega_n)^T, (S(\omega_n)\Pi_s)^T) &\leq \sigma_{s+1}(\omega_n) \| R_{11}(\omega_n)^{-1} \| . \end{aligned}$$

The bounds hold for each frequency because the derivation of the bounds does not depend upon the specific properties of the QR factorization. Rather, the proof holds for a general  $R_{11}$  matrix. However, the quality of the bound may be adversely affected if  $\| R_{11}^{-1} \|$  is not on the order of  $\sigma_k^{-1}$ .

### 3.5 Computational complexity of approach

The algorithm for implementing the transducer selection approach described above is computationally efficient and, as a result, can be used for very large-scale problems involving hundreds to thousands of sensors and actuators. Specifically, suppose we are choosing  $k$  actuators out of  $N_d$  total actuators, with  $N_e$  error sensors, over  $N_f$  frequencies. Each of the following transducer selection methods requires some sort of computation of the residual of the active vibration control system. Let  $\mathcal{O}(\text{residual})_k$  represent the flop count

for computing the system residual with  $k$  actuators. Then Table 1 gives a general complexity overview of some actuator selection methods, and the dominating term by way of easy comparison. The methods are (i) Exhaustive Search, in which all combinations of  $k$  actuators are considered, (ii) Best  $k$ , in which each actuator is evaluated individually and the Best  $k$  are chosen, (iii) sequential forward selection, in which actuators are added to the chosen set based on which new actuator will behave the best with those already chosen, and finally, (iv) Multidimensional QR, the algorithm presented in this paper. Choosing  $k$  out of  $N_s$  sensors yields similar relative complexity counts as in Table 1, with Multidimensional QR still more computational efficient than the SFS method. For brevity, we include results for the actuators only.

Table 1: Algorithm Complexity For Choosing  $k$  out of  $N_d$  Actuators

Method	General Complexity	Dominating Term
Exhaustive Search	$N_f \frac{N_d!}{k!(N_d-k)!} \mathcal{O}(\text{residual})_k$	$N_f \frac{N_d!}{k!(N_d-k)!} (6N_e k^2 + 20k^3)$
Multidim. QR	$\sum_{i=1}^k i \mathcal{O}(\text{column-selection}) + N_f \mathcal{O}(\text{Householder transform})$	$k^2(N_f N_e^2 + N_e^3) + k N_f N_e^3 + N_f N_e$
Seq. Forward Sel.	$\sum_{i=1}^k \{(N_d - i + 1) \mathcal{O}(\text{residual})_i\}$	$k^3 N_f N_d N_e + k^4 N_f N_d - k^5 N_f$
Best $k$	$N_d N_f \mathcal{O}(\text{residual})_1$	$7 N_f N_d N_e$

It can be difficult to compare the dominating terms, so as way of example, consider a system with 40 possible actuators in which only 20 can be kept. Assume there are 20 error sensors measuring the actuator responses over 300 frequencies. Then the complexity for these four methods are shown in Table 2, printed in order of optimality of solution.

Table 2: Example Complexity Comparison

Method	Complexity
Exhaustive Search	6.9e19
Sequential Forward Selection	3.8e9
Multidimensional QR	9.9e7
Best $k$	1.7e6

Notice that the Multidimensional QR algorithm is more efficient than sequential forward selection, and comparable with Best K. In addition, the method is guaranteed to perform as well or better than both SFS and Best K. As will be demonstrated in the next section, the efficiency of this procedure enables practical transducer selection for large-scale problems.

## 4 NUMERICAL RESULTS

The methods described in the previous section were applied to the problem of controlling vibrations on a smart plate model (embedded sensors and actuators). The SPICES consortium's solid-plate model (Flamm et al. 1995) was considered.

As shown in Figure 3, the plate is a layered composite material  $46 \times 46 \times 1.2$  cm. ( $18 \times 18 \times 0.5$  in.), connected to an infinite, rigid base on the bottom of the plate at the four corners (indicated by the black dots). The plate was excited with a point force with x, y, and z components. The force was applied to the plate through a stiff tripod (all three connections with the plate move together to simulate connectors between the plate and attached machinery). The forcing function was an impulse with flat frequency response. The first 268 natural frequencies and mode shapes of this 3858-node plate model were used in the computation of frequency response matrices (admittance) relating excitation force to displacement.

The sensor models used in this numerical experiment measure point displacements. For the sensor placement studies, 361 evenly spaced candidate sensor locations were used. The candidate locations were on a  $19 \times 19$  grid (2.5 cm=1 in. from nearest neighbor) in the middle layer (denoted by the dashed line). For the actuator placement studies, simple two-dimensional actuators were modeled and incorporated into the plate model. The actuators have length and depth (into the plate), but no width. Figure 4 shows a cross-section side view of the plate with an embedded actuator. The directional forces in the model are shown as  $\pm F$ , which produce an effective bending moment about the center of the actuator. A total of 180 candidate actuator locations were specified for the actuator selection studies. From a top view of the plate (xy projection), the actuator locations formed a checkerboard pattern, as illustrated in the right plot in Figure 3. The lines between the dots on the checkerboard pattern represent the actuators, and all horizontal and vertical lines, represented by letters in this schematic, are considered actuators. The goal of the vibration control system was to reduce the transmission of forces over 500-4000 Hz from the tripod excitation to the connectors at the four corners of the plate. Thus, the four corners of the plate model represent the vibration control zone. All control law designs used FIR implementations designed using the conjugate-gradient method described in Section 2. The FIR weights were found by solving the minimization problem in Eq. (6).

To select the sensors and actuators, the continuous, time-domain, state-space model responses were sampled and used to compute the frequency response matrices  $S$  and  $A$  in Eq. (7). The sensor and actuator selection was then performed using these matrices. Finally, the FIR controller was implemented and the controlled system responses computed.

The  $S$  matrix consisted of 361 rows (corresponding to sensor responses), and the  $A$  matrix had 180 columns (actuator responses). The broadband extension of the Householder QR with column-pivoting factorization was applied to these matrices to find the columns of  $A$  and rows of  $S$  that formed matrices with approximately the same range space as the original matrices. As described in Section 3.4, the matrix 2-norm was used by the Householder algorithm to select the columns of the response matrices. The numerical rank of the  $S$  matrix (with a threshold set @ -30 dB) was approximately 3. Based on this, three sensors were chosen. Their locations correspond to the connector points between the tripod and the plate in Figure 3. The numerical rank of the  $A$  matrix was approximately 4. The left plot in Figure 5 shows the locations of the actuators and sensors chosen by the broadband QR method. The right plot shows the uncontrolled (dashed) and controlled (solid) time-domain impulse responses for the control bandwidth at the  $x = 17$  in.,  $y = 17$  in. connector. As can be seen, this control configuration quickly reduces the vibration transmission from the tripod to the connectors. Figure 6 shows the power spectral density (psd) of the uncontrolled and controlled vibration responses for the sensor-actuator layout chosen by the multidimensional QR algorithm. The lines shown represent the root mean squared (RMS) of the values of the responses at all four feet from the x, y, and z tripod excitation. As can be seen, the controller effectively reduces the transmission power over the control bandwidth (500-4000 Hz).

To compare the QR-based designs with manually selected actuator locations, additional designs were completed, chosen to be intuitively competitive. The results are shown in Figures 7 through 10 (all cases used the QR sensor configuration). As can be seen, the performance for each design were inferior to those of the QR-based actuator configuration. Table 3 shows the in-band control performance (500-4000Hz) at each of the four feet (or corners) of the plate in dB. The three configurations of actuator placement are the QR-based configuration and the two comparison configurations shown in Figures 7 and 9. Notice that the performance at all four corners for the QR-based configuration is about the same level, whereas there is much more variation for the other two configurations, and even some enhancement.

## 5 SUMMARY

This paper has presented a computationally efficient, unifying method for broadband sensor and actuator selection. The method is based on the Householder QR with column-pivoting factorization of the system's frequency response matrices. Using the Householder algorithm, upper bounds were presented on the errors induced by selecting a subset of transducers. The bounds can be computed efficiently, as they are in terms of the singular values of the response matrices. Also, they serve as sufficient conditions for optimality of

Table 3: Performance Comparison.

Configuration	In-Band Performance (dB)			
	Corner 1	Corner 2	Corner 3	Corner 4
QR	10.9	10.9	11.4	11.4
Figure 7	6.86	-.24	.76	-.40
Figure 9	10.6	5.8	2.3	3.2

the transducer selection method, such that rank-deficient response matrices with large spectral gaps in the singular values cause the bounds in Eq. (17) and Eq. (18) to reach equality instead of inequality. Finally, the multidimensional extension of the Householder QR procedure developed in this paper provides a practical method of selecting sensors and actuators that yield effective control over a broad band of frequencies. The new method is more efficient than sequential forward selection and has an order of complexity approaching that of simply choosing the best K transducers independently. However, the new method performs as well or better than both competing algorithms. Future work will extend this method to minimize the required interconnections between the sensors and actuators.

## 6 ACKNOWLEDGEMENTS

This work was supported by ARPA Contracts MDA972-93-2-0010 and N00014-94-C-0176. The authors wish to thank the SPICES team for providing the plate model used in the numerical experiments presented here, and David Flamm, Bill Nowlin, Paul Titterton, and Ken Chou for helpful discussion related to this work.

## 7 REFERENCES

- K. Baek, S. Elliott, 1995, "Natural algorithms for choosing source locations in active control systems," *ASME J. Sound and Vib.*, vol. 186, no. 2, pp. 245-267.
- G. Chen, R. Bruno, and M. Salama, 1991, "Optimal placement of active/passive members in truss structures using simulated annealing," *AIAA Journal*, vol. 29, no. 8.
- R. Clark and C. Fuller, 1992, "Optimal placement of piezoelectric actuators and polyvinylidene fluoride error sensors in active structural acoustic control approaches," *J. Acoust. Soc. Am.*, vol. 92(3), pp. 1521-1533.
- D. Flamm, L. Heck, P. Titterton, W. Nowlin, J. Olkin, and K. Chou, 1995, "Control system design for the spices smart structure demonstrations," in *SPIE Conference on Smart Structures and Materials*, pp. 237-248.
- G. H. Golub, V. Klema, and G. W. Stewart, 1976, "Rank degeneracy and least squares problems," Tech. Rep. TR-456, Depart. of Computer Science, University of Maryland, College Park, MD.
- G. H. Golub and C. F. Van Loan, 1989, *Matrix Computations*. Baltimore: The Johns Hopkins University Press, second ed.
- L. Heck and K. Naghshineh, 1994, "Large-scale, broadband actuator selection for active noise control," in *Proceedings of Nat. Conf. in Noise Control Engineering*, (Ft. Lauderdale, FL).
- C. Nett and H. Spang, 1987, "Control structure design: A missing link in the evolution of modern control theories," in *American Control Conference*, vol. 29.
- J. A. Olkin, M. S. Freed, and P. D. Jungers, 1994, "SRI weights algorithm and performance simulation (SWAPS) code," tech. rep., SRI International.
- J. Olkin, L. Heck, and K. Naghshineh, 1996, "Automated placement of transducers for active noise control: Performance measures," in *International Conference on Acoustics, Speech, and Signal Processing*, (Atlanta, GA).
- C. Ruckman and C. Fuller, 1993 "Optimizing actuator locations in feedforward active control



systems using subset selection," in *Supplement to 2nd Conf. on Recent Advances in Active Control of Sound and Vibration*, pp. S122-S133.

K. Skelton, R.E. DeLorenzo, M.L., 1983, "Selection of noisy actuators and sensors in linear stochastic systems," *Journal of Large Scale Systems, Theory, and Applications*, vol. 4, pp. 109-136.

S. D. Snyder and C. H. Hansen, 1990, "Using multiple regression to optimize active noise control system design," in *J. of Sound and Vib.*.

G. W. Stewart, 1984, "Rank degeneracy," *SIAM J. Sci. Statist. Comput.*, vol. 5, pp. 403-413.

B. Wang, R. Burdisso, and C. Fuller, 1991, "Optimal placement of piezoelectric actuators for active control of sound radiation from elastic plates," *Proceedings of Nat. Conf. in Noise Control Engineering*, pp. 267-274.

B. Wang, 1996, "Optimal placement of microphones and piezoelectric transducer actuators for far-field sound radiation control," *J. Acoust. Soc. Am.*, vol. 99, no. 5.

## Table Legends

**Table 1:** Algorithm Complexity For Choosing  $k$  out of  $N_d$  Actuators.

**Table 2:** Example Complexity Comparison.

**Table 3:** Performance Comparison.

## Figure Legends

**Figure 1:** Block diagram of the vibration control problem. The responses from the disturbance to the sensors,  $S$ , are sent to the *compensator*  $W$ . The outputs,  $WS$ , are sent through the actuators,  $A$ , to the vibration control zone. A feedforward neutralization filter,  $N$ , is used to “neutralize” the feedback coupling,  $C$ , between the actuators and sensors.

**Figure 2:** Multidimensional Householder QR factorization with column pivoting.

**Figure 3:** The left plot shows the solid-plate model developed by the SPICES consortium. The right plot shows the pattern for the 180 candidate actuator locations embedded in the SPICES plate.

**Figure 4:** Actuator Model.

**Figure 5:** Locations of the actuators and sensors chosen by the broadband QR method (left). The uncontrolled (dashed) and the controlled (solid) time-domain impulse responses for the control bandwidth for the connector located at  $x = 17in.$ ,  $y = 17in.$  (right).

**Figure 6:** Plot of the RMS values of the uncontrolled (solid) and the controlled (dashed) responses at all four feet for the configuration chosen by the QR algorithm.

**Figure 7:** Locations of the actuators and sensors chosen by the authors for comparison to the QR method (left). The uncontrolled (dashed) and the controlled (solid) time-domain impulse responses for the control bandwidth for the connector located at  $x = 17in.$ ,  $y = 17in.$  (right).

**Figure 8:** Plot of the RMS of the uncontrolled (solid) and the controlled (dashed) responses at all four feet for the configuration chosen by the authors.

**Figure 9:** Locations of the actuators and sensors chosen by the authors for comparison to the QR method (left). The uncontrolled (dashed) and the controlled (solid) time-domain impulse responses for the control bandwidth for the connector located at  $x = 17in.$ ,  $y = 17in.$  (right).

**Figure 10:** Plot of the RMS of the uncontrolled (solid) and the controlled (dashed) responses at all four feet for the configuration chosen by the authors.

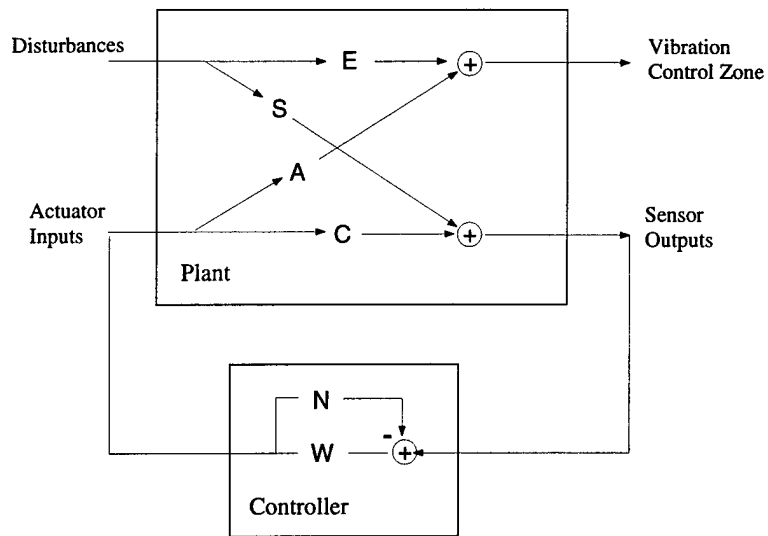


Figure 1: Block diagram of the vibration control problem. The responses from the disturbance to the sensors,  $S$ , are sent to the compensator  $W$ . The outputs,  $WS$ , are sent through the actuators,  $A$ , to the vibration control zone. A feedforward neutralization filter,  $N$ , is used to "neutralize" the feedback coupling,  $C$ , between the actuators and sensors.

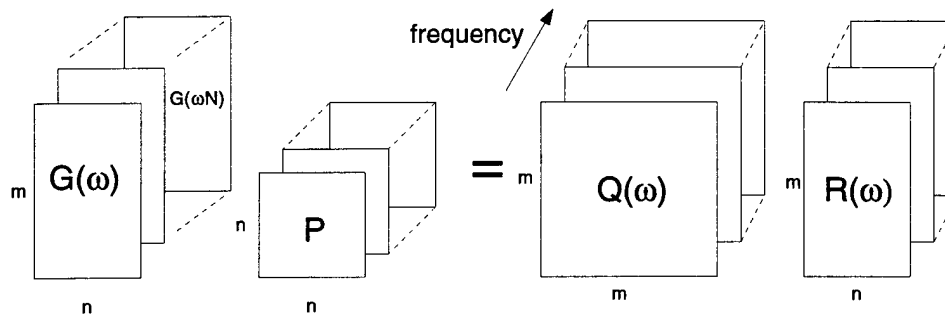


Figure 2: *Multidimensional Householder QR factorization with column pivoting.*

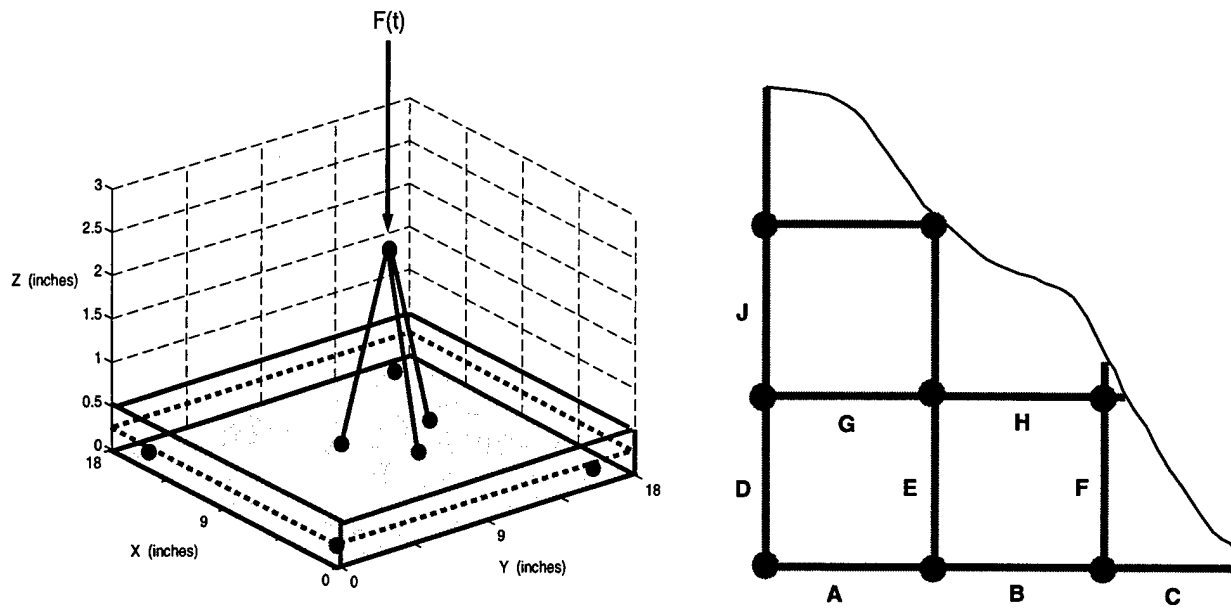


Figure 3: The left plot shows the solid-plate model developed by the SPICES consortium. The right plot shows the pattern for the 180 candidate actuator locations embedded in the SPICES plate.

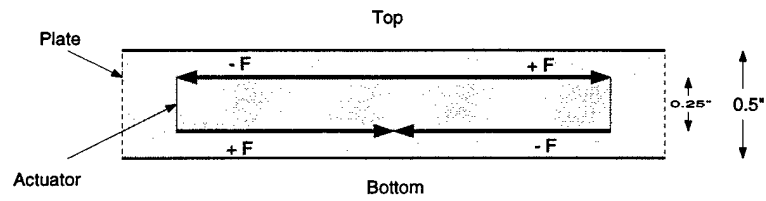


Figure 4: *Actuator Model.*

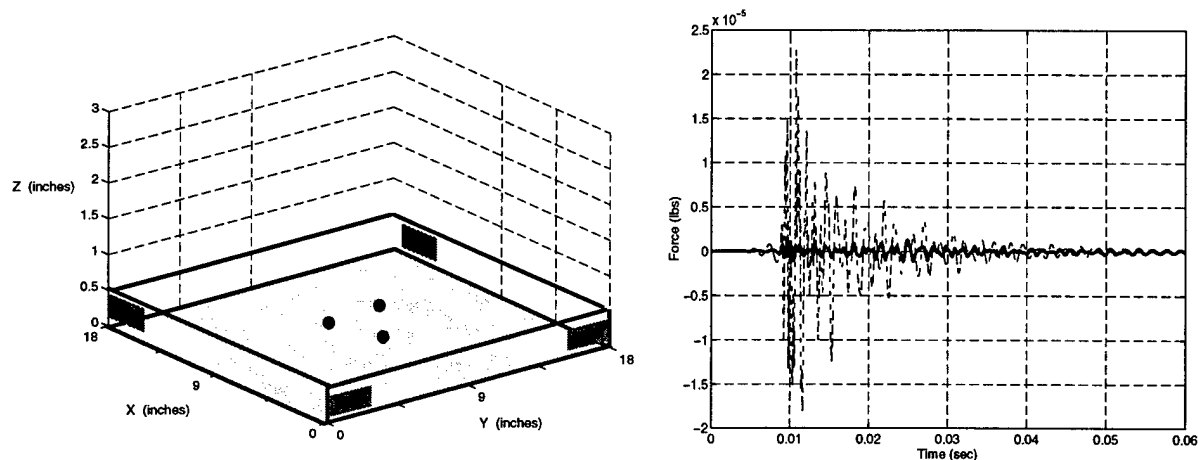


Figure 5: Locations of the actuators and sensors chosen by the broadband QR method (left). The uncontrolled (dashed) and the controlled (solid) time-domain impulse responses for the control bandwidth for the connector located at  $x = 17\text{in.}$ ,  $y = 17\text{in.}$  (right).



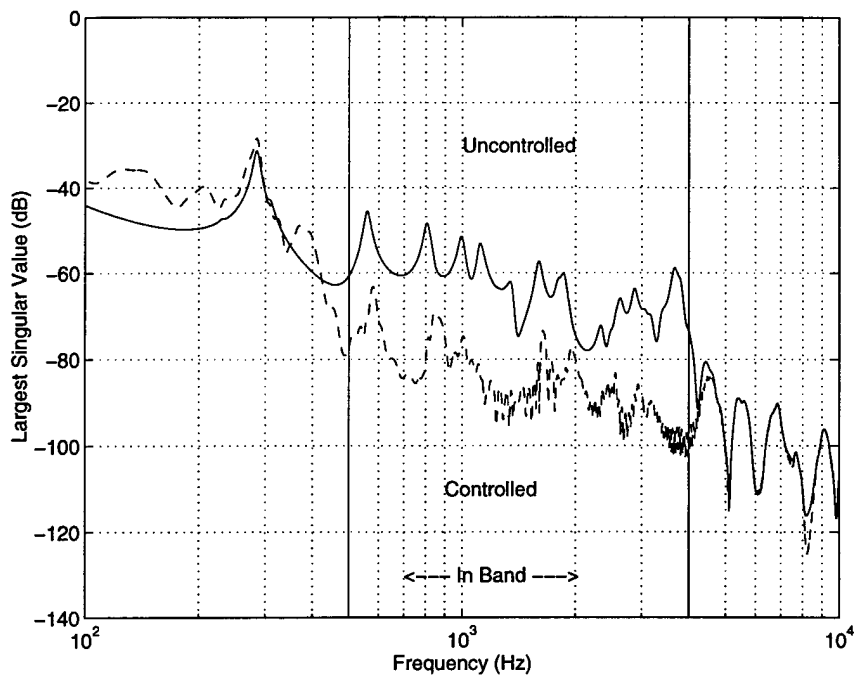


Figure 6: Plot of the largest singular values of the uncontrolled (solid) and the controlled (dashed) responses at all four feet for the configuration chosen by the QR algorithm.

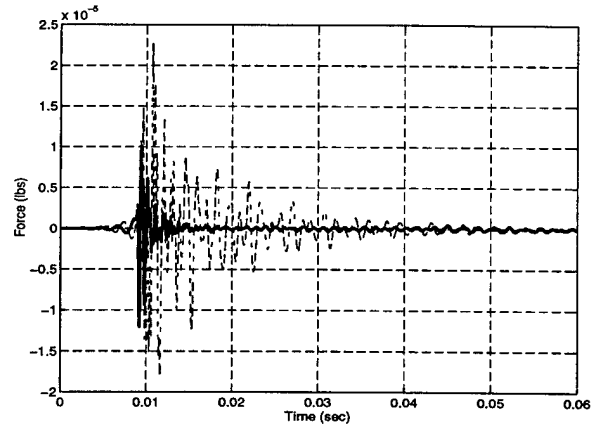
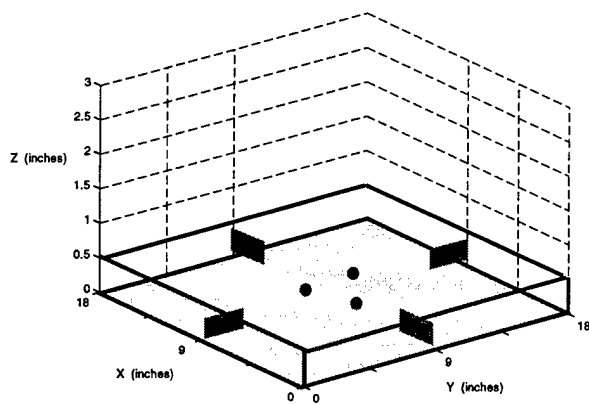


Figure 7: Locations of the actuators and sensors chosen by the authors for comparison to the QR method (left). The uncontrolled (dashed) and the controlled (solid) time-domain impulse responses for the control bandwidth for the connector located at  $x = 17\text{in.}$ ,  $y = 17\text{in.}$  (right).

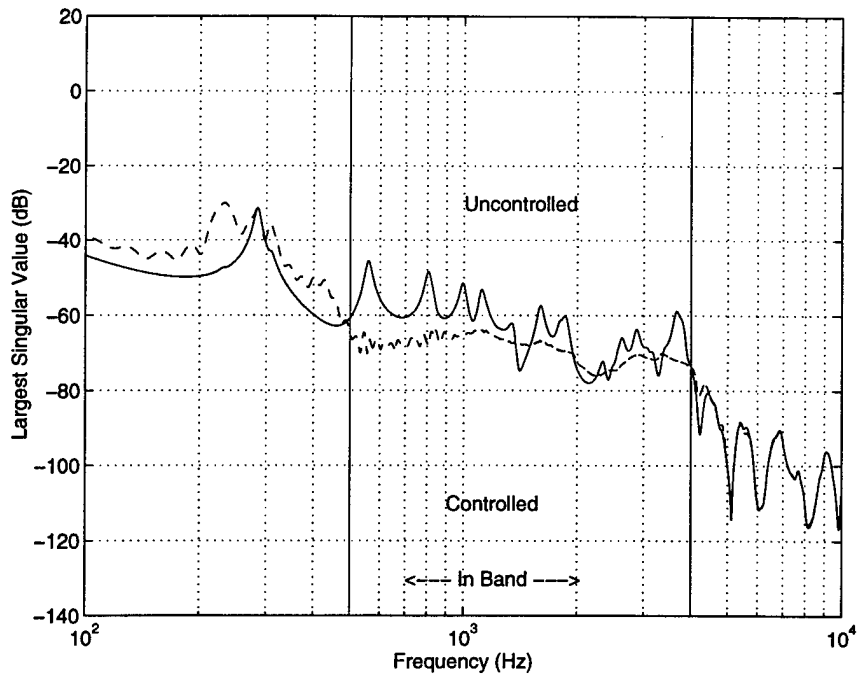


Figure 8: Plot of the largest singular values of the uncontrolled (solid) and the controlled (dashed) responses at all four feet for the configuration chosen by the authors.

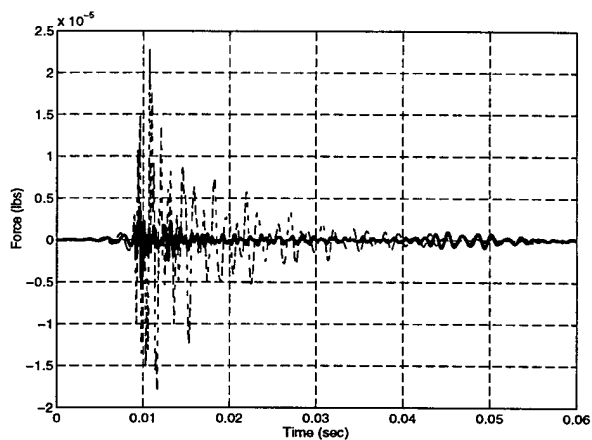
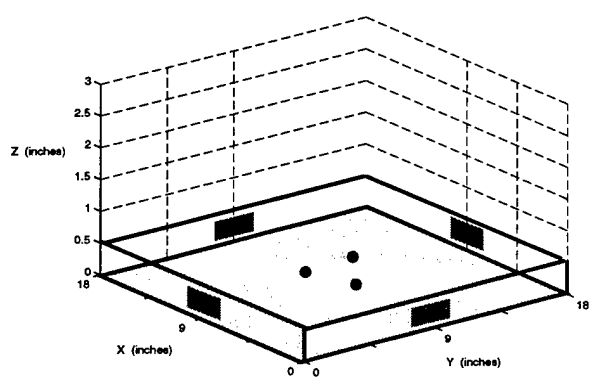


Figure 9: Locations of the actuators and sensors chosen by the authors for comparison to the QR method (left). The uncontrolled (dashed) and the controlled (solid) time-domain impulse responses for the control bandwidth for the connector located at  $x = 17\text{in.}$ ,  $y = 17\text{in.}$  (right).

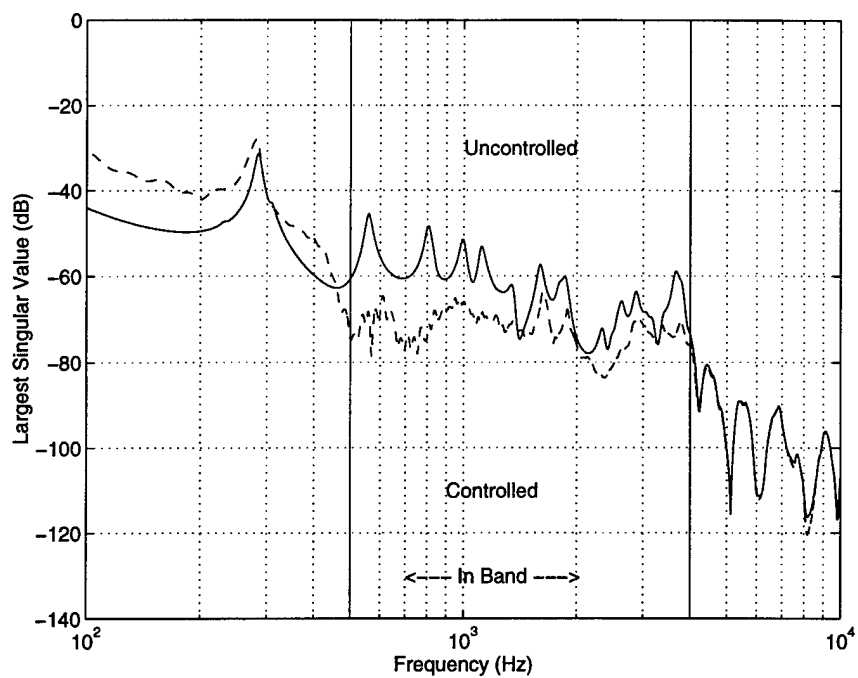


Figure 10: Plot of the largest singular values of the uncontrolled (solid) and the controlled (dashed) responses at all four feet for the configuration chosen by the authors.

# Representation of Green's Function Integral Operators Using Wavelet Transforms

Dr. Kenneth C. Chou (corresponding author)

System Technology Division

SRI International

Menlo Park, CA 94025

(415) 859-3097

(415) 859-4121 (Fax)

kcchou@sneezy.sri.com

Dr. Gary S. Guthart

Intuitive Surgical, Inc

1340 W. Middlefield Rd

Mountain View, CA 94043

(415) 237-7017

gary\_guthart@intusurg.com

## Abstract

In this paper we analyze the representation of integral operators whose kernels are Green's functions for a class of linear differential equations using wavelets with a finite number of vanishing moments. In particular, we show how wavelets can be used to generate a sparse representation of these operators. We show that the matrix associated with the discretized integral operator represented in the wavelet basis is sparse and, in particular, contains multiple bands of various widths. The particular banded structure of the wavelet representation of the operator follows from the fact that the associated Green's function is smooth away from the source point and is singular at some order; i.e., for some  $T$ , its  $T$ th derivative is discontinuous at the source point. We derive bounds on the magnitude of the coefficients of the integral operator in the wavelet basis as a function of scale and position and, in particular, in terms of whether or not the coefficient lies within a band. Based on these bounds, we can approximate the operator by ignoring coefficients not lying within these bands, thus producing a sparse representation. This sparse representation is extremely beneficial for numerical applications in which one would like to apply the Green's function operator efficiently: normally if such an operator mapped  $N$  points into  $N$  points, it would require  $O(N^2)$  operations; however, with the wavelet transform, the mapping would require only  $O((4M + 2\gamma LM + 2\gamma(1 - \gamma)M - 3)N)$  operations, where  $2M$  is the length associated with the support of the wavelet function,  $L = \log_2 N - 1$ , and  $\gamma = \frac{1}{\ln 2}$ . An application example in which this is important is the control of Smart Structures in which a large number of embedded sensors and actuators must be coordinated in order to achieve disturbance rejection on the surface of the structure.

**Keywords:** wavelets, Green's functions, control, structures

# 1 Introduction

The literature on the use of wavelets to efficiently represent signals and mathematical operators has become extensive, spanning a wide range of applications. While much of the mathematical aspects of wavelet representations of operators has its origins in the work of Meyer [9], the work of Beylkin et al. [1] was perhaps the first presentation of numerical results that generated a great deal of interest in the idea of using wavelets to develop *sparse* representations of operators. In [1], wavelets were used to compress Calderon-Zygmund and pseudo-differential operators. In this work it was shown that representations of these operators using tensor products of one-dimensional wavelets were extremely efficient in the sense that few wavelet coefficients were needed to represent the operators with arbitrarily specified accuracy. In this paper, we focus on the use of wavelet transforms in compressing integral operators whose kernel is a Green's function associated with a linear differential equation. While there has been much work in using wavelets to solve partial differential equations (PDEs) numerically using finite difference and Galerkin methods [3, 5], our objective is to present a novel analysis of *Green's functions* associated with the integral form of the solution to a linear differential equation and to show how the sparsity of wavelet representations of Green's function integral operators follows naturally from properties of both wavelets and Green's functions.

Our paper presents an analysis of the use of wavelets with vanishing moments to represent integral operators associated with Green's functions for linear differential equations. We show that integral operators of this type can be efficiently represented in such wavelet bases, i.e. very few wavelet coefficients need to be retained to faithfully represent the operator. Furthermore, there exist extremely efficient algorithms for computing the wavelet transform [4], making the overall transformation scheme a viable method for efficiently realizing the Green's function operator. This efficiency is important for such applications as numerical integration, the numerical solution of differential equations, the solution of inverse problems, as well as for ongoing work we are performing in the area of the control of "Smart Structures"[2]. Furthermore, we are currently working on extensions of this work to the solution of PDEs.

We apply our analysis to the class of Green's functions associated with differential equations of the following form:

$$\mathcal{L}u = f \tag{1}$$

where  $\mathcal{L}$  is a linear, differential operator,  $u$  is the solution to the differential equation, and  $f$  is the forcing term. The solution  $u$  can be represented in integral form as follows.

$$u(r) = \int_S G(r, s) f(s) ds \tag{2}$$

where  $G(r, s)$  is the Green's function kernel of the integral operator. We will refer to the variable  $r$  as the observation variable, and the variable  $s$  as the source variable.

The main contribution of this paper is an analysis of the structure of the representation of Green's function integral operators in wavelet bases. In particular, we characterize the sparsity of the

transformed operator in terms of basic properties of Green's functions. Our analysis relies on the following fundamental property of Green's functions: For linear differential operators with smooth coefficients, the associated Green's function is smooth (in the  $C^\infty$  sense) in *both* the source and observation variables, *except* at points where they are equal. Furthermore, at points where they are equal, i.e., where the source and observation locations coincide, for each coordinate in both observation and source variables, the highest derivative of the Green's function with respect to that coordinate is *singular*. This fact reflects the basic physical property that a Dirac delta forcing function introduces a singularity in the highest order derivative of the Green's function with respect to the observation variable at the point of forcing.

Our paper presents an analysis of the structure of the Green's function integral operator coefficients in the wavelet representation, and in particular, this analysis reveals explicitly the sparse structure of the operator in this representation as a function of spatial scale and position, and as a function of the structure of the singularities in the Green's function. Our analysis exploits the fact that wavelets are particularly well-suited to analyzing singularities. The use of wavelet transforms in analyzing singularities is widely recognized in such applications as image analysis [7], where wavelets help reveal the structure of edges in an image. In [7], wavelets were used to characterize the Lipschitz regularity of a function based on the decay rate of the wavelet coefficients as a function of scale. In [8] wavelets are used to analyze singularities arising in turbulence. In all these applications, the fact that wavelets have a finite number of vanishing moments is essential, enabling the wavelets to discriminate between smooth portions of functions and their points of singularity. Note that the thrust of this paper is to provide a theoretical basis for approximating Green's function integral operators as sparse operators in the wavelet domain. An example application where this is particularly useful, which we will not discuss in detail in this paper, is the control of Smart Structures. In this application, one might, for example, want to control the vibration of the structure using embedded sensors and actuators. In [2], a method is used in which the transfer function from actuator inputs to sensor outputs is modeled as a Green's function operator and an extremely efficient algorithm is developed to control a structure containing large arrays of sensors and actuators.

The paper is organized as follows. In Section 2, we give background on orthonormal wavelets with compact support. Note that while we perform our analysis specifically using orthonormal wavelets, our results do not in fact rely on this property, as we will point out later. We then review the vanishing moments property of wavelets and some results on analyzing the singularities of functions in terms of Lipschitz regularity. In Section 3, we develop our characterization of the wavelet representation of Green's function integral operators, using fundamental properties of Green's functions as well as the vanishing moments property of wavelets. We also provide bounds for the magnitude of the coefficients as a function of scale and position of the wavelet basis functions associated with each coefficient. Then, in Section 4 we give numerical examples of our results based on a differential equation describing the behavior of a flexible beam (Euler-Bernoulli beam). These examples illustrate the multiband structure of the discretized integral operator in the wavelet basis as well as the scale and position dependencies of the operator coefficients predicted by our results. Finally, in Section 5 we state conclusions of our work and point out extensions that we are currently researching.



## 2 Background

In this section we give background on wavelets with an arbitrary number of vanishing moments. We treat specifically the case of orthonormal wavelets of compact support, although our results can be developed for the case of non-orthogonal wavelets as well. The issue of compact support of the basis functions is, however, a key issue in our development. We then give some background on the relationship between the number of vanishing moments of a wavelet basis function and the ability of the basis set to represent smooth functions efficiently.

### 2.1 Orthonormal Wavelets of Compact Support

The basic structure of scale-based wavelet transforms<sup>1</sup> builds on the idea that a space of functions, such as  $L^2(\mathcal{R})$ , can be spanned by a basis set consisting of dilations and translations of a single, properly chosen function:

$$\{\Psi(2^m x - n) \text{ for } m, n \text{ integer}\} \quad (3)$$

The basic wavelet function  $\Psi$  is in general oscillatory and compressed in  $x$  - hence the name. For our purposes one of the most interesting aspects of bases of the type in eq.(3) is the fact that under certain conditions, transforming a signal in these basis functions can be interpreted as performing what is known as a *multiresolution analysis* of the signal [6]. In this analysis the signal is represented at different resolutions using a *scaling function*,  $\Phi$ , which is used to blur the signal at different resolutions.

The multiresolution analysis interpretation of the wavelet transform can be summarized by the following key points.

- Translations of the scaling function for a fixed scale  $m$ ,  $\{\Phi(2^m x - n) \text{ for } n \text{ integer}\}$ , define a subspace of  $L^2(\mathcal{R})$ . At this scale, a signal is represented by projecting the signal onto this subspace .
- Translations of the wavelet function for a fixed scale  $m$ ,  $\{\Psi(2^m x - n) \text{ for } n \text{ integer}\}$ , span the subspace defined by the difference between the scaling subspace at scale  $m$  and the scaling subspace at scale  $m - 1$ .
- Wavelet basis coefficients can be computed *recursively* in scale, resulting in an extremely efficient procedure.

In [4] a class of wavelets was introduced in which the wavelets are compactly supported and orthonormal. Furthermore, a characteristic of this class of wavelets is that their transforms can

---

<sup>1</sup>As opposed, for example, to time-frequency representations such as Gabor transforms, which some include in the wavelet class.

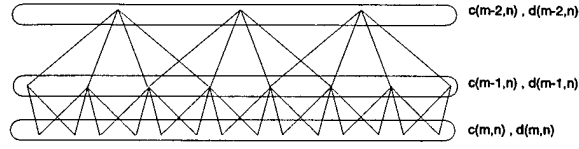


Figure 1: Domain of Lattice Algorithm for Computing Wavelet Coefficients

be computed efficiently via a scale recursion. Let us define the scaling coefficients and wavelet coefficients as follows for some signal  $f(x)$ :

$$c(m, n) = \int_{-\infty}^{\infty} \Phi(2^m x - n) f(x) dx \quad (4)$$

$$d(m, n) = \int_{-\infty}^{\infty} \Psi(2^m x - n) f(x) dx \quad (5)$$

It is shown in [4] that the following equations can be used to compute the scaling and wavelet coefficients recursively in scale from fine to coarse:

$$c(m, n) = \sum_k c(m+1, k) h(2n - k) \quad (6)$$

$$d(m, n) = \sum_k c(m+1, k) g(2n - k) \quad (7)$$

Each of the recursions in eq.'s(6,7) can be interpreted as discrete filtering followed by downsampling by a factor of two. The scaling function filter  $h(n)$  is related to the wavelet filter  $g(n)$  by:  $g(n) = (-1)^n h(1 - n)$ . Furthermore, for compactly supported wavelets  $h(n)$  and  $g(n)$  are FIR filters (typically, of length  $< 12$ ). The computational complexity for the algorithm described by eq.'s(6,7) is order  $O(NM)$  where  $2M$  is the length of  $h$  and  $g$  and  $N$  is the number of coefficients at the initial (finest) scale. The algorithm flow is illustrated in Figure 1 for the case of 4-tap FIR filters  $h$  and  $g$ , where the  $c$  and  $d$  coefficients are computed recursively up the lattice.

The inverse transform, i.e. reconstructing the scaling coefficients at the finest scale from wavelet coefficients at all coarser scales, consists of the following recursion in scale from coarse to fine, which represents the adjoint of the operation described in eq.'s(6,7).

$$c(m+1, 2n) = \sum_k c(m, k) h(n - k) + \sum_k d(m, k) g(n - k) \quad (8)$$

The algorithm flow would correspond to propagating down the lattice in Figure 1. Again, the computational complexity is  $O(NM)$ .

What these fast wavelet algorithms suggest is the possibility of using fast basis transformations in applying our Green's function integral operator, and, assuming this operator is sparse in the wavelet basis, for implementing a scheme which would, overall, be extremely efficient. Note that although we are dealing with an operator that can be viewed as a superposition integral, it is in general *not* shift-invariant; thus, the discretized operator would not be implementable using an FFT. Also, the wavelet transform is highly parallelizable, offering the possibility of extremely fast computations using multiprocessor schemes.

## 2.2 Compression Properties of Wavelets

In this section we review some results in [1] and [7] on using wavelets both to characterize the regularity of functions and to compress or “sparsify” operators. These results motivate our use of wavelet bases to compress operators of the form in eq.(2). We also derive useful results on Lipschitz regularity of a function at a point and its relationship to polynomial approximation of the function at that point. These results will aid in our analysis of representing Green’s function integral operators in wavelet bases.

The main idea in using wavelets to compress operators is to take advantage of the fact that the wavelet bases, for example those designed in [4], can be used to represent smooth operators efficiently. The feature of these wavelets that allows such compression is referred to as the property of “vanishing moments,” which is described as follows.

$$\int_{-\infty}^{\infty} \Psi(x)x^m dx = 0 \text{ for } m = 0, 1, \dots, M-1 \quad (9)$$

This property is a direct result of the fact that the Fourier transform of the filter  $h(n)$  has  $M$  zeros at  $\omega = \pi$  and that, consequently, the Fourier transform of the filter  $g(n)$  has  $M$  zeros at  $\omega = 0$ . It is also true that the number of vanishing moments,  $M$ , is proportional to the support length of the wavelet or the length of the discrete filters  $h(n)$  and  $g(n)$ .

The reason this property is essential to compressing smooth operators is the fact that when one integrates a smooth function,  $f(x)$ , against a wavelet basis function,  $\Psi(2^m x - n)$ , satisfying eq.(9), the first  $M$  terms of the Taylor expansion of  $f$  vanish and one is left with the integral of the product of  $\Psi$  and the  $M$ th order remainder term of the expansion. What this means for integral operators is that we can relate compression efficiency of the wavelet basis in terms of smoothness properties of the kernel of the operator. In [1] the class of Calderon-Zygmund integral operators are considered, which have the property of being smooth away from the diagonal. In particular, kernels  $K(x, y)$  associated with operators in this class satisfy the following:

$$|K(x, y)| \leq \frac{1}{|x - y|} \quad (10)$$

$$|\partial_x^M K(x, y)| + |\partial_y^M K(x, y)| \leq \frac{C_M}{|x - y|^{1+M}} \quad (11)$$

From the fact that the  $M$ th partials of  $K$  decay strongly away from the diagonals, along with the vanishing moment property in eq.(9), one can show that the wavelet coefficients decay in a similar fashion as a function of the distance between coefficients, i.e. the distance between the centers of the basis functions corresponding to two coefficients.

In this paper we consider operators that are *not* restricted to the Calderon-Zygmund class. In fact, the operators can be frequency dependent, spatially varying in their parameters, and in general depend on boundary conditions. Furthermore, what we exploit in our kernels is not the fact that they decay away from their diagonals; in fact for many applications they do not.

Rather, we exploit the fact that Green's function kernels exhibit *singularities* on the diagonals at a derivative of some order.

In order to understand more precisely the implications of applying wavelets with vanishing moments to a kernel with a singularity on its diagonal, we state precisely what we mean by a singularity of a function at a point at some order derivative. Furthermore, we will be exploiting the vanishing moments property of wavelets by taking Taylor expansions of the Green's function up to some order. Thus, we would like to understand the relationship between the order derivative at the point at which there is a discontinuity and the order of the Taylor expansion about that point. In the following, we derive statements about polynomial approximations of a function about a point at which we know there is a singularity at some order derivative.

Let us define the local smoothness of a function at a point in terms of Lipschitz exponents in the following way [7]:

**Definition 2.1** For  $n$  a positive integer, a function  $f(x)$  is Lipschitz  $n + 1$  at  $x_0$  if there exist constants  $A$  and  $h_0 > 0$ , and a polynomial of order  $n$ ,  $P_n(x)$ , such that for  $0 \leq h < h_0$

$$|f(x_0 + h) - P_n(h)| \leq Ah^{n+1} \quad (12)$$

We now state the following theorem (see Appendix A for a proof), which will allow us to show precisely why the limited differentiability of a function  $f$  prevents us from approximating  $f$  by a polynomial to arbitrary order.

**Theorem 2.1** For  $n$  a positive integer, if  $f(x)$  is Lipschitz  $n + 1$  at  $x_0$  and  $f(x)$  is  $C^n$  for  $0 < |x - x_0| < \gamma$ ,  $\gamma > 0$ , then  $f(x)$  is  $n$  times differentiable at  $x_0$  and the polynomial  $P_n(h)$  is equal to the first  $n + 1$  terms of the Taylor series expansion of  $f(x)$  about  $x_0$ .

Note that this is a strong theorem relating differentiability of a function and approximation of a function by a polynomial. In particular, for example, if the  $n$ th derivative of  $f$  does not exist at  $x_0$ , there is no polynomial of order  $n$  that approximates  $f$  with order  $h^{n+1}$  accuracy. We state this more precisely in the following corollaries, the first of which is essentially a restatement of Theorem 2.1 in contrapositive form.

**Corollary 2.1** Let  $f(x)$  be  $C^\infty$  in a neighborhood about  $x_0$ , excluding  $x_0$ , i.e.  $C^\infty$  for  $x$  such that  $0 < |x - x_0| < \gamma$ ,  $\gamma > 0$ . For  $n$  a positive integer, if  $f(x)$  is not  $n$  times differentiable at  $x_0$ , then  $f(x)$  is not Lipschitz  $n + 1$  at  $x_0$ . Furthermore,  $f$  is not Lipschitz  $j$  at  $x_0$  for  $j > n + 1$ . In particular, for all constants  $A$  and  $h_0 > 0$ , and for all polynomials of order  $j$ ,  $P_j(x)$ ,  $j \geq n$ , there exists an  $h$  such that  $0 \leq h < h_0$  and

$$|f(x_0 + h) - P_j(h)| > Ah^{j+1} \quad (13)$$

This corollary can be strengthened into the following corollary.

**Corollary 2.2** *Let  $f(x)$  be  $C^\infty$  in a neighborhood about  $x_0$ , excluding  $x_0$ , i.e.  $C^\infty$  for  $x$  such that  $0 < |x - x_0| < \gamma$ ,  $\gamma > 0$ . For  $n$  a positive integer, if  $f(x)$  is not  $n$  times differentiable at  $x_0$ , then for all constants  $A$  and  $h_0 > 0$ , and for all polynomials of order  $j$ ,  $P_j(x)$ ,  $j \geq n$ , there exists an  $h$  such that  $0 \leq h < h_0$  and*

$$|f(x_0 + h) - P_j(h)| > Ah^{n+1} \quad (14)$$

### Proof

We know from Corollary 2.1 the following. For all constants  $A$  and  $h_0 > 0$ , and for all polynomials of order  $j$ ,  $P_j(x)$ ,  $j \geq n$ , there exists an  $h$  such that  $0 \leq h < h_0$  and

$$|f(x_0 + h) - P_j(h)| > Ah^{j+1} \quad (15)$$

Suppose there exists a  $j \geq n$  and constants  $B, h_0 > 0$  such that

$$|f(x_0 + h) - P_j(h)| \leq Bh^{n+1} \quad (16)$$

for  $0 \leq h < h_0$ . Let  $P_j(h) = \sum_{k=0}^j \rho_k h^k$  and let  $P_n(h)$  denote the first  $n+1$  terms of  $P_j(h)$ . Then, from the triangle inequality eq.(16) can be written as the following.

$$|f(x_0 + h) - P_n(h)| \leq \sum_{k=n+1}^j |\rho_k| h^k + Bh^{n+1} \quad (17)$$

Then, we can find  $C, \tilde{h}_0 > 0$  such that

$$|f(x_0 + h) - P_n(h)| \leq Ch^{n+1} \quad (18)$$

for  $0 \leq h < \tilde{h}_0$ . But this contradicts eq.(15) for the case  $j = n$  and  $P_j(h) = P_n(h)$ .

□

As we will see, these corollaries will be used in showing how limited differentiability of the kernel of our integral operator, i.e. the Green's function, affects our ability to exploit the vanishing moments property, eq.(9), of wavelets.

## 3 Representation of Green's Function Operator in Wavelet Basis

In this section we use properties of Green's functions to characterize the structure of the associated integral operator in the wavelet basis. This transformed operator is sparse in the sense that

the magnitude of the coefficients along various bands is large relative to the magnitude of the coefficients off these bands, allowing one to approximate the operator by ignoring the off-band coefficients with relatively little error. We show explicitly how the limited differentiability of the Green's functions along their diagonal accounts for the structure of these bands. Furthermore, we give bounds on the relative magnitude of the coefficients on and off these bands. Note that while our analysis is performed for a one-dimensional system, we discuss in the conclusions extensions of this analysis to multidimensional systems.

### 3.1 Properties of Green's Functions

Consider the following inhomogeneous differential equation:

$$\mathcal{L}u = f \quad (19)$$

where both the solution  $u$  and the forcing function  $f$  are defined on the interval  $[0, 1]$  with homogeneous boundary conditions. Let us also assume that the spatial differential operator  $\mathcal{L}$  is of the form

$$\mathcal{L} = \sum_{z \in Z} \lambda_z(r) \partial_r^z \quad (20)$$

where  $Z$  is a subset of the natural numbers, and  $\lambda_z(r)$  is a smooth function of  $r$ , i.e.  $\lambda_z(r) \in C^\infty$ .

The Green's function integral form of the solution can be written as the following:

$$u(r) = \int_S G(r, s) f(s) ds \quad (21)$$

where  $G(r, s)$  is the Green's function associated with  $\mathcal{L}$  and is itself the solution to the following differential equation.

$$\mathcal{L}G(r, s) = \delta(r - s) \quad (22)$$

where  $\mathcal{L}$  is applied to the variable  $r$ . Note that we use  $r$  to denote a point in the observation or "output" space of the Green's function, (e.g. the point of displacement for a mechanical system, while we use  $s$  to denote a point in the source or "input" space of the Green's function, e.g. the point of forcing).

The key property of  $G$  that will lead us to its compression in the wavelet basis is the fact that it is smooth everywhere except along its diagonal where  $r = s$ , i.e. where the output location coincides with the input location. For the case where  $r = s$ , from eq.(22)  $G$  must have partial derivatives of some order that are singular. One way to see this is to observe the fact that the delta function on the right-hand side of eq.(22) implies a singularity in some of the terms on the left-hand side of eq.(22) at the point  $r = s$ . From eq.(20) we see that the left-hand side of eq.(22) comprises a sum, weighted by smooth functions, of partial derivatives of  $G$  with respect to components of  $r$ . In particular,

$$\sum_{z \in Z} \lambda_z(r) \partial_r^z G(r, s) = \delta(r - s) \quad (23)$$

Let  $T + 1$  denote that highest derivative in the summation in eq.(23). We then rewrite eq.(23), isolating terms involving  $\partial_r^{T+1}G$  as follows.

$$\lambda_{T+1}(r)\partial_{\partial_r^{T+1}}G(r, s) = \delta(r - s) + e(r) \quad (24)$$

where  $e(r)$  is a linear combination, weighted by smooth functions, of derivatives of  $G$  with respect to  $r$  of order less than  $T + 1$ . Note that derivatives of  $G$  with respect to  $r$  of order  $j$  for  $j < T + 1$  must be strictly smoother than the  $T + 1$ st derivative of  $G$ . Thus, eq.(24) shows  $\partial_r^{T+1}G$  to be smooth for all  $r$  except at  $r = s$ , where it is a delta function. Note that this makes  $\partial_r^T G$  discontinuous at  $r = s$  and  $G \in C^\infty$  for  $r \neq s$ . We state this fundamental property of Green's functions as follows.

**Property 3.1** *Smoothness Property of Green's Function (I)*

Let  $G(r; s)$  denote the Green's function as a function of the observation point  $r$ , holding the source point  $s$  fixed. Then,  $G(r; s) \in C^\infty$  for  $r \neq s$  whereas for  $r = s$ ,  $G(r; s) \in C^{T-1}$ , i.e.  $\partial_r^T G(r; s)$  is discontinuous at  $r = s$ .

We have shown that by fixing  $s$ ,  $G$  is smooth as a function of  $r$  everywhere except at  $r = s$ . However, we are ultimately interested in transforming the coordinates of the Green's function operator into wavelet basis coordinates in both input and output spaces. In other words, in representing our integral operator we need to integrate  $G$  with respect to wavelet basis functions in  $s$  as well as in  $r$ . Thus, we would like to show that by fixing  $r$ ,  $G$  is smooth as a function of  $s$  everywhere except at  $s = r$ .

In order to describe how  $G$  behaves as a function of  $s$ , holding  $r$  fixed, we invoke the reciprocity property of Green's functions [10], which says that  $G(r, s) = \tilde{G}(s, r)$  where  $\tilde{G}(s, r)$  is the Green's function associated with the adjoint of  $\mathcal{L}$ . Whereas before we analyzed the properties of  $\mathcal{L}$  to deduce smoothness properties of  $G$  as a function of  $r$ , we now analyze properties of the adjoint of  $\mathcal{L}$ , which we denote as  $\tilde{\mathcal{L}}$ , to deduce smoothness properties of  $G$  as a function of  $s$ . In particular, from the definition of  $\mathcal{L}$  in eq.(20),  $\tilde{\mathcal{L}}$  can be written as follows [10].

$$\tilde{\mathcal{L}} = \sum_{z \in Z} (-1)^z \partial_s^z \lambda_z(s) \quad (25)$$

The Green's function for this adjoint operator,  $\tilde{G}(s, r)$ , satisfies the following equation.

$$\sum_{z \in Z} \partial_s^z \lambda_z(s) \tilde{G}(s, r) = \delta(s - r) \quad (26)$$

Given our assumption of smooth weighting functions  $\lambda_z(r)$ , we can apply the same argument to eq.(26) as we did to eq.(23). It then follows that Property 3.1 holds for  $\tilde{G}$  as a function of  $s$ , holding  $r$  fixed. From reciprocity, we can then conclude that Property 3.1 holds for  $G$  as a function of  $s$ , holding  $r$  fixed. In particular,

**Property 3.2 Smoothness Property of Green's Function (II)** Let  $G(s; r)$  denote the Green's function as a function of the source point  $s$ , holding the observation point  $r$  fixed. Then,  $G(s; r) \in C^\infty$  for  $s \neq r$  whereas for  $s = r$ ,  $G(s; r) \in C^{T-1}$ , i.e.  $\partial_s^T G(s; r)$  is discontinuous at  $s = r$ .

Finally, we note that for self-adjoint operators the reciprocity property of Green's functions states that  $G(r, s) = G(s, r)$ , i.e. the Green's function is a self-adjoint kernel. This has implications on the smoothness properties on the diagonal of  $G$  in that  $\partial_r G(r, s) = \partial_s G(s, r)$ .

**Property 3.3 Smoothness Property of Green's Function (Self-Adjoint Case)** Let  $G(r, s)$  denote the Green's function of a self-adjoint differential operator. Then,  $G(r, s) \in C^\infty$  for  $s \neq r$  whereas for  $s = r$ ,  $\partial_s^\alpha \partial_r^\beta G(r, s)$  is discontinuous, whenever  $\alpha + \beta = T - 1$ .

In summary, Green's functions satisfying eq.(19) are smooth off their diagonal, i.e. for  $r \neq s$ , while on the diagonal they are  $C^{T-1}$ , where  $T + 1$  is the highest derivative of the differential operator. For the case of self-adjoint differential operators, the condition on the diagonal is such that mixed partials with respect to  $r$  and  $s$  are discontinuous when the sum of the orders of the partials is  $T - 1$ .

### 3.2 Structure of Wavelet Transformed Integral Operator

In this section we reveal the fundamental structure of the Green's function integral operator in the wavelet basis. We begin with the definition of the operator coefficients in the wavelet basis, assuming a complete, orthonormal wavelet basis defined on the interval  $[0, 1]$ . This basis set is defined as follows.

$$\{\Psi(2^m r - n)\} \quad (27)$$

for all integers  $m, n$ , where  $m$  is the scale index and  $n$  is the translation index.

We now express the coefficients of the integral operator in the basis given in eq.(27) as follows.

$$\alpha_{m,n,\bar{m},\bar{n}} = \int_{2^{-m}n}^{2^{-m}(n+1)} \int_{2^{-\bar{m}}\bar{n}}^{2^{-\bar{m}}(\bar{n}+1)} G(r, s) \Psi(2^m r - n) \Psi(2^{\bar{m}} s - \bar{n}) dr ds \quad (28)$$

Consider the following equations for the coefficients of the transformed functions in both the input and output spaces of the operator.

$$x_{m,n} = \int_{2^{-m}n}^{2^{-m}(n+1)} \Psi(2^m s - n) x(s) ds \quad (29)$$

$$y_{m,n} = \int_{2^{-m}n}^{2^{-m}(n+1)} \Psi(2^m r - n) y(r) dr \quad (30)$$

Then, the following equation describes the integral operator mapping between these functions in the wavelet basis.

$$y_{m,n} = \sum_{\bar{m},\bar{n}} \alpha_{m,n,\bar{m},\bar{n}} x_{\bar{m},\bar{n}} \quad (31)$$



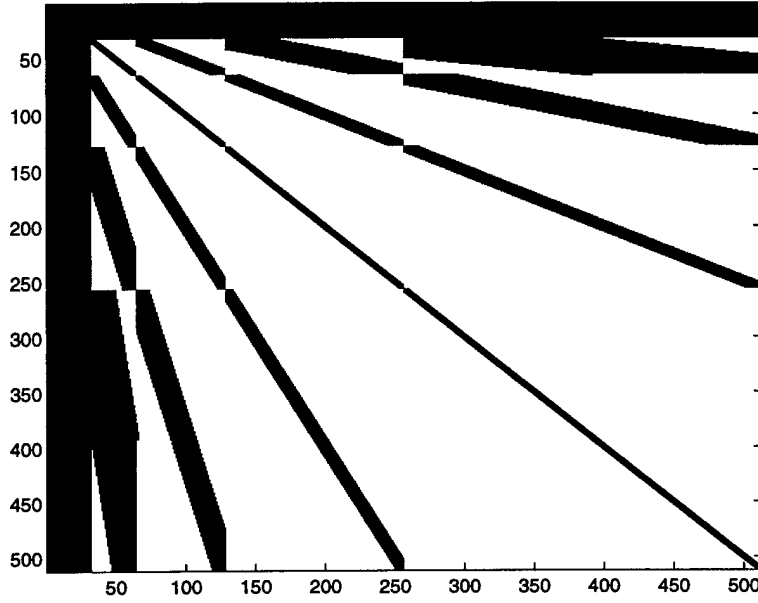


Figure 2: Matrix representing wavelet transformed integral operator. Dark points represent coefficients corresponding to basis functions whose support include the diagonal of  $G$ . A 8-tap Daubechies filter is used on an interval with 256 uniformly sampled points .

In performing the integrals in eq.(28) there are two cases to consider based on the bounds of integration with respect to  $dr$  and the bounds of integration with respect to  $ds$ , which we denote as follows.

$$\Omega_r = [2^{-m}n, 2^{-m}(n+1)] \quad (32)$$

$$\Omega_s = [2^{-\bar{m}}\bar{n}, 2^{-\bar{m}}(\bar{n}+1)] \quad (33)$$

The two cases to consider consist of: 1)  $\Omega_r \cap \Omega_s = \emptyset$  and 2)  $\Omega_r \cap \Omega_s \neq \emptyset$ . For Case 1, in performing our integration we can consider  $G(r, s)$  to have the properties for the case of  $r \neq s$ , while for Case 2, in performing our integration we must consider  $G(r, s)$  to have the properties for the case of  $r = s$ . An interpretation of Case 1 is that we are considering the case where the support of the wavelet functions for the observation and source positions do not overlap, while for Case 2, we are considering the case where they *do* overlap.

For visual purposes, it is worthwhile at this point to illustrate the structure of the transformed operator imposed by this division between Case 1 and Case 2. In particular, Case 1 corresponds to coefficients whose associated basis functions include the diagonal of  $G$  in their support. The fact that basis functions that include the diagonal exist at multiple scales gives rise to a multiband structure, where each band corresponds to a pair of basis functions, in  $r$  and  $s$ , whose support differ by some power of two. The width of each band is simply the sum of the supports of the basis functions in  $r$  and  $s$ . We illustrate this multiple band structure of the operator in Figure 2 for the case of an 8-tap Daubechies filter with four vanishing moments.

For Case 1, we know from Properties 3.1 and 3.2 that  $G(r, s)$  is a smooth function in both  $r$

and  $s$ . Thus, from Taylor's theorem we can expand  $G(r, s)$  as a polynomial in  $r$  and  $s$  up to arbitrary order. Using the vanishing moments property of wavelets in eq.(9), the expression for the operator coefficients in the wavelet basis as given in eq.(28) can be reduced to a double integral of the remainder term of the Taylor expansion with respect to the wavelet basis functions in  $r$  and  $s$ . The important point in this case is the fact that for wavelets of any given order vanishing moments, the operator coefficients are equal to a double integral of a remainder term corresponding to a Taylor expansion of that order. We will show in the next section explicit upper bounds for the magnitude of these coefficients. In particular, this will show that for Case 1 the magnitude of the operator coefficients can be made *arbitrarily small* given wavelets of arbitrary order vanishing moments.

For Case 2, we know from Properties 3.1 and 3.2 that for  $r = s$ ,  $G(r, s)$  is smooth in  $r$  and  $s$  only to a certain order derivative in each of the coordinates, where the order is related to the highest order derivative of the particular differential operator  $\mathcal{L}$ . For the case of self-adjoint  $\mathcal{L}$ , from Property 3.3 we know that the mixed partials with respect to  $r$  and  $s$  are singular when the sum of the orders of the respective partials is equal to the highest order derivative of  $\mathcal{L}$ . Thus, unlike in Case 1, we cannot use a Taylor expansion to expand  $G$  up to arbitrary order. Furthermore, from Corollary 2.1, the fact that  $G$  is smooth only up to some order in each coordinate  $r$  and  $s$  implies the following. For each coordinate  $r$  and  $s$ , if  $n - 1$  is the order of the highest continuous partial derivative in that coordinate, then for *every* polynomial of order  $i$ ,  $i \geq n$ ,  $G$  in that coordinate cannot be approximated by that polynomial with error less than  $O(h^{i+1})$ .

From Corollary 2.1, we can make the stronger claim that for every polynomial of order  $i$ ,  $i \geq n$ ,  $G$  as a function of that coordinate cannot be approximated by a polynomial with error less than  $O(h^{n+1})$ , i.e. higher order approximations of  $G$  have an error that is independent of the order of the approximation. Thus, in contrast to Case 1, where  $G$  could be expanded to arbitrarily higher order terms, in Case 2,  $G$  is *limited* to polynomial approximations of order  $n - 1$  or fewer where  $n$  reflects the structure of  $\mathcal{L}$ . Finally, as we will see explicitly in the next section, the fact that we are limited in the order of the polynomial approximating  $G$  in each of its coordinates limits us in the number of vanishing moments that can be used to bound the operator coefficients in the wavelet basis. This is a key distinction in discriminating between the coefficients in Case 1 and the coefficients in Case 2. Roughly speaking, whereas in Case 1 the magnitudes of the coefficients can be made arbitrarily small with higher and higher order vanishing moments, in Case 2 they cannot.

### 3.3 Bounds on Magnitude of Transformed Operator Coefficients

We now derive bounds on the wavelet transform coefficients for a Green's function integral operator. From Properties 3.1 and 3.2, we know  $G(r, s)$  to be  $C^\infty$  away from  $r = s$  and to be  $T - 1$  times differentiable on the line  $r = s^2$ . The  $T$ 'th order partial derivatives of  $G(r, s)$  are

---

<sup>2</sup>Recall that differentiability on a set for a real function of two variables requires that the partial derivatives exist and are continuous on the set.

assumed to be discontinuous at  $r = s$  and bounded over the domain of interest.

The quadrupally indexed wavelet coefficient,  $\alpha$ , is as given in eq.(28), where  $\Psi$  satisfies the moment property stated in eq.(9), i.e.  $\Psi$  has  $M$  vanishing moments. Recall that the bounds of integration with respect to  $dr$  and  $ds$ , respectively, in eq.(28) are given by

$$\begin{aligned}\Omega_r &= [2^{-m}n, 2^{-m}(n+1)], \text{ and} \\ \Omega_s &= [2^{-\bar{m}}\bar{n}, 2^{-\bar{m}}(\bar{n}+1)]\end{aligned}$$

which reflect the support of the wavelet basis function in the  $r$  and  $s$  directions, respectively. We derive bounds for the two cases identified in the previous section: Case 1)  $\Omega_r \cap \Omega_s = \emptyset$  and Case 2)  $\Omega_r \cap \Omega_s \neq \emptyset$ . The bounds rely upon the smoothness properties of  $G(r, s)$  and use the multidimensional Taylor series expansion along with the theorem and corollaries introduced in Section 2.2.

### 3.3.1 Case 1: Non-intersecting wavelet support

When the support of the wavelet bases in  $r$  and  $s$  not overlap, the Green's function in the integral in eq.(28) will be  $C^\infty$  over the entire domain of the integral. We derive an upper bound for the magnitude of the wavelet coefficient as a function of scale as follows.

Since  $G(r, s)$  is  $C^\infty$  for  $r$  and  $s$  of interest, we can expand it in a two-dimensional Taylor series about a point,  $(r_0, s_0)$ , to arbitrary order. For convenience, choose the expansion point,  $(r_0, s_0)$  to be  $(2^{-m}n, 2^{-\bar{m}}\bar{n})$ , the endpoint of the wavelet support. We choose to expand the first  $2M - 1$  polynomial terms in the Taylor series so that we can apply the moment property of the wavelet to annihilate the low order behavior of the Green's function. The Taylor series with remainder is given by

$$G(r, s) = G(r_0, s_0) + \sum_{j=1}^{2M-1} \frac{1}{j!} \left( (r - r_0) \frac{\partial}{\partial r} + (s - s_0) \frac{\partial}{\partial s} \right)^j G(r, s)|_{r=r_0, s=s_0} + R_{2M}(r, s) \quad (34)$$

The above expansion involves no approximation when the remainder is included.

The remainder is given by

$$R_{2M+1}(r, s) = \frac{1}{(2M-1)!} \int_0^1 (1-t)^{2M-1} \left( (r - r_0) \frac{\partial}{\partial r} + (s - s_0) \frac{\partial}{\partial s} \right)^{2M} G(r_0 + t(r - r_0), s_0 + t(s - s_0)) dt \quad (35)$$

By substituting the above expansion for  $G$  into eq.(28), applying the moment property of the wavelet basis annihilates all of the polynomial terms in the expansion, leaving for  $\alpha$ , without approximation, the following.

$$\alpha_{m,n,\bar{m},\bar{n}} = \int_{2^{-m}n}^{2^{-m}(n+1)} \int_{2^{-\bar{m}}\bar{n}}^{2^{-\bar{m}}(\bar{n}+1)} \Psi(2^m r - n) \Psi(2^{\bar{m}} s - \bar{n}) R_{2M}(r, s) dr ds \quad (36)$$

We can bound  $\alpha$  by applying the Cauchy-Schwartz inequality to the above equation giving

$$\alpha^2 \leq \int_{2^{-m}n}^{2^{-m}(n+1)} \int_{2^{-m}\bar{n}}^{2^{-m}(\bar{n}+1)} \Psi^2(2^m r - n) \Psi^2(2^m s - \bar{n}) dr ds \int_{2^{-m}n}^{2^{-m}(n+1)} \int_{2^{-m}\bar{n}}^{2^{-m}(\bar{n}+1)} R_{2M}^2(r, s) dr ds \quad (37)$$

The orthonormal property of the wavelet basis,  $\Psi$ , implies that the first double integral is unity. To construct the bound, we note that

$$\left( (r - r_0) \frac{\partial}{\partial r} + (s - s_0) \frac{\partial}{\partial s} \right)^{2M} = \sum_{i=0}^{2M} \beta_i (r - r_0)^i (s - s_0)^{2M-i} \frac{\partial^{2M}}{\partial r^i \partial s^{2M-i}} \quad (38)$$

where  $\beta_i$  are positive integer coefficients of a binomial expansion. Therefore, we can write

$$R_{2M}^2(r, s) = \frac{1}{(2M-1)!^2} \left( \sum_{i=0}^{2M} \beta_i (r - r_0)^i (s - s_0)^{2M-i} \Theta_i \right)^2 \quad (39)$$

$$\Theta_i = \int_0^1 (1-t)^{2M-1} \frac{\partial^{2M}}{\partial r^i \partial s^{2M-i}} G(r_0 + t(r - r_0), s_0 + t(s - s_0)) dt$$

Furthermore, we can use the inequality<sup>3</sup>

$$\left( \sum_{i=0}^{2M} a_i \right)^2 \leq (2M+1) \sum_{i=0}^{2M} a_i^2$$

to show that

$$R_{2M}^2(r, s) \leq \frac{(2M+1)}{(2M-1)!^2} \sum_{i=0}^{2M} \beta_i (r - r_0)^{2i} (s - s_0)^{4M-2i} (\Theta_i)^2 \quad (40)$$

We bound the integral in parenthesis as follows:

$$\begin{aligned} I_i &= \left( \int_0^1 (1-t)^{2M-1} \frac{\partial^{2M}}{\partial r^i \partial s^{2M-i}} G(r_0 + t(r - r_0), s_0 + t(s - s_0)) dt \right)^2 \\ &\leq \int_0^1 (1-t)^{4M-2} dt \int_0^1 \left( \frac{\partial^{2M}}{\partial r^i \partial s^{2M-i}} G(r_0 + t(r - r_0), s_0 + t(s - s_0)) dt \right)^2 dt \quad (\text{Cauchy-Schwartz}) \\ &\leq \frac{B_i^2}{(4M-1)} \end{aligned} \quad (41)$$

where the bound  $B_i^2$  is defined to be

$$B_i^2 = \sup \left( \frac{\partial^{2M}}{\partial r^i \partial s^{2M-i}} G(r, s) dt \right)^2 \quad r \neq s$$

---

<sup>3</sup>The Cauchy-Schwartz Inequality for sequences is  $\left( \sum_{i=1}^T a_i b_i \right)^2 \leq \sum_{i=1}^T a_i^2 \sum_{i=1}^T b_i^2$ . Setting  $b_i = 1$  yields  $\left( \sum_{i=1}^T a_i \right)^2 \leq T \sum_{i=1}^T a_i^2$ .

Returning to eq.(40), we can write

$$R_{2M}^2(r, s) \leq \frac{(2M+1)}{(4M-1)(2M-1)!^2} \sum_{i=0}^{2M} \beta_i B_i^2(r-r_0)^{2i} (s-s_0)^{4M-2i} \quad (42)$$

Finally, returning to eq.(37) and substituting eq.(42) gives for a bound on  $\alpha$

$$\alpha^2 \leq \frac{(2M+1)}{(4M-1)(2M-1)!^2} \int_{2^{-m_n}}^{2^{-m(n+1)}} \int_{2^{-\bar{m}_{\bar{n}}}}^{2^{-\bar{m}(\bar{n}+1)}} \sum_{i=0}^{2M} \beta_i B_i^2(r-r_0)^{2i} (s-s_0)^{4M-2i} dr ds \quad (43)$$

Evaluating the integrals in  $r$  and  $s$  gives for the bound

$$\alpha_{m,n,\bar{m},\bar{n}}^2 \leq \frac{(2M+1)}{(4M-1)(2M-1)!^2} \sum_{i=0}^{2M} \frac{\beta_i B_i^2}{(2i+1)(4M-2i+1)} 2^{-(2i+1)m} 2^{-(4M-2i+1)\bar{m}} \quad (44)$$

Defining a single coefficient,

$$\gamma_i = \frac{(2M+1)\beta_i B_i^2}{(4M-1)(2M-1)!^2 (2i+1)(4M-2i+1)} \quad (45)$$

highlights the scale dependence of the bound

$$\alpha_{m,n,\bar{m},\bar{n}}^2 \leq \sum_{i=0}^{2M} \gamma_i 2^{-(2i+1)m} 2^{-(4M-2i+1)\bar{m}} \quad (46)$$

The above equation bounds the wavelet coefficient as a function of scale,  $m$  and  $\bar{m}$ , for Case 1. The only parameter determining the rate of decay with scale is the wavelet moment order,  $M$ . Note that the bound can be arbitrarily decreased by increasing the number of vanishing moments,  $M$ . Numerical confirmation of this bound will be shown in Section 4.

### 3.3.2 Case 2: Intersecting wavelet support

We now turn to the case where the intersection of  $\Omega_r$  and  $\Omega_s$  is not empty. Here, the integral expression in eq.(28) contains the point  $r = s$  for which the Green's function is discontinuous in the  $T$ 'th order partial derivatives. We again derive a scale dependent bound for the wavelet coefficient in this case that closely follows the derivation in Case 1. We show below that the bound in this case will depend upon the relationship between the "depth" of the singularity in  $G(r, s)$ ,  $T$ , and the moment property of the wavelet basis,  $M$ . When  $2M \leq T-1$ , the wavelet basis does not annihilate enough of the low order behavior of the Green's function to uncover the singularity, and the bound is the same as that derived in Case 1. However, if  $2M > T-1$ , the wavelet strips away enough of the low order behavior of  $G(r, s)$  to expose its singularity, and the bound on the wavelet coefficient differs from Case 1. The derivation for Case 2 proceeds as follows.

As in Case 1, we expand  $G(r, s)$  about a point  $(r_0, s_0) = (2^m n, 2^{\bar{m}} \bar{n})$ . Given that  $G(r, s)$  is  $C^{T-1}$  at  $r = s$ , we can expand  $G$  in the first  $T - 1$  terms of its Taylor series

$$G(r, s) = G(r_0, s_0) + \sum_{j=1}^{T-1} \frac{1}{j!} \left( (r - r_0) \frac{\partial}{\partial r} + (s - s_0) \frac{\partial}{\partial s} \right)^j G(r, s)|_{r=r_0, s=s_0} + R_T(r, s) \quad (47)$$

with the remainder given by

$$R_T(r, s) = \frac{1}{(T-1)!} \int_0^1 (1-t)^{T-1} \left( (r - r_0) \frac{\partial}{\partial r} + (s - s_0) \frac{\partial}{\partial s} \right)^T G(r_0 + t(r - r_0), s_0 + t(s - s_0)) dt \quad (48)$$

Since we assume that  $G(r, s)$  has bounded, discontinuous derivatives at  $r = s$ , the remainder above is well defined. Note that the expansion we are performing in eq.(47) is essentially a one-dimensional Taylor expansion of  $G$  along the line connecting  $(r_0, s_0)$  and  $(r, s)$ ; i.e.  $(r_0 + t(r - r_0), s_0 + t(s - s_0))$ . The expansion is performed with respect to the variable  $t$ , which represents the extent along this line. Thus, by Theorem 2.1 we know that if we wish to approximate  $G$  by a polynomial of order  $T - 1$  along this line with  $O(t^T)$  error, the Taylor expansion in eq.(47) does precisely this. Furthermore, by Corollary 2.2 of Section 2.2, if we wish to approximate  $G$  along  $(r_0 + tr, s_0 + ts)$  by a polynomial of order  $T$  or higher the error is *greater* than  $O(t^{T+1})$ . Thus, given that the Green's function is discontinuous in the  $T$ 'th order partial derivatives for  $r = s$ , eq.(47) represents the highest order expansion of  $G$  with  $O(t^T)$  error; higher order expansions *do not* result in lower order error.

Now, when we substitute eq.(48) into the integral equation for the wavelet coefficient, eq.(28), we make the following observation. If the moment order  $M$  is such that  $2M \leq T - 1$ , then the wavelet bases will not annihilate all of the polynomial terms in the expansion for  $G$ , eq.(47). The remaining polynomial terms will dominate the wavelet decay as a function of scale, precisely as in Case 1, and the bound on the wavelet coefficients as a function of scale will be exactly that given in eq.(46). Conversely, if  $2M > T - 1$ , the wavelet bases will annihilate all of the polynomial terms in the expansion for  $G$ , and the behavior of the wavelet coefficient will be determined by  $R_T(r, s)$ . We turn now to deriving the bound in this case,  $2M > T - 1$ .

The derivation of the bound follows that of Case 1. Substituting the expansion of  $G$  in eq.(48) into eq.(28) and using the moment property of the wavelet bases with  $2M > T - 1$  leaves for  $\alpha$

$$\alpha_{m,n,\bar{m},\bar{n}} = \int_{2^{-m}n}^{2^{-m}(n+1)} \int_{2^{-\bar{m}}\bar{n}}^{2^{-\bar{m}}(\bar{n}+1)} \Psi(2^m r - n) \Psi(2^{\bar{m}} s - \bar{n}) R_T(r, s) dr ds \quad (49)$$

Using the Cauchy-Schwartz inequality and the orthonormal property of the wavelet bases gives

$$\alpha^2 \leq \int_{2^{-m}n}^{2^{-m}(n+1)} \int_{2^{-\bar{m}}\bar{n}}^{2^{-\bar{m}}(\bar{n}+1)} R_T^2(r, s) dr ds \quad (50)$$

As before, we can bound  $R_T^2$  as follows

$$R_T^2 = \frac{1}{(T-1)!^2} \left( \sum_{i=0}^T \bar{\beta}_i (r-r_0)^i (s-s_0)^{T-i} \Theta_i \right)^2 \quad (51)$$

$$\begin{aligned} \Theta_i &= \int_0^1 (1-t)^{T-1} \frac{\partial^T}{\partial r^i \partial s^{T-i}} G(r_0 + t(r-r_0), s_0 + t(s-s_0)) dt \\ R_T^2 &\leq \frac{(T+1)}{(T-1)!^2} \sum_{i=0}^T \bar{\beta}_i (r-r_0)^{2i} (s-s_0)^{2T-2i} (\Theta_i)^2 \end{aligned} \quad (52)$$

$$R_T^2 \leq \frac{(T+1)}{(2T-1)(T-1)!^2} \sum_{i=0}^T \bar{\beta}_i \bar{B}_i^2 (r-r_0)^{2i} (s-s_0)^{2T-2i} \quad (53)$$

where  $\bar{\beta}_i$  are positive integer coefficients of a binomial expansion and  $\bar{B}_i^2$  is given by

$$\bar{B}_i^2 = \sup \left( \frac{\partial^T}{\partial r^i \partial s^{T-i}} G(r, s) \right)^2 \quad r \neq s \quad (54)$$

Returning to eq.(50) and substituting eq.(54) bounds  $\alpha$  as

$$\alpha^2 \leq \frac{(T+1)}{(2T-1)(T-1)!^2} \int_{2^{-m}n}^{2^{-m}(n+1)} \int_{2^{-\bar{m}}\bar{n}}^{2^{-\bar{m}}(\bar{n}+1)} \sum_{i=0}^T \bar{\beta}_i \bar{B}_i^2 (r-r_0)^{2i} (s-s_0)^{2T-2i} dr ds \quad (55)$$

Finally, evaluating the integrals in  $r$  and  $s$  gives

$$\alpha^2 \leq \frac{(T+1)}{(2T-1)(T-1)!^2} \sum_{i=0}^T \frac{\bar{\beta}_i \bar{B}_i^2}{(2i+1)(2T-2i+1)} 2^{-(2i+1)m} 2^{-(2T-2i+2)\bar{m}} \quad (56)$$

As before, we can highlight the scale dependence of the bound by defining

$$\bar{\gamma}_i = \frac{(T+1)\bar{\beta}_i \bar{B}_i^2}{(2T-1)(T-1)!^2 (2i+1)(2T-2i+1)} \quad (57)$$

to give for the bound

$$\alpha^2 \leq \sum_{i=0}^T \bar{\gamma}_i 2^{-(2i+1)m} 2^{-(2T-2i+2)\bar{m}} \quad (58)$$

The above bound gives the decay of the wavelet coefficient with scale when the support of the wavelet includes the singularity in the Green's function. It depends upon the smoothness of the Green's function,  $T$ , and the scales of the wavelet,  $m$  and  $\bar{m}$  and is applicable when  $2M > T-1$ . Note that the form of this bound is identical to that of Case 1 with  $M$  in eq.(46) being replaced by  $T$ . This highlights the fact that whereas for Case 1 the bound on the coefficients can be made arbitrarily small by increasing the number of vanishing moments of the wavelet, for Case 2 the bound for  $2M > T-1$  is *independent* of  $M$ . Numerical confirmation of this bound will be shown in Section 4.

### 3.4 Compression Ratio

Finally, we conclude our analysis of the wavelet representation of the Green's function integral operator with a discussion of the degree of compression one achieves by approximating the integral operator by its significant wavelet coefficients. The bounds in eq.'s(46,58) show that by using wavelets with an arbitrary number of vanishing moments, we can make the coefficients for Case 1 drop off substantially faster away from the diagonal than coefficients for Case 2. This leads naturally to the idea of approximating the operator by zeroing out coefficients corresponding to Case 1, while retaining coefficients corresponding to Case 2. Such an approximation gives rise to an operator whose multiband structure is as illustrated in Figure 2. We now derive a formula for the number of coefficients remaining in the approximation as a function of  $N$ , the number of samples in the interval,  $2M$  the filter length, and  $L$ , the number of scales.

Consider  $N$  samples on the interval  $[0, 1]$ , giving rise to an  $N \times N$  matrix representation of the Green's function integral operator. We let  $K$  denote the number of significant coefficients in the wavelet representation of the integral operator, i.e. the total number of coefficients at all scales lying within the bands representing the case where  $\Omega_r \cap \Omega_s \neq \emptyset$ . We denote the number of scales as  $L = \log_2 N - 1$ . Recall that the filter length is  $2M$ . Let  $W$  denote the width of the band at scales  $m, \bar{m}$ . Based on the fact that  $W$  represents the coefficients at particular scales  $m$  and  $\bar{m}$ , where  $\Omega_r \cap \Omega_s \neq \emptyset$ , we get the following formula for  $W$ .

$$W = M + M2^{|m-\bar{m}|} - 1 \quad (59)$$

Summing all the bands in the transformed operator matrix, we get

$$\begin{aligned} K &= 2 \sum_{m=0}^L \sum_{\bar{m}=0}^m W 2^{\bar{m}} - \sum_{m=0}^L W 2^m \\ &= 2 \sum_{m=0}^L \sum_{\bar{m}=0}^m ((M-1)2^{\bar{m}} + M2^m) - \sum_{m=0}^L (2M-1)2^m \end{aligned} \quad (60)$$

Note that

$$\sum_{m=0}^L \sum_{\bar{m}=0}^m 2^{\bar{m}} = 2(2^{L+1} - 1) - (L+1) \quad (61)$$

We also need to compute the following sum.

$$\sum_{m=0}^L \sum_{\bar{m}=0}^m 2^m = \sum_{m=0}^L 2^m (m+1) \quad (62)$$

The sum,  $\sum_{m=0}^L 2^m m$ , can be bounded above by

$$\int_0^{L+1} 2^t t dt = \gamma(2^{L+1}(L - \gamma + 1) + \gamma) \quad (63)$$



where  $\gamma = \frac{1}{\ln 2}$ .

Thus,

$$\begin{aligned}
K &\leq 2\{(M-1)(2(2^{L+1}-1)-(L+1)) + M(\gamma(2^{L+1}(L-\gamma+1)+\gamma) + (2^{L+1}-1))\} \\
&\quad - (2M-1)(2^{L+1}-1) \\
&\leq (6M-4)(N-1) + \gamma(L-\gamma+1)2MN - (2M-2)(L+1) + 2M\gamma^2 \\
&\quad - (2M-1)N
\end{aligned} \tag{64}$$

For large  $N$ ,

$$\begin{aligned}
K &= O(\{2M(\gamma(L-\gamma+1)+2)-3\}N) \\
&= O((4M+2\gamma LM+2\gamma(1-\gamma)M-3)N)
\end{aligned} \tag{65}$$

From eq.(65) we see that the number of coefficients in the approximation to the operator is of order *linear* in  $N$  as opposed to  $N^2$  as in the case of the full operator. The number of significant coefficients is also dependent on filter length and the number of scales. Clearly, this approximation becomes advantageous rather quickly for large  $N$ . Moreover, by using wavelets with higher order moments one can arbitrarily increase the magnitude of the ratio of the coefficients on the bands to the coefficients off the bands, thus decreasing the approximation error. This is done, however, at the cost of increasing  $M$  and so there is a natural tradeoff between approximation error and number of coefficients.

## 4 Numerical Examples

The results of the prior section allow us to bound the wavelet coefficient of the Green's function subject to the two-dimensional wavelet transform defined in eq.( 28). When the support of the wavelets in  $r$  and  $s$  do not overlap, the bound on the wavelet coefficient is given by eq.( 46). This bounds wavelet coefficients off of diagonal and subdiagonal blocks in the wavelet transform space.

When the support of the  $r$  and  $s$  wavelets overlap and  $2M \leq T-1$ , so that the wavelet moment property is insufficient to annihilate enough low order behavior of  $G(r,s)$  to uncover the singularity, eq.( 46) still bounds the wavelet coefficients. However, when  $2M > T-1$ , the wavelet strips away the low order behavior of the Green's function, up to and including the highest order continuous derivative, and is bounded by eq.( 58). A numerical example confirms these conclusions.

For our example, we use an Euler-Bernoulli beam, whose equation of motion is given by

$$w_{rrrr} + \omega^2 w = -p(r) \quad r \in [0, 1]$$

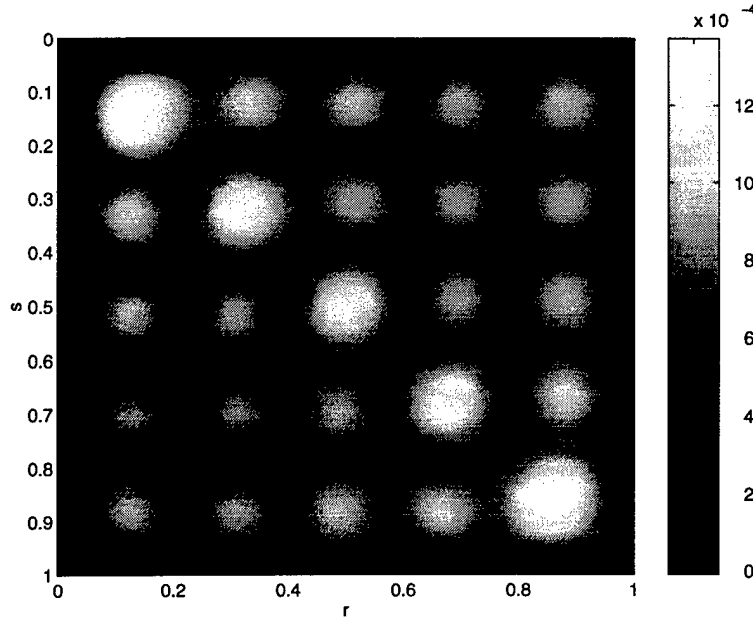


Figure 3: A plot of the magnitude of the Green's function for our Euler-Bernoulli beam with clamped ends as a function of the field point,  $r$  and the source point,  $s$ , and dimensionless frequency,  $\omega = 215$ . The scale is given by the colorbar on the right.

where  $w$  is the dimensionless vertical displacement of the beam,  $\omega$  is dimensionless frequency and  $p$  represents the forcing along the beam. We use clamped boundary conditions

$$w = w_r = 0 \text{ for } r = 0, 1.$$

The Green's function in this case satisfies

$$G(r, s)_{rrrr} + \omega^2 G(r, s) = -\delta(r - s),$$

along with the boundary conditions above. Solution for the Green's function is possible in closed form. Figure 3 shows the magnitude of the Green's function at a dimensionless frequency,  $\omega = 215$ , used for this example.

The Green's function for the Euler-Bernoulli beam above has  $T = 3$ , so that  $G(r, s)$  is  $C^\infty$  everywhere except on  $r = s$  where it is  $C^2$ . Off of the bands in the wavelet representation of the operator, i.e. Case 1, we expect the wavelet coefficients to decay in scale as

$$\alpha_{m,n,\bar{m},\bar{n}}^2 \leq \sum_{i=0}^{2M} \gamma_i 2^{-(2i+1)m} 2^{-(4M-2i+1)\bar{m}}.$$

where  $M$  is the number of vanishing moments of the wavelet. In our examples we use the Daubechies wavelets.

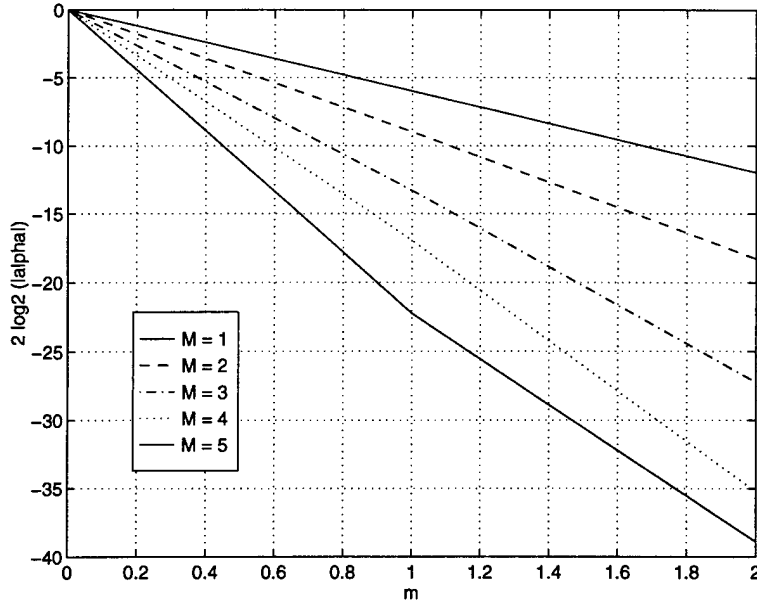


Figure 4: Decay of numerically calculated wavelet coefficient  $\alpha$ , with scale along diagonal blocks of the wavelet transform,  $m = \bar{m}$ . Slope is predicted to go as  $-(4M + 2)$ . The kink in the  $M = 5$  curve is due to the fact that the  $m = 2$  point is smaller than machine precision.

We test our bound by computing  $\alpha$  numerically and finding the supremum of  $\alpha$  off of the diagonals and subdiagonals for each scale,  $m$  and  $\bar{m}$ . We can plot our results compactly by noting that along any set of scales,  $\bar{m} = m + k$ ,  $k$  an integer, the bound looks like

$$\log_2(\alpha^2) \leq -(4M + 2)m + C.$$

Therefore, we expect  $2\log_2(\alpha)$  to be linear with slope  $-(4M + 2)$  as a function of  $m$  along diagonal blocks. Figure 4 shows the decay of the supremum of  $\log_2(\alpha)$  along the blocks  $m = \bar{m}$  when the wavelet bases do not intersect. The lines' intersections with the  $m = 0$  axis have been normalized to zero to show their slopes. Shown are the decay rates for various wavelet bases having different numbers of vanishing moments. As more moments are annihilated by the wavelet,  $M$  increasing, we expect faster decay of the wavelet coefficient, with slopes given by  $-(4M + 2)$ . Figure 4 shows that this is indeed the case. The slopes in the figure show good agreement with the theoretical bound. We believe that departures from the theoretical values are due to the discrete implementation of the wavelet transform. Note that the last point in the  $M = 5$  curve is smaller than machine precision and is, thus, unreliable. In Figure 5, we show the case where  $m = \bar{m} + 1$ . Again, the decay as a function of scale is well predicted by our bound.

Next, we test the bound for the wavelet coefficients when they are on the diagonals of the wavelet transform blocks. Recall that we expect the Case 1 bound if  $2M \leq T - 1$  and the Case Two bound if  $2M > T - 1$ . For the Euler-Bernoulli beam,  $T = 3$ , so that only the  $M = 1$  wavelet (the Haar wavelet), will give the Case 1 bound. Conversely, when  $2M > T - 1$ , we derived a

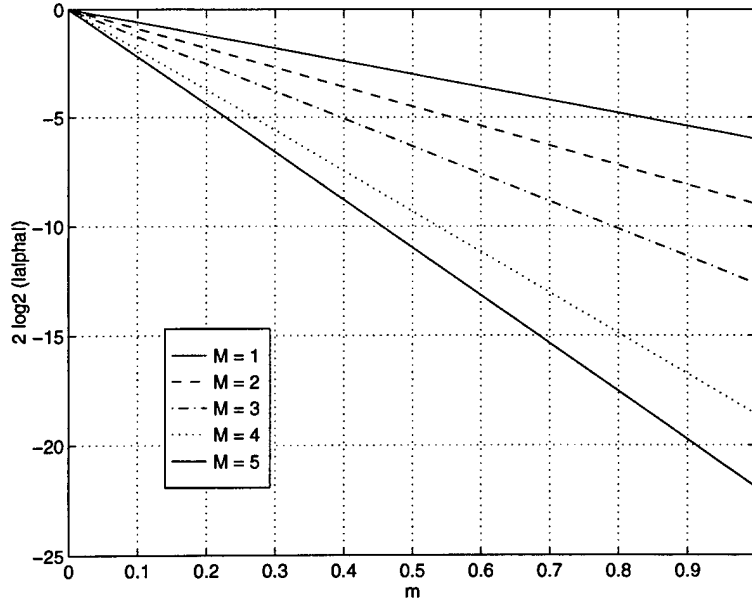


Figure 5: Decay of numerically calculated wavelet coefficient,  $\alpha$ , as a function of scale for,  $\bar{m} = m + 1$ . Theoretically predicted slopes are given by  $-(4M + 2)$ .

bound whose scale dependence is given by

$$\alpha^2 \leq \sum_{i=0}^T \bar{\gamma}_i 2^{-(2i+1)m} 2^{-(2T-2i+2)\bar{m}}.$$

Again, consider the case where  $m = \bar{m} + k$ , with  $k$  an integer. For  $M = 1$ , the Haar wavelet, we expect the Case 2 bound to hold on the main diagonal so that

$$\log_2(\alpha^2) = -6m + C_0,$$

along the diagonal. However, for  $M > 1$ , we expect the Case Two bound to hold so that

$$\log_2(\alpha^2) = -(2T + 2)m = -8 + C_1.$$

Figure 6 shows the decay of numerically obtained wavelet coefficients, supremum of  $\alpha$ , along the main diagonal  $m = \bar{m}$ , as a function of scale for wavelets with  $M = 1, 2, 3$  and 4. As predicted, the slope of the decay for  $M = 1$  is  $-6$  while for all  $M > 1$  the slope is  $-8$ . Likewise, Figure 7 shows the decay of the wavelet coefficient as a function of  $m$  along the first subdiagonal,  $\bar{m} = m + 1$ . As before, we expect the slope of the line to be  $-6$  for  $M = 1$  and  $-8$  for  $M > 1$ . Numerical agreement with the predicted bound is quite good, as shown in the figure.

Finally, we show in Figure 8 the wavelet transformed operator using an 8-tap Daubechies wavelet. Note the multiband structure reflecting the ability of the wavelet to discern the singular behavior of the Green's function along its diagonal. Figure 9 shows the approximated operator derived by keeping only coefficients whose magnitudes are greater than  $1e-8$  times the norm of the operator.

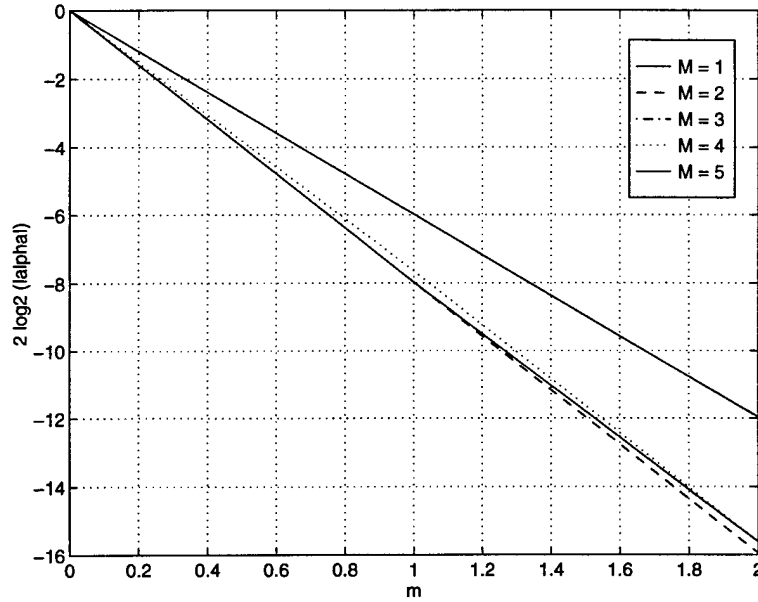


Figure 6: Decay of numerically calculated wavelet coefficient,  $\alpha$ , as a function of scale along the main diagonal. Our theory predicts a slope of -6 for  $M = 1$  and a slope of -8 for  $M > 0$ . The above plot shows excellent agreement with the theoretical bounds.

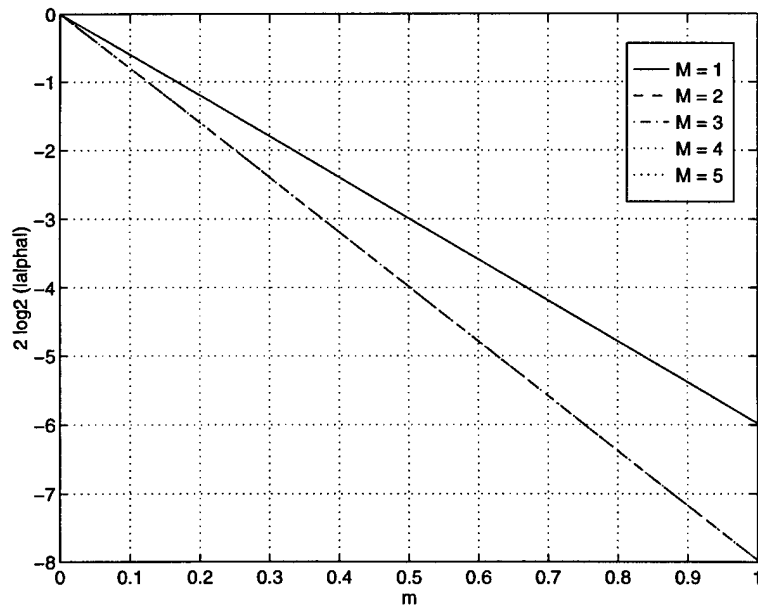


Figure 7: Decay of numerically calculated wavelet coefficient,  $\alpha$ , as a function of scale along the first sub-diagonal,  $\bar{m} = m + 1$ . Our theory predicts a slope of -6 for  $M = 1$  and a slope of -8 for  $M > 0$ . The above plot shows excellent agreement with the theoretical bounds.

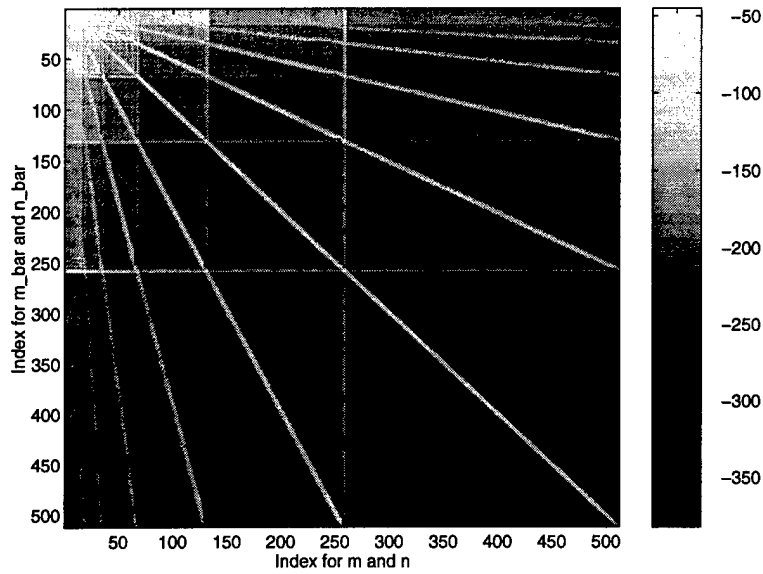


Figure 8: Wavelet transformed operator using 8-tap Daubechies wavelet. A dB intensity scale is used.

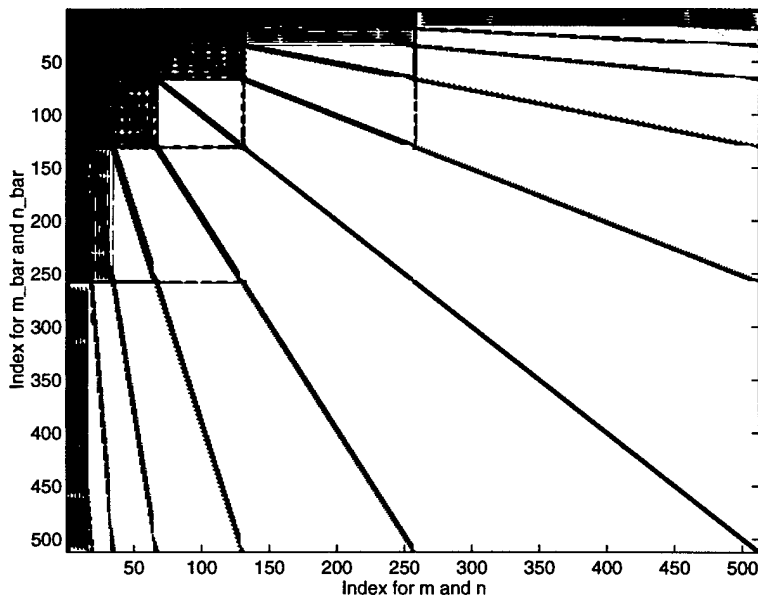


Figure 9: Thresholded values (shown in black) of wavelet transformed operator using 8-tap Daubechies wavelet. Values greater than  $1e-8$  times the norm of the operator are shown.

## 5 Conclusions

In this paper we have analyzed the use of wavelets with vanishing moments in representing Green's function integral operators associated with linear differential equations. We have shown that this representation is sparse, manifesting itself in a multiband structure, and that this structure follows from the moment property of the wavelet and the structure of the singularity of the Green's function along its diagonal. In particular, we show that Green's functions are smooth off its diagonal and limited in its smoothness on its diagonal in the sense that at some order its partial derivatives are discontinuous, where this order corresponds to the highest derivative of the associated differential operator. We then show that in the representation of the integral operator in the wavelet basis, coefficients corresponding to wavelet basis functions whose support include the diagonal of the Green's function behave much differently from coefficients corresponding to basis functions whose support does not include the diagonal. Namely, coefficients that do not include diagonal information can be made arbitrarily small as the number of vanishing moments of the wavelet increase, whereas coefficients that do include diagonal information cannot. Moreover, the bound for the magnitude of these latter coefficients is a function of the highest derivative of the associated differential operator.

The results of this analysis show the wavelet representation of the integral operator to have multiple bands, each of which represents coefficients corresponding to wavelet basis functions of a certain scale whose support includes the diagonal of the Green's function. Our bounds support the idea of approximating the operator by zeroing out coefficients off of the bands, since these coefficients drop off substantially faster away from the diagonal than coefficients on the bands. The compression ratio one gets from doing this is reflected by the fact that the approximated operator has  $O((4M + 2\gamma LM + 2\gamma(1 - \gamma)M - 3)N)$  coefficients as opposed to  $N^2$ . Finally, in Section 4 numerical results show good agreement with predicted results for the case of an Euler-Bernoulli beam whose behavior is governed by a fourth order differential equation.

We are currently extending the results of this paper to the case of PDE's. In this case the smoothness characterization of Green's functions is more subtle than in the case of one dimensional problems. In particular, the relationship between the derivatives of the partial differential operator and the smoothness of its associated Green's function along its diagonal needs to be more fully understood. We believe, however, that results analogous to those in this paper can be derived for the PDE case.

## Acknowledgements

This work is being performed under an ARPA program sponsored by the Office of Naval Research under Contract No. N00014-94-C-0176.

## References

- [1] G. Beylkin, R. Coifman, and V. Rokhlin, "Fast Wavelet Transforms and Numerical Algorithms I," *Communications on Pure and Applied Mathematics*, Vol. XLIV, pp. 141-183, 1991.
- [2] K. Chou, G. Guthart, and D. Flamm, "A Multiscale Approach to the Control of Smart Materials," *SPIE Conference on Smart Structures and Materials*, San Diego, March 1995.
- [3] W. Dahmen, S. Prossdorf, and R. Schneider, "Multiscale Methods for Pseudo-differential Equations on Smooth Closed Manifolds," in *Wavelets: Theory, Algorithms, and Applications*, C. Chui, L. Montefusco, L. Puccio (editors), Academic Press, 1994, pp.385-424.
- [4] I. Daubechies, "Orthonormal bases of compactly supported wavelets", *Communications on Pure and Applied Mathematics*, Vol. XLI, pp. 909-996, 1988.
- [5] S. Jaffard, "Wavelet Methods for Fast Resolution of Elliptic Problems," *SIAM Journal on Numerical Analysis*, Vol. 29, No. 4, pp. pp. 965-986, August 1992.
- [6] S.G. Mallat, "A Theory for Multiresolution Signal Decomposition: The Wavelet Representation", *IEEE Transactions on Pattern Anal. and Mach. Intel.*, Vol. PAMI-11, July 1989, pp. 674-693.
- [7] S. Mallat and W.L. Hwang, "Singularity Detection and Processing with Wavelets," *IEEE Transactions on Information Theory: Special Issue on Wavelet Transforms and Multiresolution Signal Analysis*, Vol. 38, No. 2, March 1992, pp. 617-643.
- [8] C. Meneveau, "Analysis of Turbulence in the Orthonormal Wavelet Representation," *J. Fluid Mechanics*, Vol. 232, 1991, pp. 469-520.
- [9] Y. Meyer, *Ondelettes et Operateurs*, Paris, France: Herman, 1990.
- [10] P. Morse and H. Feshbach, *Methods of Theoretical Physics: Part I*, McGraw-Hill, 1953.

## A Appendix

**Lemma A.1** *For  $n$  a positive integer, if a function  $f(x)$  is Lipschitz  $n + 1$  at  $x_0$ , then it is Lipschitz  $n$  at  $x_0$  and  $P_n(h) = P'_{n-1}(h) + \rho h^n$ , where  $P_n(h)$  and  $P'_{n-1}(h)$  are the polynomials in the Lipschitz  $n + 1$  and  $n$ , respectively, definitions for  $f$  at the point  $x_0$ .*

### Proof

We first assume  $f(x)$  is Lipschitz  $n + 1$  at  $x_0$ . From Definition 2.1 this means there exist constants  $A$  and  $h_0 > 0$ , and a polynomial of order  $n$ ,  $P_n(x)$ , such that for  $0 \leq h < h_0$

$$|f(x_0 + h) - P_n(h)| \leq Ah^{n+1} \quad (66)$$



Let  $P_n(h) = P_{n-1}(h) + \rho h^n$ , where  $P_{n-1}(h)$  represents the first  $n$  terms of the polynomial  $P_n(h)$ . Substituting this into eq.(66) and using the triangle inequality we get

$$|f(x_0 + h) - P_{n-1}(h)| - |\rho|h^n \leq Ah^{n+1} \quad (67)$$

which can be rewritten as

$$|f(x_0 + h) - P_{n-1}(h)| \leq (|\rho| + Ah)h^n \quad (68)$$

If we let  $A' = |\rho| + Ah_0$ , then

$$|f(x_0 + h) - P_{n-1}(h)| \leq A'h^n \quad (69)$$

By definition  $f$  is Lipschitz  $n$  at  $x_0$ , where the polynomial in the definition is in fact  $P_{n-1}(h)$ , i.e. the first  $n$  terms of the polynomial in the definition  $f$ 's being Lipschitz  $n + 1$  at  $x_0$ .

□

**Theorem A.1** *For  $n$  a positive integer, if  $f(x)$  is Lipschitz  $n + 1$  at  $x_0$  and  $f(x)$  is  $C^n$  for  $0 < |x - x_0| < \gamma$ ,  $\gamma > 0$ , then  $f(x)$  is  $n$  times differentiable at  $x_0$  and the polynomial  $P_n(h)$  is equal to the first  $n + 1$  terms of the Taylor series expansion of  $f(x)$  about  $x_0$ .*

### Proof

We use induction on  $n$  to prove this result. For  $n = 1$ ,  $f(x)$  is Lipschitz 2 at  $x_0$ . By letting  $h = 0$  in eq.(12), we get the following.

$$|f(x_0) - P_1(0)| \leq 0 \quad (70)$$

Thus,  $P_1(0) = f(x_0)$ . By using this fact and Definition 2.1, we know that there exist constants  $A$  and  $h_0 > 0$ , and a polynomial of order 1,  $P_1(x)$ , such that for  $0 \leq h < h_0$

$$|f(x_0 + h) - f(x_0) - \rho_1 h| \leq Ah^2 \quad (71)$$

where  $\rho_1$  is the coefficient of the first order term of  $P_1(h)$ . Dividing both sides of eq.(71) by  $h$ , we get

$$\left| \frac{f(x_0 + h) - f(x_0)}{h} - \rho_1 \right| \leq Ah \quad (72)$$

For every  $\epsilon > 0$ , we can choose  $\tilde{h}$  such that the left-hand side of eq.(71) is bounded by  $\epsilon$  whenever  $h < \tilde{h}$ . Thus, the first derivative of  $f$  at  $x_0$  exists and is in fact equal to  $\rho_1$ .

Our induction hypothesis is stated as follows. For  $n - 1$  a positive integer, if  $f(x)$  is Lipschitz  $n$  at  $x_0$  and  $f(x)$  is  $C^{n-1}$  for  $0 < |x - x_0| < \gamma$ ,  $\gamma > 0$ , then  $f(x)$  is  $n - 1$  times differentiable at  $x_0$  and the polynomial  $P_{n-1}(h)$  is equal to the first  $n$  terms of the Taylor series expansion of  $f(x)$  about  $x_0$ .

We now show our induction hypothesis is true for  $n$ . We assume in our theorem statement that  $f(x)$  is Lipschitz  $n + 1$  at  $x_0$ . From Lemma A.1, we know that  $f(x)$  is Lipschitz  $n$  at  $x_0$ , and thus, from our induction hypothesis know that it is  $n - 1$  times differentiable at  $x_0$ . Thus, we can expand  $f$  as follows using the Taylor's theorem with Lagrange's form for the remainder term.

$$f(x_0 + h) = \sum_{i=0}^{n-1} \frac{f^{(i)}(x_0)}{i!} h^i + \frac{f^{(n)}(x_0 + \delta)}{n!} h^n \quad (73)$$

for  $0 < \delta < h$ , where we have used the assumption of the theorem that  $f^{(n)}$  exists in the neighborhood around  $x_0$ , exclusive of  $x_0$ .

We now substitute eq.(73) into eq.(12) and use from Lemma A.1 the fact that  $P_n(h) = P'_{n-1}(h) + \rho_n h^n$  to get the following. There exist constants  $A$  and  $h_0 > 0$ , and a polynomial of order  $n$ ,  $P_n(x)$ , such that for  $0 \leq h < h_0$

$$\left| \sum_{i=0}^{n-1} \frac{f^{(i)}(x_0)}{i!} h^i + \frac{f^{(n)}(x_0 + \delta)}{n!} h^n - P'_{n-1}(h) - \rho_n h^n \right| \leq Ah^{n+1} \quad (74)$$

Since we know from Lemma A.1 that  $f$  is Lipschitz  $n$ , from our induction hypothesis  $f$  is  $n - 1$  times differentiable at  $x_0$  and in fact  $P'_{n-1}(h)$  is equal to the first  $n$  Taylor terms of  $f$  about  $x_0$ . Thus, eq.(74) simplifies to

$$\left| \frac{f^{(n)}(x_0 + \delta)}{n!} h^n - \rho_n h^n \right| \leq Ah^{n+1} \quad (75)$$

Dividing both sides of eq.(75) by  $h^n$ , we get

$$\left| \frac{f^{(n)}(x_0 + \delta)}{n!} - \rho_n \right| \leq Ah \quad (76)$$

For any  $\epsilon > 0$ , we can set  $Ah < \epsilon$ , whereby for any  $\delta < h$  eq.(76) holds. Thus,  $\lim_{\delta \rightarrow 0} \frac{f^{(n)}(x_0 + \delta)}{n!}$  indeed exists and is in fact equal to  $\rho_n$ .

□